POLYPUBLIE
Polytechnique Montréal

POLYTECHNIQUE MONTRÉAL
UNIVERSITÉ D'INGÉNIERIE

Titre: Title:	Polylactic Acid: Process Intensification of Polymerization and Drug Carrier Production
Auteur: Author:	Nicolas Patience
Date:	2025
Type:	Mémoire ou thèse / Dissertation or Thesis
Référence: Citation:	Patience, N. (2025). Polylactic Acid: Process Intensification of Polymerization and Drug Carrier Production [Thèse de doctorat, Polytechnique Montréal]. PolyPublie. https://publications.polymtl.ca/63268/

Document en libre accès dans PolyPublie
Open Access document in PolyPublie

URL de PolyPublie: PolyPublie URL:	https://publications.polymtl.ca/63268/
Directeurs de recherche: Advisors:	Daria Camilla Boffito, & Xavier Banquy
Programme: Program:	Génie biomédical

Ce fichier a été téléchargé à partir de PolyPublie, le dépôt institutionnel de Polytechnique Montréal
This file has been downloaded from PolyPublie, the institutional repository of Polytechnique Montréal

https://publications.polymtl.ca

POLYTECHNIQUE MONTRÉAL
affiliée à l'Université de Montréal

Polylactic Acid: Process Intensification of Polymerization and Drug Carrier Production

NICOLAS PATIENCE
Institut de génie biomédical

Thèse présentée en vue de l'obtention du diplôme de *Philosophiæ Doctor*
Génie biomédical
Février 2025

© Nicolas Patience, 2025.

POLYTECHNIQUE MONTRÉAL
affiliée à l'Université de Montréal

Cette thèse intitulée :

Polylactic Acid: Process Intensification of Polymerization and Drug Carrier Production

présentée par **Nicolas PATIENCE**
en vue de l'obtention du diplôme de *Philosophiæ Doctor*
a été dûment acceptée par le jury d'examen constitué de :

Olivier HENRY, président
Daria Camilla BOFFITO, membre et directrice de recherche
Xavier BANQUY, membre et codirecteur de recherche
Nick VIRGILIO, membre
Bruno GAILLET, membre externe

DEDICATION

To my wife, Samara ...

ACKNOWLEDGEMENTS

I would first like to acknowledge my supervisors, Daria and Xavier for their guidance throughout my doctorate; they have taught me an immeasurable amount. Special thanks to my parents for their unwavering support; my father for reading my rough rough first drafts. My brothers for helping me with programming-related issues. A shout-out to Dalma for all her immense help in the laboratory and especially for convincing me to get a dog. Alfie thanks you for that, too. I'd also like to thank Jacopo, my desk buddy turned friend. Your presence helped me through those really tough times. I appreciate the EPIC group as a whole, it's been a journey! I'd like to thank Bruno, Victor, and Mikael for your patience during the simulations, it would not have been possible without you! Thank you to Gino and Martine for subsidizing my acetone addiction, all their help with orders, and for the passing conversations in the hallway at 7 am. I'd also like to thank Xavier's group, especially Thang, my PLA-dealer. And lastly, my incredible wife, Samara, who has stood by me the whole way.

RÉSUMÉ

Le poly(D,L-lactide) est un polymère biocompatible et biodégradable ayant des applications dans le domaine biomédical, notamment dans l'administration contrôlée de médicaments. Sa synthèse conventionnelle à l'aide de l'octanoate stanneux est lente et prend plus de 4 h, voire plus dépendamment du poids moléculaire souhaité. Afin de réduire le temps de réaction dans la production du poly(D,L-lactide), nous avons polymérisé par ouverture de cycle le D,L-lactide dans un réacteur à micro-ondes (à des températures comprises entre 130 °C et 170 °C), dans deux solvants différents, le toluène et le tétrahydrofurane, en utilisant l'octanoate stanneux comme catalyseur et l'alcool benzylique comme initiateur. La réaction dans le toluène a produit du poly(D,L-lactide) d'un poids moléculaire de 31 kDa après 1 h avec un indice de dispersion de 1,5. La réaction dans le tétrahydrofurane a produit du poly(D,L-lactide) d'un poids moléculaire de 11 kDa après 4 h à 170 °C avec un indice de dispersion de 1,2. Bien que le tétrahydrofurane intéragisse mieux avec les micro-ondes que le toluène (valeur de perte diélectrique de 0,35 contre 0,1), sa teneur en eau naturelle pose problème, car l'eau scinde les chaînes de poly(D,L-lactide), entraînant une diminution du poids moléculaire. Après la synthèse du poly(D,L-lactide), nous nous sommes focalisés sur la production de nanoparticules. Les nanoparticules sont en demande croissante, car de plus en plus d'études démontrent l'efficacité des systèmes d'administration de médicaments de taille nanométrique, dont le poly(D,L-lactide) est l'un des principaux composants. Cependant, les technologies actuelles ne permettent pas de produire ces nanoparticules à une échelle suffisamment grande pour des essais cliniques ou pour l'industrie. Pour la première fois, nous avons produit dans un réacteur à disque rotor-stator des nanoparticules uniformes de dispersion $< 0{,}2$, de tailles comprises entre 58 nm et 132 nm, à des taux plus élevés (jusqu'à $864\,\mathrm{g\,d^{-1}}$) que ceux de nombreuses autres technologies disponibles. La taille des particules peut être prédite selon le modèle de coalescence limité par la diffusion ($R^2 = 0{,}89$) dans le régime de mélange lent. Celle-ci était indépendante du débit total et du poids moléculaire du poly(D,L-lactide). Nous avons également appliqué un modèle statistique de loi de puissance ($R^2 = 0{,}88$) qui prédit la taille des particules en fonction des paramètres expérimentaux (concentration de polymère dans la phase organique, vitesse de rotation, le ratio entre les débits de la phase organique et de la phase aqueuse). La concentration du polymère dans la phase organique et la vitesse de rotation du disque sont les facteurs dominants; l'influence du ratio de débit sur la taille ne représente qu'un tiers de celle des autres facteurs. Enfin, pour pousser davantage l'intensification du processus continu de nanoprécipitation, nous avons simulé le mélange et les profils de vitesse moyenne dans le réacteur à disque rotor-stator. Ces

résultats permettront d'orienter les décisions de conception visant à maximiser le potentiel de ces réacteurs pour la production de nanoparticules chargées en médicaments. Des simulations effectuées avec `Lethe`, un logiciel libre d'accès basé sur la simulation des grandes structures de la turbulence ont permis de saisir les profils de vitesses et de mélange dans un réacteur à disque rotor-stator (modélisé d'après le premier niveau du réacteur commercial R2 de FlowID) à des vitesses angulaires comprises entre $39\,\mathrm{rad\,s^{-1}}$ et $157\,\mathrm{rad\,s^{-1}}$ pour un débit adimensionnel de 29 ($C_w = Q\nu^{-1}r_D$) et un ratio entre la distance du disque au mur supérieur et le rayon du disque de 0,014 ($G = hr_D^{-1}$). Ces chiffres correspondent à des nombres de Reynolds rotationnels compris entre 4.8×10^4 to 1.9×10^5 ($\mathrm{Re} = \omega r_D^2 \nu^{-1}$). Dans les simulations, il n'existe aucune transition entre un régime d'écoulement radial à un régime d'écoulement rotatif — l'écoulement est exclusivement régi par le régime de rotation. Nous sommes les premiers à affirmer que c'est la géométrie de l'entrée qui détermine la présence ou l'absence de cette transition. Dans ce modèle, les fluides entrent dans la même région et se heurtent (comme des jets percutants) avant d'être expulsés vers l'extérieur. Le long du disque, le profil du fluide est similaire à ceux décrits dans la littérature : des écoulements radiaux sortants dans la couche de Von Kármán et des écoulements radiaux entrants dans la couche de Bödewadt. Nous avons simulé le macro-mélange en injectant deux traceurs de signes opposés et représentant deux états de mélange : 95 % et 99 %. Les rayons de mélange (rayons où les fluides sont considérés comme mélangés) diminuent avec l'augmentation des vitesses angulaires : les rayons sont de 25 mm (mélange à 99 %) et de 19 mm (mélange à 95 %) à $39\,\mathrm{rad\,s^{-1}}$, et passent à 17 mm (99 %) et 10 mm (95 %) à $157\,\mathrm{rad\,s^{-1}}$.

ABSTRACT

Poly(D,L-lactide) is a biocompatible and biodegradable polymer with applications in the biomedical field, notably drug delivery. Conventional synthesis with stannous octoate is slow and takes upwards of 4 h and more depending on the desired molecular weight. In order to reduce the reaction time, we ring-open polymerized D,L-lactide to form poly(D,L-lactide) in a microwave reactor (between 130 °C to 170 °C) in toluene and tetrahydrofuran with stannous octoate as the catalyst and benzyl alcohol as the initiator. The reaction in toluene produced poly(D,L-lactide) with a molecular weight of 31 kDa after 1 h with a dispersity index of 1.5. The reaction in tetrahydrofuran produced poly(D,L-lactide) with a molecular weight of 11 kDa after 4 h at 170 °C with a dispersity index of 1.2. Despite tetrahydrofuran's ability to interact with microwaves more readily than toluene (dielectric loss value of 0.35 vs. 0.1), its innate water content is problematic. Water cleaves poly(D,L-lactide)'s chains resulting in a lower molecular weight. After synthesis of poly(D,L-lactide), the focus shifts towards producing nanoparticles. Demand for them is increasing as more and more studies showcase the efficacy of nano-sized drug delivery systems, of which poly(D,L-lactide) is a principal component. However, current technologies are unable to produce these nanoparticles on a scale sufficiently large for clinical trials or industry. For the first time, in a spinning-disk reactor, we have produced uniform (dispersity < 0.2) nanoparticles (58 nm to 132 nm) at higher rates (up to 864 g d^{-1}) than many other available technologies. The particle size can be predicted according to the diffusion limited coalescence model ($R^2 = 0.89$) in the slow mixing regime. Particle size was independent of total flowrate and poly(D,L-lactide) molecular weight. We also fit a statistical power-law model ($R^2 = 0.88$) that predicts particle size in relation to the experimental parameters (concentration of polymer in the organic phase, rotational speed, flowrate ratio between the organic and aqueous phase). The concentration and rotation of the disk are the dominating factors; the flowrate ratio's influence on the size is 1/3 of that of the others. Finally, to push the intensification of the continuous nanoprecipitation process even further, we simulated mixing and the time-averaged velocity flow profiles in the rotor-stator spinning disk reactor. These results provide a basis for informing design decisions to maximize the potential of these reactors for producing drug-loaded nanoparticles. Large eddy simulations with `Lethe`, an open-source computational fluid dynamics software, captured the flow and bulk mixing profiles in a rotor-stator spinning disk reactor (modeled after the first level of FlowID's commercial R2 reactor) at rotational speeds of 38 rad s^{-1} to 157 rad s^{-1} at a dimensionless flowrate of 29 ($C_w = Q\nu^{-1}r_\mathrm{D}$) and a gap ratio of 0.014 ($G = hr_\mathrm{D}^{-1}$). These correspond to rotational Reynolds numbers of 4.8×10^4 to 1.9×10^5 ($\mathrm{Re} = \omega r_\mathrm{D}^2 \nu^{-1}$). There

is no point along the disk radius at which the flow transitions from throughflow-governed to rotation-governed — it is exclusively rotation-governed. We are the first to put forth that it is the geometry of the inlet that determines the presence/absence of this transition. In this model, the fluids enter into the same region and collide (like impinging jets) before being expelled outwards. Further along the disk, the fluid profile is reminiscent of the literature; radial outflows in the Von Kármán layer and radial inflows in the Bödewadt layer. Macro-mixing was simulated by injecting two tracers of opposite signs and denoting two mixing states: 99 % and 95 %. The critical mixing radius, i.e., the radius at which the fluids are considered mixed, decreased with increasing rotational speeds from 25 mm and 19 mm at $39\,\mathrm{rad\,s^{-1}}$ to 17 mm and 10 mm at $157\,\mathrm{rad\,s^{-1}}$ for 99 % and 95 % mixing states, respectively.

TABLE OF CONTENTS

DEDICATION iii

ACKNOWLEDGEMENTS iv

RÉSUMÉ v

ABSTRACT vii

TABLE OF CONTENTS ix

LIST OF TABLES xii

LIST OF FIGURES xiv

LIST OF SYMBOLS AND ACRONYMS xvii

CHAPTER 1 INTRODUCTION 1
- 1.1 Background and problem identification 1
- 1.2 Thesis Highlights 2
  - 1.2.1 Objectives 2
  - 1.2.2 Summary of Contributions 3
  - 1.2.3 Thesis Structure 5

CHAPTER 2 LITERATURE REVIEW 6
- 2.1 Polylactic Acid 6
  - 2.1.1 Synthesis 7
- 2.2 Microwaves 9
  - 2.2.1 Theory 9
  - 2.2.2 Ring-Opening Polymerization of Lactide with Microwaves 10
- 2.3 Production of Polymeric Nanoparticles 16
  - 2.3.1 Production Techniques 16
  - 2.3.2 Nanoprecipitation 17
  - 2.3.3 Microfluidics 17
  - 2.3.4 Large-Scale Production of Polymeric Nanoparticles 18
- 2.4 Spinning Disk Reactors 20
  - 2.4.1 Thin-Film Spinning Disk Reactor 21

2.4.2 Rotor-Stator Spinning Disk Reactor 22
2.5 Hydrodynamics in Rotor-Stator Spinning Disk Reactors 24
2.5.1 Macroscopic Flow Behaviour 25
2.5.2 The Finite Element Method and `Lethe` 27
2.5.3 Experimental Studies 28
2.5.4 Theoretical Studies 29
2.5.5 Main Research Gaps 30

CHAPTER 3 ARTICLE 1 – MICROWAVE-ASSISTED POLY(D,L-LACTIDE) SYNTHESIS IN TOLUENE AND TETRAHYDROFURAN 31
3.1 Abstract 31
3.2 Introduction 32
3.3 Experimental 36
3.3.1 Materials 36
3.3.2 Microwave Synthesis 38
3.3.3 Characterization 39
3.4 Results and Discussion 40
3.4.1 Solvent Selection 40
3.4.2 Evolution of the Experimental Design 40
3.4.3 Results of the Polymerizations in Toluene and THF 41
3.4.4 Microwaves vs. Conduction Heating 43
3.4.5 Predictor Screening of Toluene and THF 44
3.4.6 Proton Nuclear Magnetic Resonance (^{1}H NMR) 44
3.4.7 Differential Scanning Calorimetry (DSC) 44
3.4.8 Thermal Gravimetric Analysis (TGA) 44
3.4.9 Statistical Model 45
3.5 Conclusion 47
3.6 Conflicts of interest 47
3.7 Acknowledgements 47

CHAPTER 4 CONTINUOUS NANOPRECIPITATION OF POLY(D,L-LACTIDE) IN A ROTOR-STATOR SPINNING DISK REACTOR 51
4.1 Introduction 51
4.1.1 Nanoprecipitation Mechanism 52
4.1.2 Rotor-Stator Spinning Disk Reactor (rs-SDR) 52
4.1.3 Novelty 53
4.2 Experimental 54

4.2.1 Materials 54
4.2.2 PLA, PLA-PEG Synthesis 55
4.2.3 Characterization 55
4.2.4 Pulse Experiments in the rs-SDR 56
4.2.5 Continuous Experiments in the rs-SDR 56
4.2.6 Drug Loading Experiments in the rs-SDR 59
4.2.7 Theory — Micromixing in an rs-SDR 59
4.3 Results and Discussion 61
4.3.1 Effect of Molecular Weight on Particle Size 61
4.3.2 Transmission Electron Microscopy 62
4.3.3 Diffusion Limited Coalescence 62
4.3.4 Statistical Model for the Nanopreciptation of Polylactic Acid 65
4.3.5 Drug Loading in an rs-SDR 71
4.3.6 Nanoprecipitation Technologies: Potential for Scale-Up 73
4.4 Conclusion 75

CHAPTER 5 MIXING AND HYDRODYNAMICS IN A ROTOR-STATOR SPINNING DISK REACTOR 76
5.1 Introduction 76
5.2 Theoretical Background 77
5.2.1 Micromixing - Recap 77
5.2.2 Transition Radius and Flow Profiles 78
5.3 Model Formulation 79
5.4 Simulation Setup 79
5.4.1 Mesh Sensitivity Analysis 80
5.5 Results and Discussion 80
5.5.1 Transition and critical mixing radii 81
5.5.2 Time-Averaged Velocities 85
5.6 Conclusion 90

CHAPTER 6 DISCUSSION 91

CHAPTER 7 CONCLUSION 94
7.1 Future Research 95

REFERENCES 97

LIST OF TABLES

Table 3.1 Literature Summary. The conversion column reports the highest conversion achieved. The text in parentheses beside the conversion values represents the technique that determined said conversion. The * indicates that the authors of the study have not reported conversion and we are calculating it as we did in this study. 36

Table 3.2 Solvents and their dielectric loss values 37

Table 3.3 Design of experiments. The solvent column lists the dielectric loss values (0.096 = toluene, 0.348 = THF). The experiment number refers to the order in which the experiments were completed. The MHS-Mn column lists the corrected values for the number-average molecular weight. 41

Table 4.1 Different NP synthesis techniques with a focus on continuous large-scale production. (a) = pulsed, (b) = continuous experiments, * = theoretical calculation. The abbreviations are: GC = glass capillary, PDMS = polydimethylsiloxane, COP = cyclic olefin polymer, PID = polyimide, CTJM = coaxial turbulent jet mixer, HPH = high pressure homogenization, FFR = fiber fluidic reactor, Wa = water, Ac = acetone, Acn = acetonitrile, DCM = dichloromethane, DMSO = dimethyl sulfoxide, EA = ethyl acetate, PR = max production rate. 54

Table 4.2 DoE for pulsed experiments. * removed from analysis as an outlier. A:W R represents the acetone:water ratio. 57

Table 4.3 DoE for continuous experiments. * removed from analysis as an outlier. Experiments PP1-PP3 were with PLA-PEG. A:W R represents the acetone:water ratio. 58

Table 4.4 Particle size vs. MW (C1) 62

Table 4.5 Power model with varying parameters 66

Table 4.6 Particle size and $Đ$ as a function of total flowrate. C, R, and ω were constant. 68

Table 4.7 Production Rates in the rs-SDR 74

Table 5.1 A summary of literature studying the hydrodynamics in rotor-stator systems. * is a theoretical study of the boundary layers between two parallel infinite disks. G is the gap ratio ($G = h/r_D$). Re_{TC} is the Taylor-Couette Reynolds numbers, i.e., $r_{\mathrm{disk}} \times \omega \times (r_{\mathrm{stator}} - r_{\mathrm{disk}}) \times \nu^{-1}$. Abbreviations are as follows: EXP = experimental, LES = large eddy simulation, ILES = implicit large eddy simulation, PMM = predictive math model, NA = numerical and analytical, NRTM = numerical reaction transport model, and VKE = volume of fluid plus $k - \epsilon$ model. [1]assuming fluid is water. 78

Table 5.2 Physical parameters from FlowIDs R2 used for mesh creation and resulting operating conditions. 81

LIST OF FIGURES

Figure 2.1 Poly(D,L-lactide). 6

Figure 2.2 ROP of lactide with $SnOct_2$ and an initiating alcohol following a coordination-insertion mechanism. Reproduced from [30]. 8

Figure 2.3 Published articles per year on SDRs from 1972 to 2024. 20

Figure 2.4 Bibliometric map of keywords created with VOSViewer for based on all the SDR articles found (436) with the search strategy: "spinning disk reactor" OR "rotating disk reactor" OR "spinning disc reactor" OR "rotating disc reactor." 21

Figure 2.5 (Left) FlowID's R2 three-stage rs-SDR. Each stage is a different disk. There are three inlets and one outlet, the experimental work in the thesis relies on two of the inlets. Maximum disk rotation is 6000 RPM, total allowable flowrate is $120\,\mathrm{mL\,min^{-1}}$. (Right) Top-view of one disk from FlowID's R2 rs-SDR. The pill at the center is to magnetically couple the disk to the reactor's motor. 23

Figure 2.6 Flow regimes in a rs-SDR as a function of G and Re. The blue dots represent the region of operation for Chapter 4 and 5. Adapted from [144]. 26

Figure 2.7 Time-averaged radial velocity profile in torsional Couette flow (regime III) in a rs-SDR. Adapted from [144]. 26

Figure 2.8 Time-averaged azimuthal velocity profile in torsional Couette flow (regime III) in a rs-SDR. Adapted from [144]. 27

Figure 3.1 Power required to heat 4 mL of solvent to 170 °C. The values associated to each solvent are the dielectric loss value. 35

Figure 3.2 MW as a function of time and temperatures in toluene. Error bars represent the standard deviation. For the data between 0 h to 1 h the error bars are the size of the markers. The large standard deviations past 1 h is caused by the stochastic nature of the MW reduction events. Please refer to the main text for a more detailed explanation. 48

Figure 3.3 ^{1}H NMR spectra of poly(D,L-lactide). 49

Figure 3.4 PLA MW as a function of time in toluene (left) and a standard parity plot (right). The lines represent the non-linear regression model (eq3) and the symbols the experimental data. $R^2 = 0.91$. 49

Figure 3.5 PLA MW as a function of time in THF (left) and a standard parity plot (right). The lines represent the non-linear regression model (eq3) and the symbols the experimental data. $R^2 = 0.94$. 50
Figure 4.1 TEM images of PLA and PLA-PEG NPs. The red circles highlight well-shaped spherical particles. The orange circles highlight melting particles as a result of the beam from the TEM; images must be taken quickly to avoid complete deformation. 63
Figure 4.2 Rescaled mixing time and particle size of the experimental data overlayed onto the master curve depicting the DLC model. Pulsed: $R^2 = 0.80$, continuous: $R^2 = 0.89$, pulsed and continuous combied: $R^2 = 0.77$. 64
Figure 4.3 Size of PLA in pulse-mode nanoprecipitation at a acetone:water ratio of 1:11. The lines depict the statistical model and the circles, the experimental data. 66
Figure 4.4 $Đ$ of the PLA NPs in pulse-mode nanoprecipitation. The symbols represent the different flowrate ratios: circle = 1/11, square = 1/5, cross = 1/3. 67
Figure 4.5 Size of PLA in continuous-mode nanoprecipitation at a acetone:water ratio of 1:11. The lines depict the statistical model and the circles, the experimental data. 69
Figure 4.6 $Đ$ of the PLA NPs in continuous-mode nanoprecipitation. The symbols represent the different flowrate ratios: circle = 1/11, square = 1/5, cross = 1/3. 70
Figure 4.7 Drug loading. 71
Figure 4.8 Encapsulation efficiency. 72
Figure 5.1 2D slice of the rs-SDR. The left wall is an axis of symmetry. $\mathrm{I_E}$, $\mathrm{D_E}$, $\mathrm{D_O}$, and $\mathrm{O_E}$ represent the entrance of the reactor, the region on the disk where fluid is on its way in, the region of the disk where the fluid is going towards the outlet, and the exit of the reactor, respectively. The shaded part is the sectioned area in the time-averaged velocity in z figures 5.3, 5.10. r_D is the radius of the disk, and g_rs is the axial distance between the disk and the stator. 80
Figure 5.2 Time-averaged radial velocity in Q3 and Q2. 81
Figure 5.3 Time-averaged velocity in z at Q3 and Q2 with no discernible difference. 82
Figure 5.4 Time-averaged radial velocity adjacent to the disk's center, before and after the inlet, and across the dip towards r_D. 83

Figure 5.5 Top view of the radial velocity of the entrance region. The two inlets are on opposing sides along the horizontal plane. The black squares indicate the approximate location of the inlets. There are clear radial inflows and outflows even near the center of the disk. 84

Figure 5.6 Time and distance across the disk's radius required to achieve 99 % (squares) and 95 % (circles) mixing. The percentage underneath the markers represent the fraction of the disk's radius necessary to achieve indicated mixing. 86

Figure 5.7 Visual depiction of tracers mixing and critical radii for 99 % and 95 % mixing. The center (turquoise) are areas of mixing inferior to 99 % and 95 %. The critical radius is the distance from the center of the disk to the intersection point between non-mixed and fully mixed. The scales indicate the concentration gradients for the tracers. 87

Figure 5.8 Time-averaged radial velocity profiles for rotational speeds of $38\,\mathrm{rad\,s^{-1}}$ to $157\,\mathrm{rad\,s^{-1}}$ at $0.4r_\mathrm{D}$, $0.6r_\mathrm{D}$, and $0.8r_\mathrm{D}$. 88

Figure 5.9 Time-averaged azimuthal velocity profiles for rotational speeds of $38\,\mathrm{rad\,s^{-1}}$ to $157\,\mathrm{rad\,s^{-1}}$ at $0.4r_\mathrm{D}$, $0.6r_\mathrm{D}$, and $0.8r_\mathrm{D}$. 88

Figure 5.10 Normalized (velocities divided by ωr_D) time-averaged velocities in z. . 89

Figure 6.1 2D slice of the simulated geometry (left), 2D slice of the actual reactor geometry (right). The arc in the center represents a pill-shaped magnet that couples with the magentic motor of the rs-SDR. 93

LIST OF SYMBOLS AND ACRONYMS

Ac	Acetone
Acn	Acetonitrile
A:W R	Acetone water ratio
BN	Batch nanoprecipitation
BnOH	Benzyl alcohol
BHT	Butylated hydroxytoluene
CFD	Computational fluid dynamics
CFEG-TEM	Cold Field Emission Gun Transmission Electron Microscope
COP	Cyclic olefin polymer
CSTR	Continuously stirred tank reactor
CTJM	Coaxial turbulent jet mixer
DBTM	Dibutyltin dimethoxide
DBU	1,8-diazabicyclo(5.4.0)undec-7-ene
DCM	Dichloromethane
DL	Drug loading
DLC	Diffusion limited coalescence
DLS	Dynamic light scattering
DSC	Differential scanning calorimetry
DMF	Dimethylformamide
DMSO	Dimethyl sulfoxide
DoE	Design of experiments
D:P	Drug polymer ratio
EA	Ethyl acetate
EE	Encapsulation efficiency
EXP	Experimental
FDA	United States Food and Drug Administration
FEM	Finite element method
FFR	Fiber fluidic reactor
GC	Glass capillary
GPC	Gel permeation chromatography
HFF	Hydrodynamic flow focusing
HNT	Halloysite nanotube

HPH	High pressure homogenization
HPLC	High performance liquid chromatography
ILES	Implicit Large Eddy Simulation
LA	Lactic acid
LAB	Lactic acid bacteria
LDV	Laser Doppler velocimeter
LES	Large eddy simulation
LS	Light scattering
M:I	Momoner:initiator ratio
Mn	Number average molecular weight
MHS	Mark-Houwink-Sakurada
MW	Weight average molecular weight
NA	Numerical and analytical
NMR	Nuclear magnetic resonance
NP	Nanoparticle
NRTM	Numerical reaction transport model
NSERC	Natural Sciences and Engineering Research Council of Canada
PCL	Polycaprolactone
PDMS	Polydimethylsiloxan
PEG	Polyethylene glycol
PFR	Plug flow reactor
PHA	Polyhydroxyalkanoates
PI	Process intensification
PID	Polyimide
PLA	Polylactic acid or poly(D,L-lactide)
PLA-PEG	Poly(D,L-lactide)-poly(ethylene glycol)
PLGA	Poly(lactic-co-glycolic acid)
PLLA	Poly(L-lactide)
PMM	Predictive math model
POSS	Polyhedral oligomeric silsesquioxanes
PR	Max production rate
PS	Polystyrene
PSPG	Pressure-Stabilizing/Petrov-Galerkin
PTFE	Polytetrafluoroethylene

p-TsOH	p-toluenesulfonic acid
QoL	Quality of life
RI	Differential refractometer
ROP	Ring-opening polymerization
rs-SDR	Rotor-stator spinning disk reactor
SD	Standard deviation
SDR	Spinning disk reactor
SHMN	Staggered herringbone micromixer
$Sn(Oct)_2$	Tin(II) 2-ethylhexanoate or stannous octoate
SSA	Solid super-acids
STR	Stirred-tank reactor
SUPG	Streamline-Upwind/Petrov-Galerkin
TEM	Transmission electron microscopy
TGA	Thermal gravimetric analysis
tf-SDR	Thin-film spinning disk reactor
THF	Tetrahydrofuran
TSA	Toluenesulfonic acid
UV	Ultraviolet
VKE	Volume of fluid plus k-ϵ model
Wa	Water
WoS	Web of Science
ZnO	Zinc oxide
^{1}H NMR	Proton nuclear magnetic resonance
Symbols	
α	Proportionality constant or empirical constant in MHS equation
C	Concentration
C_p	Concentration of polymer in the organic phase
C_m	Torque coefficient
$C_w = Q\nu^{-1}r_D$	Dimensionless flowrate
d	Penetration depth
D	Particle diameter
$Đ$	Dispersity index, for polymers its MW/Mn
$Đ$	Dispersity index, for nanoparticles its $(\sigma/\bar{x})^2$
ϵ	Dieletric constant, energy dissipation rate

ϵ''	Dieletric loss
E	Engulfment model
E_{dr}	Total energy dissipation rate
F	Flowrate
$G = h/r_{\mathrm{D}}$	Gap ratio
h	Axial distance between the rotor and the stator
k	Area surfactant molecules can cover or Boltzmann constant
M_{p}	Molecular weight of the polymer
M_{t}	Total torque
N_{A}	Avogadro's number
η	Dynamic viscosity
P	Partition coefficient
p^*	Reduced pressure
ρ	Density
Q	Volumetric flowrate
R	Acetone:water ratio
r_{D}	Radius of the disk
r_{t}	Transition radius
$\mathrm{Re} = \frac{\omega R^2}{\nu}$	Reynolds number
$\mathrm{Re}_h = \omega h^2 v^{-1}$	Reynolds number
$\mathrm{Re}_{\mathrm{TC}} = r_{\mathrm{disk}} \times \omega \times (r_{\mathrm{stator}} - r_{\mathrm{disk}}) \times \nu^{-1}$	Taylor-Couette Reynolds number
$R_{\mathrm{p0}} = (\frac{3M_{\mathrm{p}}}{4\pi N_{\mathrm{p}}\rho})^{\frac{1}{3}}$	Lower limit for particle radius
$\tan\delta$	Loss tangent
T	Temperature
τ_{mix}	Micromixing time
$\tau_{\mathrm{cls}} = \frac{3}{8}(\frac{\eta}{kT})(\frac{M_{\mathrm{w}}}{N_{\mathrm{A}}C_{\mathrm{p}}})$	Coalescence time
τ_{res}	Residence time
τ_{K}	Kolmogorov time scale
$\mathbf{u}$	Fluid velocity
V	Volume
ν	Kinematic viscosity
ω	Rotational speed

CHAPTER 1 INTRODUCTION

1.1 Background and problem identification

Supply and personnel shortages in the medical field is not a new problem. Documented cases date as far back as the early 1900s for bedpans, medical officers (1906), helium (1927), species for dissection, dietary calcium (1938), and hospital beds [1, 2, 3]. Reports of medicinal shortages appeared in both world wars and as of 1990, the shortage counts began to increase with a spike in 2004 caused by insufficient influenza vaccines. As of 2022, there were 140x more publications with the term shortage(s) in their title compared to 1990 [1]. In fact, in 2020, the United States alone was low on over 100 medications with anti-cancer drugs topping the list [4]. The big picture is that drug shortage occurs when supply lags demand, however, this paints too broad a stroke [5]. Issues can occur all along the development path of a medication — lack of raw materials, technical difficulties during manufacturing, regulatory hurdles, recalls, production halts for financial reasons, mergers/acquisitions, diverted supply (e.g., to war zones), and politics [1]. However, the Food and Drug Administration (FDA) and the Government Accountability Office of the United States estimate that at least 70 % of recorded drug shortages are caused by production problems [6, 7, 8]. Another issue is the amount of drug required to treat a disease. Often, treatments require frequent drug dosing in excess amounts. The body's immune system eliminates drugs and only a fraction of it reaches the targeted area. These large doses lead to drug concentration spikes and trigger adverse side-effects and affect a patient's quality of life (QoL) [9].

Sustained and targeted drug delivery are a promising avenue in this regard. For example, sustained release can reduce the frequency of dosing, the amount of drug required, drug concentration fluctuations and thus side-effects; patient QoL improves as a result. Targeted systems carry similar boons but are able to reduce the quantity of drug needed overall by concentrating it in the desired area [9]. These systems are generally nano-sized and polymer-based, a popular one being polylactic acid (PLA) due to its biodegradable and biocompatible properties. However, conventional PLA synthesis requires heating lactic acid or lactide above 100 °C for 4 h to 16 h + [10]. This lengthy process reduces its scale-up potential and makes it more difficult to test PLA-based drug carriers in clinical settings. Furthermore, the current techniques for synthesizing these carriers are unable to produce at rates suitable for large-scale clinical trials and industry ($100\,\mathrm{g\,d^{-1}}$ and $1\,\mathrm{kg\,d^{-1}}$, respectively [11]). As a result, any drug carrier systems developed will be in short supply, once again, due to production limitations.

This thesis addresses these issues by applying the principles of process intensification (PI) to

the production of PLA and nano-sized drug carriers. The first PI technology, microwaves, targets PLA synthesis, while the second, rotor-stator spinning disk reactors (rs-SDR), targets drug carrier synthesis.

1.2 Thesis Highlights

1.2.1 Objectives

The **main objective** of this work is to intensify PLA processes from synthesis to production as a drug-loaded polymeric nanoparticle in an effort to address one aspect of the drug-shortage issue.

Sub-objective 1: is to identify the optimal conditions to ring-open polymerize D,L-lactide to PLA via microwaves. The findings of this objective have been submitted to the *Journal of Advanced Manufacturing and Processing*.

- Measure the dielectric properties of D,L-lactide.
- Polymerize D,L-lactide in tetrahydrofuran (THF) and toluene.
- Develop a statistical model to predict molecular weight (MW) as a function of reaction time and temperature.

This sub-objective demonstrated that microwaves as an energy source reduce polymerization times. In addition, many microwave-efficient solvents are unsuitable for this reaction as their OH groups interfere with PLA's chain growth. Finally, it is possible to predict the MW as a function of reaction time and temperature to produce PLA's with desired weights.

Sub-objective 2: is to develop a continuous nanoprecipitation process in a rs-SDR that produces PLA-based drug-loaded nanoparticles at rates above $100\,\mathrm{g\,d^{-1}}$. The results from this are currently being considered for intellectual property protection and will eventually be published.

- Calculate theoretical micromixing times with the engulfment model for a rs-SDR operating between $157\,\mathrm{rad\,s^{-1}}$ to $523\,\mathrm{rad\,s^{-1}}$.
- Produce PLA nanoparticles in a rs-SDR at $>100\,\mathrm{g\,d^{-1}}$.
- Load ibuprofen into PLA and poly(D,L-lactide)-poly(ethylene glycol) (PLA-PEG).

This sub-objective presents, for the first time, rs-SDRs as a viable alternative to producing drug-loaded nanoparticles on a scale suitable for large-scale clinical trials, and potentially, industry. The nanoparticles themselves were monodisperse (dispersity index < 0.2) and a size suitable for drug delivery (50 nm to 200 nm). In addition, the results fit the diffusion limited coalescence theoretical framework that predicts nanoparticle size ($R^2 = 0.89$).

Sub-objective 3: is to predict bulk mixing and flow behaviours in the rs-SDR with a Large Eddy Simulation (LES) model. The results from this are also currently being considered for intellectual property protection and will eventually be published.

- Create a structured mesh based on the geometry of the rs-SDR in Pointwise (the standard mesh creation software).
- Simulate the fluid dynamics at rotational speeds of $39\,\mathrm{rad\,s^{-1}}$ to $157\,\mathrm{rad\,s^{-1}}$ and a flowrate of $30\,\mathrm{mL\,min^{-1}}$ in two inlets.
- Simulate the input of two tracers to determine a critical mixing distance at which point the fluids are fully mixed.

For the first time, we have discovered that the geometry of the inlet determines whether or not there will be throughflow-governed time-averaged velocity profiles or if they will be exclusively rotation-governed. Furthermore, bulk mixing never requires travelling the entire distance of the disk's radius. If we consider two states, 99 % and 95 % mixed, as fully mixed then the fluids need to travel 49 % and 29 % of the disk's radius, respectively, to be blended. These two facts are indispensable for designing a unique reactor for nanoprecipitation.

1.2.2 Summary of Contributions

The following is a collection of my achievements during my doctorate excluding Chapters 4 and 5:

Submissions:

- Patience NA, Jensen HM, Banquy X, Boffito DC. 2025. **Microwave-assisted poly(D,L-lactide) synthesis in toluene and tetrahydrofuran.** Journal of Advanced Manufacturing and Processing. (*Wrote the majority of the text, conducted the majority of the experiments, proofread the manuscript.*)

Publications:

- Rivera-Quintero P, Patience GS, Patience NA, Boffito DC, Banquy X, Schieppati D. 2024. **Experimental methods in chemical engineering: Karl-Fischer titration.** The Canadian Journal of Chemical Engineering. (*Conducted part of the experiments, assisted with the creation of figures, proofread the manuscript.*)

- Schieppati D, Patience NA, Galli F, Dal P, Seck I, Patience GS, Fuoco D, Banquy X, Boffito DC. 2023. **Chemical and Biological Delignification of Biomass: A Review.** Industrial and Engineering Chemistry Research. (*Wrote part of the review, assisted with the creation of the figures, proofread the manuscript.*)

- Patience NA, Schieppati D, Boffito DC. 2021. **Continuous and Pulsed Ultrasound Pectin Extraction from Navel Orange Peels.** Ultrasonics Sonochemistry. (*Wrote the majority of the text, conducted all the experiments, proofread the manuscript*)

- Schieppati D, Patience NA, Campisi S, Patience GS. 2021. **Experimental methods in chemical engineering: High Performance Liquid Chromatography—HPLC.** The Canadian Journal of Chemical Engineering. (*Conducted part of the experiments, wrote part of the case study, proofread the manuscript.*)

Scholarships:

- Canadian Graduate Scholarship for the Ph.D. from NSERC (PGS D)

- MITACS Scholarship to work at Dymedso Inc.

- Canadian Graduate Scholarship for the M.Sc. from NSERC (CGS M)

Mentoring:

- Mentored 2 undergradate students (Canada, France) full-time for 4 months in research over 2 summers

Teaching Assistant:

- Teaching assistant for CALCULS DES RÉACTEURS CHIMIQUES (GCH3110) at Polytechnique Montréal

1.2.3 Thesis Structure

Chapter 2 introduces the relevant literature. It touches upon some foundational elements with regards to PLA, microwaves, the production of nanoparticles, and experimental plus theoretical aspects of rs-SDRs. Chapter 3, 4, 5 are tied to sub-objectives 1, 2, and 3, respectively. Chapter 7 summarizes the work presented in this thesis in addition to its limitations, aspects we found surprising, and recommendations for future research. There are no appendices.

CHAPTER 2 LITERATURE REVIEW

2.1 Polylactic Acid

Lactic acid (LA) is the building block of PLA — it is a common ingredient in the food industry and functions as an acidic flavouring buffer and a bacterial inhibitor in processed foods. Bacterial fermentation with lactic acid bacteria (LAB) accounts for 90 % of all LA production [12]. This process consumes little energy, operates at low temperatures, selectively produces D-lactic acid or L-lactic acid, and consumes renewable carbohydrate biomass. Food waste, lignocellulosic biomass, microalgae, dairy and industrial waste are all potential feedstocks for LA fermentation. Chemical synthesis of LA, on the other hand, exclusively produces D,L-lactic acid [12]. Polymerization with D-lactic acid, L-lactic acid, and DL-lactic acid produce poly-D-lactide (amorphous), poly-L-lactide (semi-crystalline), and poly(D,L-lactide), respectively [13]. From this point on, PLA refers to poly(D,L-lactide), unless otherwise specified.

PLA is an aliphatic polyester synthesized from α-hydroxy acids (Figure 2.1) with a glass transition temperature of 55 °C and degradation temperature of 200 °C [12]. This biocompatible and biodegradable polymer degrades through the hydrolysis of its ester bonds. The body processes and excretes the degradation products without causing physiological stress [13]. The FDA approved its use in the 1970s as a promising alternative to petroleum-based plastics in food packaging combined with its potential in the medical field (suturing, scaffolding, drug delivery).

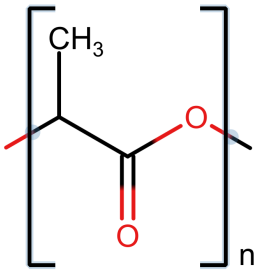

Figure (2.1) Poly(D,L-lactide).

For drug delivery, PLA is typically required to have a MW less than 50 kDa as anything larger will take too long to dissolve and is reserved for sutures and scaffolds [14]. In addition, PLA homopolymers are poor nano-carriers due to their low degradation rate, poor cell adhesion, lack of sites for cell recognition, which limits tissue compatibility and drug targeting [15, 16, 17]. The functional groups are unreactive [18], which restricts PLA for drug delivery.

As a result, lactide (the cyclic ester intermediate formed after multiple esterifications between two or more molecules of LA) is polymerized with other monomers like ϵ-caprolactone, ethylene glycol, and glycolic acid to produce copolymers with enhanced properties. Polyethylene glycol (PEG) is hydrophilic and can avoid phagocytosis from macrophages (i.e., better capability to evade the immune system) [19, 20]. These traits enhance PLA's ability to function as a drug delivery agent. A PLA-PEG copolymer has superior drug loading capacity to either PLA or PEG homopolymers; the copolymer bears a hydrophilic exterior (PEG) and a hydrophobic core (PLA) to load hydrophobic drugs and degrades faster at the target site [21, 22]. Moreover, the kidney readily eliminates the degradation products of PLA-PEG [23]. Another versatile PLA copolymer is the FDA-approved poly(lactic-co-glycolic acid) (PLGA) whose surface can harbour various peptides, antibodies, cytokines, and such for targeted delivery [24, 25]. In one example, PLGA nanoparticles (NPs), conjugated with transferrin (an iron-binding protein in the blood), selectively delivered medication to breast cancer cells overexpressing receptors for transferrin [26]. Much like its counterpart PLA and PLA-PEG, PLGA decomposes into harmless by-products, H_2O, CO_2, and LA [25]. PLA can be combined and its properties tailored to maximize therapeutic benefits – increasing or decreasing its molecular weight also affects degradation and drug release [27].

2.1.1 Synthesis

The most common route for synthesizing PLA is ring-opening polymerization (ROP) from lactide, which follows a coordination-insertion mechanism. A common catalyst for the ROP is tin(II) 2-ethylhexanoate ($Sn(Oct)_2$), also known as stannous octoate. It is soluble in molten lactide, has low toxicity, and enables the formation of PLAs with MWs above 100 kDa [12]. The FDA has approved it as a food stabilizer and its introduction into the environment is a non-issue as it oxidizes to SnO_2, a harmless tin salt (cassiterite) [28]. However, $Sn(Oct)_2$ must be transformed by an OH group — typically from an alcohol — to tin(II) alkoxide ($Sn(OR)_2$), which is the true initiator of the polymerization. In addition, $Sn(Oct)_2$ will also react with water and any other OH-bearing species in the reaction mixture to form tin(II) alkoxide [29]. Once the initiator is formed, lactide inserts itself into the Sn-OR bond and polymerization continues with the following steps (Figure 2.2) [30]:

1. **A** The alcohol reacts with $Sn(Oct)_2$ to form an alkoxide species (1) and 2-ethylhexanoic acid (3).

2. **B** A second alcohol reacts with the alkoxide species (1) to yield tin(II) alkoxide (2) and another 2-ethylhexanoic acid (3).

3. **C** OH-bearing species may also deactivate $Sn(Oct)_2$ to form a stannous alcohol derivative (4).

4. **D** The lactide monomer inserts itself into tin(II) alkoxide (2) to create the first propagating chain (5).

5. **E** The propagating chain (5) will propagate or succumb to an intermolecular exchange with another hydroxyl group from the initiator or impurity or a hydroxy end chain; an equilibrium is established between activated and deactivated chain ends (R represents unreacted alcohol initiator molecules, impurities, or hydroxy chain ends). Impurities are any source of uncontrolled OH-bearing species (e.g., excess moisture).

6. The chains continue to propagate via acyl oxygen cleavage of the lactide.

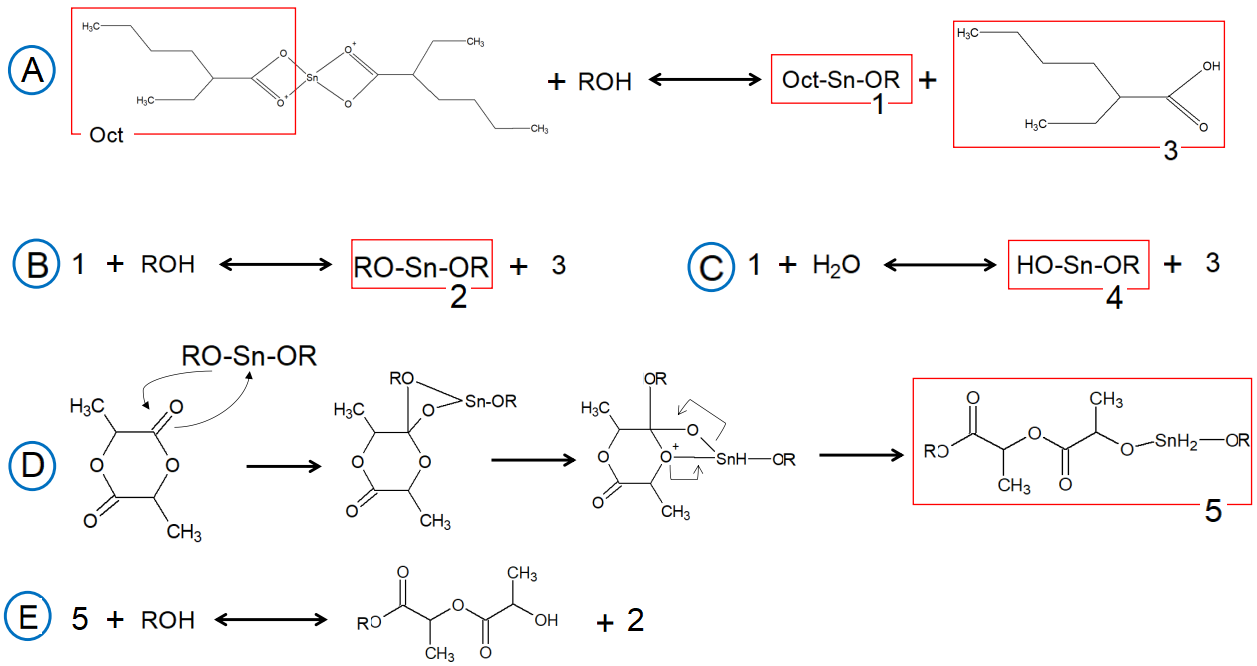

Figure (2.2) ROP of lactide with $SnOct_2$ and an initiating alcohol following a coordination-insertion mechanism. Reproduced from [30].

ROP of lactide is, kinetically, first order and the polymerization rate peaks when the ratio between $Sn(Oct)_2$ and the alcohol is 0.5 [30]. This is the ideal ratio to shift the equilibrium of step **A** (Figure 2.2) towards the right so that all the R-OH is consumed to form tin(II) alkoxide [29]. Otherwise, the MW of the resulting PLA depends on the ratio between lactide and the initiating species.

The second route to produce PLA is direct polycondensation of LA. However, this method produces low MW PLAs relative to ROP [31]. Its mechanism is reversible step-growth polymerization; LA molecules form dimers, trimers, oligomers, and finally polymer chains. The reversibility and production of water limits the final MW — this water is difficult to remove and its presence hydrolyzes the polymer chains [31].

2.2 Microwaves

2.2.1 Theory

Microwaves are part of the electromagnetic spectrum with wavelengths between 1 mm and 1 m and frequencies between 300 MHz and 300 GHz. This spectrum is also home to wireless networks, cellphones, radars, and satellite communications. Thus, the United States Federal Communications Commission has designated 0.9 GHz and 2.45 GHz as the two frequencies for microwave heating for industrial, scientific, and medical purposes [32].

Microwave irradiation is an unconventional energy source for chemical reactions and qualifies as a PI technology [33]. It heats reactor contents volumetrically and in a uniform manner thereby increasing reaction rates [34]. Dipole polarization and ionic conduction are the two mechanisms by which microwaves heat molecules [35, 36]. In the former, molecule dipoles rotate in response to the generated electromagnetic field causing internal resistance to the rotation producing heat [37, 38]. More specifically, it is the local charge in a material that moves in response to the electric field. There is a lag time between the polarization of this charge and the applied electric field, known as the relaxation time, in which energy is dissipating as heat [32]. This relaxation time is what allows materials/solvents to heat via microwaves. In ionic conduction, charged particles oscillate and collide [37, 39]. Overall, the microwaves need to penetrate and transmit their energy to solvents for these to generate heat. The loss tangent ($\tan\delta$), the dielectric constant (ϵ), and the dielectric loss (ϵ'') are the parameters that govern a given solvent's ability incorporate microwaves (Equation 2.1) [40].

$$\tan\delta = \frac{\epsilon''}{\epsilon} \tag{2.1}$$

$\tan\delta$, ϵ'', and ϵ represent the efficiency with which a solvent transforms microwave energy into heat, the conductance of said solvent, and the ease with which said solvent becomes polarized in an electric field, respectively [41]. Aside from dipole polarization and ionic conduction, there is also electronic polarization, atomic polarization, and Maxwell-Wagner polarization mechanisms that factor into a given solvent's dielectric response [32]. However, at the given

frequencies that microwave reactors operate, dipole polarization is the most important mechanism that generates heat at the molecular level [42, 43]. In conclusion, it takes less energy to heat and maintain solvents at a desired temperature if they have high dielectric property values assuming other properties are equal. For example, the power required to heat toluene ($\epsilon'' = 0.1$) to 170 °C peaked at 420 W whereas the peak for dimethylformamide ($\epsilon'' = 6.1$) was 320 W.

Penetration Depth

Solvents with OH groups have ϵ'' that can go as high as 50 (e.g., ethylene glycol). However, these kinds of solvents can potentially inhibit uniform heating as they have low penetration depths. The penetration depth, d (Equation 2.2), is the distance at which the microwave power has lost 63 % of its initial value [44]. In other words, the distance from the surface of the material where microwave absorption is $1/e$ of absorption at said surface.

$$d = \frac{c\epsilon_0}{2\pi f \epsilon''} \tag{2.2}$$

Where, ϵ_0 is the dielectric constant of free space, f is the frequency, and c is the speed of light [32]. To ensure uniform heating, a solvent must have a penetration depth equal or greater than the size of the reactor in which it is being heated. For example, toluene has a penetration depth in m range [45], and thus will uniformly heat in lab-scale microwave reactors as the radius of their reaction vessels are generally in the cm range. Penetration depth decreases with increasing dielectric properties. In other words, if the penetration depth is substantially smaller than the thickness of the material to be heated, then only the surface will heat via microwaves while the interior will heat via conduction [32]. For example, water, with a dielectric loss value of 10 has a penetration depth of 50 mm at 90 °C [46]. Thus, solvent selection is an important metric to maximize efficient and uniform heating. Overall, from a polymer synthesis standpoint, microwave heating has already shown to increase reaction rates for step-growth and ring-opening polymerizations compared to conduction heating [47].

2.2.2 Ring-Opening Polymerization of Lactide with Microwaves

The following search strategy generated less than 100 results from Web of Science (WoS): (microwave or micro-wave) AND (poly-lactic acid* OR PLA OR polylactic* acid* OR polylactid*) AND (polymerization OR ring-opening poly*). Approximately 40 were relevant. The literature search focused on ROP as it is a more performant method for producing PLA. In addition, domestic microwaves are less than ideal for synthesis as pressure and temper-

ature are more difficult to monitor and control compared to dedicated microwave reactors. Moreover, certain articles have attributed the behaviour of their data to non-thermal effects as a result of microwaves when in reality said behaviour can most likely be attributed to unreliable temperature measurements [48].

Ring-Opening Polymerization with $Sn(Oct)_2$

A domestic microwave oven polymerized L-lactide via ROP in the presence of $Sn(Oct)_2$ at 180 W and 360 W for 5 min to 30 min at different monomer-to-initiator ratios (1040:1, 2534:1, 5069:1) [49]. As the monomer:initiator (M:I) ratio increases so does the MW of the resulting PLA. There are fewer initiator molecules for a given number of monomers, which results in the formation of fewer but longer chains. However, this article mistakenly identifies $Sn(Oct)_2$ as the initiator. It is more likely that residual water in the reactor is activating the catalyst. As irradiation time increased from 10 min to 20 min, the MW went from 4.2 kDa to 10 kDa. As the power doubled from 180 W to 360 W, the MW at 5 min and 10 min were 7.6 kDa and 9.4 kDa, respectively. However, passed 10 min the PLA degrades and the MW decreases. There was no measure of temperature throughout the reactions. The optimal conditions were at a M:I ratio of 2534:1, an irradiation time of 20 min, at 180 W for a MW of 77 kDa and a dispersity ($Đ$) of 2 [49]. $Đ$ is the ratio between the weight average molecular weight and the number average molecular weight (Mn). In a similar experiment, microwaves synthesized PLA via ROP of L-lactide at a constant power of 180 W, a constant M:I ratio of 5069:1, with $Sn(Oct)_2$ (no initiator) and varying temperatures (130 °C, 150 °C, 180 °C) and times (10 min, 15 min, 20 min, 30 min). The largest MW was 11 kDa after 20 min at 180 °C; further irradiation reduced the MW of PLA [50]. In addition, Singla et al. compared a second catalyst, dibutyltin dimethoxide (DBTM), to $Sn(Oct)_2$ at 150 °C with ratios of 1040:1, 2534:1, 5069:1, 10 069:1. $Sn(Oct)_2$ outperformed DBTM producing a molecular weight 3x higher (0.1 Da vs. 0.03 Da) with similar $Đ$ (1.65) after 20 min [51]. A microwave reactor under vacuum with nitrogen sparging assisted the ROP of D-lactide in the presence of $Sn(Oct)_2$, benzyl alcohol (BnOH), and toluenesulfonic acid (TSA). $Sn(Oct)_2$ paired with BnOH at an unspecified ratio was added at 0.03 % by weight of lactide and TSA at 0.4 % by weight of lactide. The highest MW was 20 kDa after 25 min at 280 W and 215 °C [52].

Microwave irradiation ROPed D,L-lactide in the presence of $Sn(Oct)_2$ with chitosan and hydroxyethyl chitosan as initiators. PLA grafted onto hydroxyethyl chitosan over 100 % more effectively than to neat chitosan (318 % versus 209 %). The side chains were also 3x as large (3.5 kDa versus 1.2 kDa). The optimal reaction conditions were 130 °C for 15 min with a catalyst concentration of 0.05 % mol relative to lactide. Hydroxyethylation of chitosan

increased its reactivity by weakening its hydrogen bonds [53].

In another instance, L-lactide polymerized and grafted onto polyhedral oligomeric silsesquioxanes (POSS) in the presence of $Sn(Oct)_2$ and in the absence of any solvent. A microwave power of 45 W, at 120 °C for 45 min and a catalyst concentration of 1.5 wt % with respect to lactide and a molar ratio of L-lactide:POSS-$(OH)_{32}$ of 600 synthesized PLA tails with a Mn of 50.5 kDa. The Young's modulus and tensile strength of POSS-PLLA increased by 57 % and 27 %, respectively, compared to neat PLLA. In addition, the structure was a nanofibrous scaffold that promoted cell adhesion (mouse pre-osteoblastic cell line) and spreading [54].

Castor oil can also initiate the polymerization of L-lactide in a microwave reactor at 150 W and lactide:castor oil ratios ranging from 113 to 533. The optimal conditions were a ratio of 533:1 and a reaction time of 50 min, which produced a Mn of 22 kDa and a $Đ$ of 1.2. Castor oil has three OH groups, which lead to a star-shaped PLLA [55]. Thauvin et al. compared the effectiveness of $Sn(Oct)_2$ to 1,8-diazabicyclo(5.4.0)undec-7-ene (DBU) for the synthesis of PEG-PLA diblock copolymers; the monomers were mPEG2000 and D,L-lactide. Conversion with DBU in chloroform after 5 min was 100 %, 94 %, and 40 % at 100 °C, 170 °C, and 60 °C, respectively. Conversion with $Sn(Oct)_2$ at 170 °C was 95 %, however, the other temperatures were too low for $Sn(Oct)_2$ to be active (60 °C to 100 °C) [56]. In addition, 5 min is not sufficient for $Sn(Oct)_2$ to activate with residual water and not a dedicated initiator.

Polyhydroxyalkanoates (PHAs) — thermoplastic polyesters produced from bacterial microorganisms under stress (reduced access to nutrients) — can also initiate the ROP of lactide. Microwave irradiated a mixture of D,L-lactide, PHA, toluene and $Sn(Oct)_2$ at 115 °C for 5 min. A lactide:PHA ratio of 250:1 produced a Mn of 45 kDa with a $Đ$ of 1.8 and a conversion, determined by gravimetry, of 85 % [57].

Clay is also able to initiate ROP of lactide and create PLA-clay nanocomposites. Two commercially available clays (Cloisite 30B and 15A) initiated the ROP of lactide in a microwave reactor at 150 °C with a M:I ratio of 2500:1 and $Sn(Oct)_2$. Polymer yield decreased with increasing Cloisite 15A loading from 72 % and 0.5 % to 4 % and 5 %, respectively. On the other hand, Cloisite 30B's polymer yield fluctuated from 88 % to 58 % and back to 79 % at clay loadings of 0 %, 2.0 %, and 5.0 %, respectively [68]. Cloisite 30B contains two OH groups whereas Cloisite 15A does not, which explains the difference in polymer yields [10].

Surface ROP is another possibility to create multi-functional materials. D,L-lactide ROPed onto the surface of magnetite particles in the presence of $Sn(Oct)_2$ under microwave irradiation at 100 °C for 11 min [58]. The authors made no comments with regards to the MW of the PLA. A microwave reactor outperformed other PLA synthesis methods (vacuum-sealed vessel with conventional heating and a high-pressure reactor) in terms of MW and reaction

time. Conventional heating in a vacuum sealed vessel led to PLA of 250 kDa and a $Đ$ of 3 after 150 h at 150 °C. The high-pressure reactor led to a PLA of 190 kDa and a $Đ$ of 2.4 after 6 h at 120 °C and 138 kPa. In contrast, microwave irradiation led to a PLA of 300 kDa and a $Đ$ of 1.7 at 100 °C for 30 min [59]. All M:I were 5000:1.

A microwave-assisted ROP method synthesized PLA-PEG copolymers after 5 min in chloroform at 125 °C; the catalysts were $Sn(Oct)_2$ and DBU. D,L-lactide was the starting reagent, D,L-lactic acid and mPEG2000 were the initiators. A M:I ratio of 278:1 resulted in PLA-PEG polymers with a MW of 40 kDa and conversions of up to 35 % or 83 % with $Sn(Oct)_2$ or DBU, respectively [60]. A solvent evaporation method produced NPs of the polymers loaded with resiquimod — immune cells actively ingested the NPs with no signs of toxicity; the NPs successfully released the drug [60].

Dextran activated $Sn(Oct)_2$ to initiate the ROP of L-lactide under microwave irradiation to produce a dextran-grafted-PLA. Optimal conditions of a M:I ratio of 4:1, a catalyst wt % of 3 with respect to lactide, 135 °C, and 15 min of reaction time led to lactide conversion of 46 % and a graft rate of 142 % [61]. Graft rate and conversion were defined as: (W1-W2)/W2 and (W1-W2)/W3; W1, W2, and W3 represent the weight of dextran-graft-PLA, weight of dextran before grafting, and weight of lactide before grafting, respectively.

A pullulan, glycolide, D,L-lactide copolymer can load 11 % curcumin and exhibit thermo-responsive properties in a drug release setting against tumors. 39 °C triggered the loaded NP copolymer to release curcumin. The ratio of lactide/glycolide/pullulan controls the hydrophobic-hydrophilic balance, solvation, and degradation rate. The microwave-assisted method operated under a nitrogen atmosphere at 80 °C for 5 min in dimethyl sulfoxide (DMSO) with $Sn(Oct)_2$ at a D,L-lactide:glycolide molar ratio of 8:1 and a D,L-lactide:pullulan molar ratio of 45:32 [62].

Starch can also initiate $Sn(Oct)_2$ for the ROP of L-lactide thanks to its OH groups — PLA grafts itself onto the starch. A lactide:starch ratio of 5:1, 450 W of power at 100 °C for 6 min grafted the most PLA (in % mol) at 62 % [63]. The authors made no comments with regards to the MW or the $Đ$.

Halloysite nanotubes (HNTs) also initiate the ROP of L-lactide by interfacing with $Sn(Oct)_2$ — the result is poly(L-lactide) (PLLA) grafted onto HNTs, which increases the mechanical properties of HNT-PLLA nanocomposites compared to a physically blended HNT-PLLA with poor interfacial adhesion [64]. A microwave carried out the ROP of L-lactide with $Sn(Oct)_2$ at L-lactide:HNT mass ratios of 5:1, 10:1, 20:1, and 40:1. At 30 W, 130 °C, and a 40:1 mass ratio, grafting percentage increased from 8 % to 23 % as the reaction time increased from 15 min to 30 min; reaction times passed 30 min reduced grafting %. Otherwise, grafting

increased with increasing microwave power (from 20 W to 30 W) at 130 °C, but began to decrease past 30 W. Finally, temperature affected the grafting in a similar fashion — from 110 °C to 130 °C grafting increased from 9 % to 42 % and at 140 °C it decreased to 13 %. The optimal conditions were a reaction time of 30 min at 30 W and 130 °C. The tensile strength and modulus of HNT-graft-PLLA at a HNT wt % of 10 and neat PLLA were 32 MPa, 1.1 GPa and 26 MPa, 0.9 GPa, respectively. In addition, the HNT-graft-PLLA was compatible with fibroblasts and promoted adhesion and proliferation despite the HNT filler — biocompatibility at the surface was sufficient [64].

A microwave-assisted method ROPed PLA from D,L-lactide with an imidazoline-functionalized polystyrene-based macroinitiator and $Sn(Oct)_2$ in anisole. Competition between the pendant imidazoline rings and the OH groups potentially inhibited the polymerization as they both compete for $Sn(Oct)_2$. After polymerization, a methanol/sodium hydroxide aqueous solution selectively degraded PLA to leave an imidazoline- functionalized porous polystyrene framework [65].

Ring-Opening Polymerization with Alternative Catalysts

Titanium-based catalysts are also viable for ROP of lactide. A microwave polymerized lactide at 130 °C for 3 h in a solvent-free environment with a calix[4]arene-based titanium (IV) catalyst at different ratios. Conversion decreased from 96 % to 67 % and MW increased from 18 kDa to 43 kDa as the monomer:catalyst ratio increased from 200 to 1994 [66]. The $Đ$ was 1.2 in all cases. Similarly, bis(phenyl-beta-diketonato)titanium(IV) ethoxide complexes ROPed L-lactide under microwave irradiation. Titanium complexes are cheap, customizable, highly active, and prevent parasitic reactions (transesterifications), which allows control over lactide polymerization and yields low $Đ$. Conditions of 180 °C, 400 W, and a reaction time of 45 min produced PLLA with a MW of 43 kDa and a $Đ$ of 2.4 [67]. Overall, the results were erratic and there were issues with reproducibility most likely from an inability to eliminate residual water from the reactor; this also explains the high $Đ$.

Zinc, zinc oxide (ZnO), and zinc lactate demonstrate favourable activity for ROP of lactide between 100 °C and 180 °C with conversions above 80 %. Mono-modal and multi-modal microwave reactors conducted the ROP of D,L-lactide (1 g) in the presence of ZnO (8.5 wt % with respect to lactide) and toluene. The reaction conditions were 130 °C, 600 RPM of stirring and times between 20 min and 180 min. At 180 min, conversion reached 98 % with a Mn of 2.2 kDa with the multi-modal microwave reactor. The mono-modal reactor achieved 95 % conversion and a Mn of 1.2 kDa at the same conditions. In addition, the multi-modal reactor's grafting degree was higher than the mono-modal reactor (18 % vs. 8 %). In

summary, ZnO NPs are able initiators for ROP of D,L-lactide and result in PLA-graft-ZnO particles [68].

Colocasia esculenta mucilage — a water-soluble polysaccharide — has OH groups that allow it to function as an initiator in the ROP of D,L-lactide. The ideal conditions were 60 °C, a lactide:mucilage ratio of 4:1, 0.1 g $Sn(Oct)_2$, a reaction time of 19 min, and stirring at 400 RPM. The resulting grafting percentage was 133 % and 33 %, respectively. On the other hand, conventional synthesis resulted in a grafting percentage and efficiency of 166 % and 41 %, but with a longer reaction time (6 h) [69]. Microwave-assisted ROP enabled the synthesis of PLA with seven different initiators — sorbitan esters (Spans© 60 and 65), their PEGylated counterparts (Tweens© 60 and 65), and D,L-lactic acid. DBU (2.5 mol % relative to D,L- lactide) and one of the initiators polymerized D,L-lactide at 75 °C for 5 min under a nitrogen atmosphere. The MWs capped at 49 kDa with PLA-Span65 compared to plain PLA at 31 kDa. The authors further tested the entrapment efficiency and discovered that plain PLA was the most efficient (13 % versus 10 % for PLA-Span60, the next best) — additional hydrophobic groups did not allow for higher loading [70]. Bakibaev et al. studied the ROP of L-lactide in a microwave reactor and with conventional heating using $Sn(Oct)_2$, p-toluenesulfonic acid (p-TsOH), and alpha alanine. All polymerizations occurred at 160 °C. Conventional heating produced a MW of 2.2 kDa with a $Đ$ of 1.4 after 16 h at a M:I of 1000:3 with $Sn(Oct)_2$. Microwave heating produced a MW of 4 kDa with a $Đ$ of 1.35 after 10 min at a M:I of 1000:3 with $Sn(Oct)_2$. Alpha-alanine and p-TsOH produced a MW of 4 kDa with $Đ$ of 1.4 after 10 min but with a M:I of 1000:2 [71].

Solid super-acids (SSA) are potential green catalyst alternatives to $Sn(Oct)_2$. Microwave-assisted polycondensation of L-lactic acid synthesized a yellow-tinted PLA with a MW of 20 kDa at 260 °C for 60 min with 0.4 wt% SSA. A reflux condenser connected to a vacuum evacuated the produced water during the reaction. The yellowness is indicative of degradation — reducing irradiation time or temperature would have increased the final MW as PLA begins to degrade above 200 °C. Acetic ester and vacuum drying at 105 °C recovered the Al_2O_3/SO_4^{-2} SSA catalyst; its reactivity showed no decline after 5 cycles of polycondensation and recovery [72]. Melt polycondensation of L-lactic acid in a microwave reactor produced PLA with a MW of 4.8 kDa in the presence of p-TsOH (0.3 mol % with respect to LA), at 180 °C, for 60 min. In contrast, ROP of L-lactide at the same conditions led to a MW of 9 kDa [73].

This concludes the literature for sub-objective 1 (*Chapter 3/Article 1: Microwave-assisted poly(D,L-lactide) synthesis in toluene and tetrahydrofuran*). For a distilled summary of the literature concerning microwave synthesis of PLA, the reader is referred to Table 3.1. Over-

all, polymerization times for PLA in microwaves are much lower (minute) compared to conventional heating (h); microwave reactors are well-suited for this reaction. However, the literature lacks discussion on leveraging the dielectric properties of the reagents and scale-up of these processes.

2.3 Production of Polymeric Nanoparticles

NPs are promising tools for drug delivery in medicine. They can be precipitated to small enough sizes (50 nm to 150 nm in diameter) as to avoid defence mechanisms of the immune system and circulate for long periods of time in the body; NPs with a diameter greater than 200 nm are readily removed from the human body by the immune system [74].

2.3.1 Production Techniques

There are a multitude of techniques to produce NPs: solvent evaporation, emulsion diffusion, salting out, dialysis, and nanoprecipitation [75, 76].

- *Solvent evaporation*: polymers are dissolved in an organic solvent and subsequently mixed with water. The organic solvent is then evaporated to form the NPs.
- *Emulsion diffusion*: an oil/water emulsion is formed beetween a water-miscible solvent, in which polymer and/or drug is dissolved, and an aqueous solution with or without a surfactant [77, 78]. This mixture is then diluted with water, which induces solvent diffusion causing colloidal particles to form.
- *Salting out*: polymers are first dissolved in an organic solvent (acetone and THF being common ones) that is water soluble. This organic phase is subsequently mixed with an aqueous phase containing salts (e.g., magnesium chloride hexahydrate) and stirred. The water-soluble organic solvent begins to associate itself with the aqueous phase. This movement causes NPs to form. The product is centrifuged to remove the salting-out reagents and then purified [79].
- *Dialysis*: this technique relies on a semi-permeable membrane that functions as a barrier for the polymers. As with the other techniques, polymer with or without drug is dissolved in an organic solvent and then placed in a dialysis membrane and dialyzed with a non-solvent (e.g., water). The organic solvent's dissolving power decreases over time as it associates with the non-solvent. In addition, an increase in interfacial tension induces polymer aggregation. The final product is a colloidal suspension of NPs with a narrow size distribution [80].

Nanoprecipitation is the most common method for precipitating NPs smaller than 200 nm with narrow size distributions [81] — emulsification solvent evaporation techniques struggle in this regard [82]. Thus, it is the method of choice for the research found in this thesis and microfluidics, a staple NP-producing technology.

2.3.2 Nanoprecipitation

Nanoprecipitation, also known as the solvent displacement method, involves two phases. One phase is the polymer and drug (if drug loading) dissolved in a water-soluble organic solvent (e.g., acetone, acetonitrile) that can be easily evaporated [83, 84]. The second phase is an aqueous one with or without surfactants. Nanoprecipitation relies on interfacial polymer deposition after the organic solvent migrates into the aqueous phase [85]. The organic phase is mixed with the aqueous phase — dropwise or in another controlled manner (e.g., syringe pumps). As the phases mix, NPs instantly form to avoid and minimize contact with water. The organic phase can be added to the aqueous phase and vice versa with no effect on NP formation [86].

2.3.3 Microfluidics

Microfluidics is one of the dominant technologies for producing NPs via nanoprecipitation. They are able to consistently produce particles loaded with drugs in the ideal size range with narrow particle size distributions and batch-to-batch reproducibility, which is crucial for medical applications. The controllable factors in a microfluidic system are: size of the microchannels, total flowrate, flowrate ratio between the organic and aqueous solutions, the concentration of the polymer and drug (if encapsulating) in the organic solvent, choice of organic solvent, and the polymer system (PLA, PEG-PLGA, etc.). These affect NP size, drug loading and efficiency, as well as drug release [87].

- *Size of the microchannels*: as the dimensions of the microchannel get smaller, so does the average particle size of the NPs down to a lower limit. Microchannels with cross-sectional areas of 1959 μm^2 and 855 μm^2 produced no significant difference in particle size; however, the smaller channel yielded a more uniform distribution. There is a linear relationship between NP size and width of the focused stream [88].
- *Total flowrate*: efficient mixing increases with flowrate. This engenders a reduction in the average particle size because mixing favours nucleation. As more nuclei form, their overall growth will be limited by the quantity of available polymer in the solution — thus an increase in the generation of nuclei will decrease the NP size [89].

- *Flowrate ratio between the organic and aqueous phase*: keeping other parameters constant, a decrease in this ratio leads to a decrease in the NP size as well as a narrower particle size distribution. The size of NPs increases linearly with the flowrate ratio [74].
- *Concentration of the polymer in the organic phase*: a higher concentration of polymer increases the solution viscosity, which will decrease the rate of mixing and produce larger particle sizes [74].
- *Concentration of the drug in the organic phase*: the presence of a drug will slightly increase the size of the NPs as a result of the drug loading. The average particle size of polymeric micelles increased from 56 nm to 62 nm when loaded with mithramycin [74].
- *Choice of organic solvent*: a solvent for microfluidics must be miscible with water and simultaneously dissolve the polymer being precipitated. A solvent with a greater affinity for water enhances solvent diffusion and polymer partition into the aqueous phase, which results in smaller particle sizes of the precipitate [89].
- *Polymer systems*: Drug loading and encapsulation efficiency rely on the affinity a drug has for a particular polymer. When loading a hydrophobic drug, if the hydrophobic polymer is in greater proportion than the hydrophilic one, drug loading will be more effective. For example, with further addition of PLGA into the PLGA-PEG NPs (100 % PLGA-PEG versus 80 % PLGA-PEG and 20 % PLGA), the loading of the hydrophobic drug, docetaxel, increased from 28 % to 51 %. In addition, encapsulation efficiency increased from 4 % to 7 %. Furthermore, the polymer system also determines the release profile of the drug. In the presented case, docetaxel will release slower in the system with additional PLGA because it will be held more tightly in the NPs [90].

2.3.4 Large-Scale Production of Polymeric Nanoparticles

Feasible production rates for polymeric NPs for drug delivery is $100\,\mathrm{g\,d^{-1}}$ for clinical trials and $1\,\mathrm{kg\,d^{-1}}$ for industry [11]. The search strategy ((nanoparticles OR "nano particles") AND (PLA OR "polylactic acid" OR PLGA) AND ("large-scale" OR "gram scale" OR "industrial-scale")) yielded 117 results — 95 articles and 22 review articles. Of these 95, 15 were relevant to drug delivery systems. Within these, two focus their efforts on sonication processes [91, 92], three on membrane nanoprecipitation and emulsification [93, 94, 95], one on high pressure homogenization [96], one on fiber fluidic reactors [97], and eight on microfluidics [98, 99, 100, 101, 102, 103, 104, 105]. This is by no means a comprehensive list, but rather to signal the strong presence of microfluidics in the space of large-scale NP production. Unfortunately,

microfluidic channels are commonly made from polydimethylsiloxan (PDMS), a hydrophobic polymer, on which PLGA aggregates. PLGA is one of the most recurrent polymers from which drug carriers are made of. Similarly to plain PLA, it is FDA-approved, biodegradable, biocompatible, and stable during storage. It hydrolyzes into LA and glycolic acid, which are naturally eliminated from the human body [106]. PLGA production rates in PDMS channels are lower than $7.2\,\mathrm{g\,d^{-1}}$ [107]. Several approaches to overcome this issue are 3D hydrodynamic flow focusing (HFF) and pairing PLGA with lipids or amphiphilic polymers. PDMS as the base material can also be eliminated in favour of glass or polytetrafluoroethylene (PTFE) — this eliminates aggregation issues and elevates the system's endurance to pressure [107]. The latter translates to higher permissible flowrates and thus higher production rates.

3D HFF: focuses the stream in 3D so the polymer solution is never in contact with the PDMS walls and aggregation no longer becomes an issue — the properties of the produced NPs are similar to those produced with 2D HFF [108]. A single 3D HFF microchannel synthesized PLA-PEG at a production rate of $0.25\,\mathrm{g\,d^{-1}}$, far from the desired $100\,\mathrm{g\,d^{-1}}$ to $1\,\mathrm{kg\,d^{-1}}$. However, 8 parallel 3D HFF microfluidic channels yielded a production rate of $2\,\mathrm{g\,d^{-1}}$; this rate can be further increased by increasing the number of parallel channels [109]. This method has the potential to satisfy industrial production standards, withstanding economic analyses.

Microfluidic devices fabricated without PDMS: glass capillary devices are able to produce PLGA NPs at production rates of $60\,\mathrm{g\,d^{-1}}$ with a single microchannel [107]. In addition, glass is resistant to a plethora of chemicals and can withstand higher pressures than PDMS, permitting more process diversity. A series of these channels in parallel would satisfy the industrial production rates. In another instance, 8 parallel 3D HFF microchannels fabricated from polyimide (PID) had a PEG-PLGA NP (diameters between 50 nm and 85 nm) production rate of $312\,\mathrm{g\,d^{-1}}$ [99]. Moreover, a PTFE-based coaxial turbulent jet mixer achieved production rates as high as $3\,\mathrm{kg\,d^{-1}}$ with a total flowrate of $480\,\mathrm{mL\,min^{-1}}$ — modification of the Reynolds number controlled NP sizes between 25 nm and 100 nm [11]. Production rates with these devices are massively improved compared to PDMS-based systems. However, one of the advantages of PDMS is its ability to mold into complex channel shapes, which affords more control over the nanoprecipitation process and in turn the ability to synthesize more complex NPs [107]. Glass on the other hand is difficult to microfabricate and silicon-based microfluidic systems are expensive and fragile [110].

Overall, microfluidics dominant the space of NP production with a few guest appearances (sonication processes, coaxial turbulent jet mixers) in the literature. Spinning disk reactors are a relatively new technology that is up-and-coming with fewer than 20 published articles per year until 2012. They have immense potential for large-scale nanoparticle production.

2.4 Spinning Disk Reactors

Spinning disk reactors (SDR) are a type of PI technology [33] known for their exceptional heat and mass transfer capabilities, making them highly effective for multiphase chemistry (liquid-gas, liquid-liquid, gas-liquid-liquid). Typically, these reactors feature one or more rotating disks housed in a casing, which generate significant shear and centrifugal forces, creating optimal conditions for mixing. Literature on SDRs dates back to the 1970s, with few publications per year and peaking at 23 in 2012 (Figure 2.3). Research in this domain remains in its infancy. The search strategy: "spinning disk reactor" OR "rotating disk reactor" OR "spinning disc reactor" OR "rotating disc reactor" in the WoS Core Collection yielded 436 articles on SDRs.

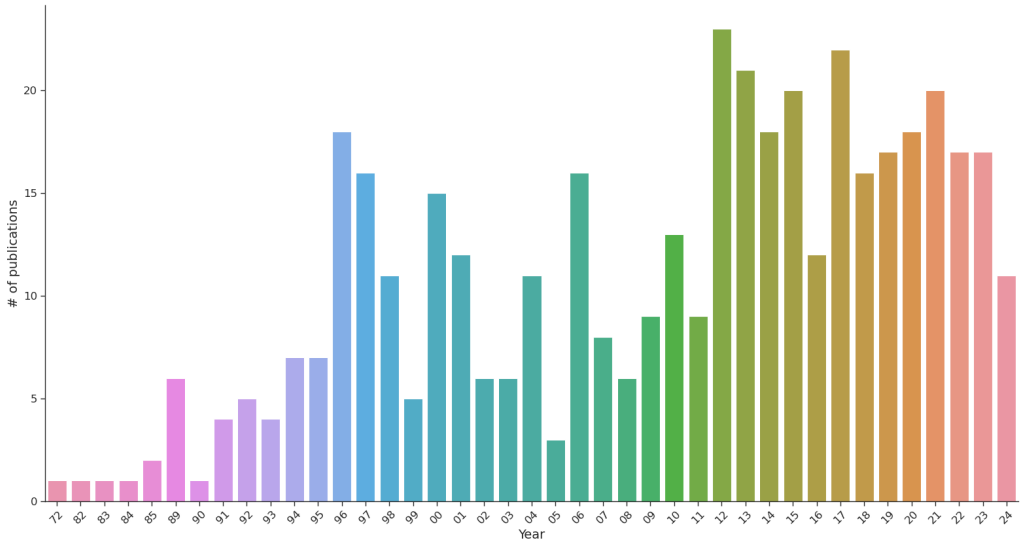

Figure (2.3) Published articles per year on SDRs from 1972 to 2024.

VOSViewer generated a bibliometric map of keywords from these articles; the size of the circles relates to the frequency of the keywords while the colours denote related concepts (Figure 2.4). The most frequent keywords are photocatalysis, degradation, followed by nanoparticles, precipitation, and then free-radical polymerization. There is much overlap with photocatalysis, degradation and NPs, as the latter is often a central part of the former. For example, ZnO [111] and copper oxide [112] NPs, as well zinc oxide-titanium dioxide nanocomposites [113] for photocatalysis and degradation. In other cases, the SDR is for synthesizing CU NPs [114], calcium carbonate NPs [115], magnetite NPs [116], curcumin NPs [117], silver NPs [118], and starch NPs [119], to list a few.

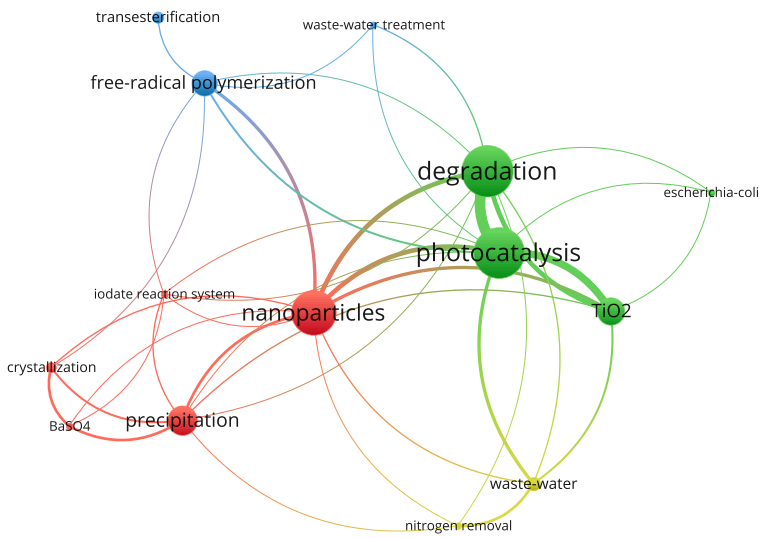

Figure (2.4) Bibliometric map of keywords created with VOSViewer for based on all the SDR articles found (436) with the search strategy: "spinning disk reactor" OR "rotating disk reactor" OR "spinning disc reactor" OR "rotating disc reactor."

Overall, NPs account for 20 % of these articles. The majority work with thin-film spinning disk reactors and none produce polymeric NPs.

2.4.1 Thin-Film Spinning Disk Reactor

A thin-film spinning disk reactor (tf-SDR) comprises of one or more rotating disks (10 cm to 1 m in diameter), feed tubes, gas inputs and outputs, a heating/cooling jacket, and a product discharge zone. The feed tube(s) introduces liquids to a point on the disk rotating between 100 to 6000 RPM, that accelerates and subjects them to shear stress. This causes the liquids to thin and stretch as they move outward and permits high rates of heat and mass transfer, which benefits reaction processes [120]. The products in a tf-SDR are ejected towards the wall casing and subsequently collected. The residence time in a tf-SDR is determined by the flowrate, the viscosity of the reagents, the rotational speed, and where the reagents are introduced (Eq. 2.3) [121].

$$t_{\mathrm{res}} = \left(\frac{81\pi^2 v}{16\omega^2 Q^2}\right)^{1/3} (r_{\mathrm{o}}^{4/3} - r_{\mathrm{i}}^{4/3}) \tag{2.3}$$

tf-SDRs are able to produce NPs with varying sizes and morphologies. The particle size varies with the position of reagent introduction onto the rotating disk. For example, a tf-

SDR generates barium sulphate particles with an average size of 5 µm when sodium sulphate is introduced near the center of the rotating disk, and 170 nm when it is introduced near the rim of the disk. In addition, the rotation of the disk affects the morphology of the resulting NPs — rotations of 1100 RPM and 1650 RPM produced spheric and cubic calcium carbonate particles, respectively [120]. In another instance, Mohammadi et al. found that as the rotational speed, flowrate and water/titanium tetra isopropoxide ratio increased, the size and $Đ$ of the resulting NPs decreased. As the flowrate increased from 3.6 mL s^{-1} to 18 mL s^{-1} the median particle size decreased from 12 nm to 3 nm. Furthermore, the median particle size decreased from 12 nm to 2 nm as the water/titanium tetra isopropoxide ratio increased from 6 to 20. Finally, as the rotational speed increased from 42 rad s^{-1} to 126 rad s^{-1}, the median particle size decreased from 15 nm to 2 nm. The tf-SDR consistently produced nano-sized titanium particles compared to the micron-sized particles originating from the stirred-tank reactor (STR); mixing conditions are more intense and uniform in an tf-SDR than a STR [122].

We believe rs-SDRs are better suited for continuous nanoprecipitation. PLA is stable in solution and would otherwise be difficult to collect from the walls of a tf-SDR setup.

2.4.2 Rotor-Stator Spinning Disk Reactor

Rs-SDRs are ideal for multiphase reactions. They differ from their counterpart (the tf-SDR) in two ways. The first, is that the disk(s) in rs-SDRs are encased in a stationary shroud with little distance between the disk(s) and said shroud. The second is that their residence time is solely defined by the reactor volume and the flowrate (Equation 2.4); the entry point of the reagents cannot generally be modified. Moreover, they emphasize intense mixing on top of the high shear forces. The energy from the rotating disks is transferred into the reaction medium, leading to high energy dissipation rates, ϵ, that can reach up to 1×10^5 W kg^{-1} [123]. These high energy dissipation rates result in enhanced mass transfer, heat transfer, and reduced micromixing times.

$$t_{\text{res}} = \frac{V}{Q} \tag{2.4}$$

The initial search strategy for SDRs was modified, in order to distinguish the literature on rs-SDRs from tf-SDRs, to: ("rotor-stator" OR "rotor-stator system" OR "rotor-stator device") AND ("spinning disk reactor" OR "spinning disc reactor"). In the WoS Core Collection, this produced 50 results, including 46 articles, 3 proceeding papers, and 1 letter, dating back to 2010. Most of these articles focus on fundamental studies of heat and mass transfer, residence

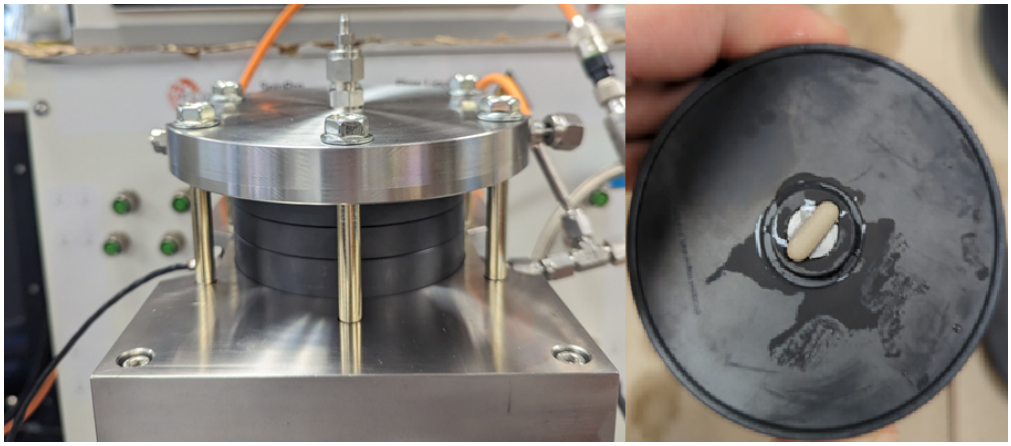

Figure (2.5) (Left) FlowID's R2 three-stage rs-SDR. Each stage is a different disk. There are three inlets and one outlet, the experimental work in the thesis relies on two of the inlets. Maximum disk rotation is 6000 RPM, total allowable flowrate is $120\,\mathrm{mL\,min^{-1}}$. (Right) Top-view of one disk from FlowID's R2 rs-SDR. The pill at the center is to magnetically couple the disk to the reactor's motor.

time distribution, micromixing, and scale-up.

- *Heat and mass transfer*: the volumetric gas-liquid mass transfer per unit volume in an rs-SDR increases with increasing rotational speed and is 40x higher than in bubble columns ($20.5\,\mathrm{m_L^3 m_G^{-3} s^{-1}}$ vs. $0.5\,\mathrm{m_L^3 m_G^{-3} s^{-1}}$) [124]. Liquid-liquid mass transfer rates in the rs-SDR increased from $0.2\,\mathrm{m_{ORG}^3 m_R^{-3} s^{-1}}$ at $10\,\mathrm{rad\,s^{-1}}$ and a water flowrate of $2.5 \times 10^{-6}\,\mathrm{m^3\,s^{-1}}$ to $51\,\mathrm{m_{ORG}^3 m_R^{-3} s^{-1}}$ at $168\,\mathrm{rad\,s^{-1}}$ and a water flowrate of $12.5 \times 10^{-6}\,\mathrm{m^3\,s^{-1}}$. These rates are 25x higher than in packed columns and up to 15x higher than in microchannels [125]. Heat transfer coefficients also increase as a function of the rotational speed, and by extension the rotational Reynolds number. The volumetric heat transfer coefficient increased from $U_{ov}AV_R^{-1} = 0.46 \pm 0.2\ \mathrm{MW/m^3\,K}$ to $U_{ov}AV_R^{-1} = 0.93 \pm 0.2\ \mathrm{MW/m^3\,K}$ as the rotational Reynolds number went from 0 to 4.5×10^5 [126].

- *Residence time*: residence time distribution studies demonstrate that the rs-SDRs can be described by a combination of plug-flow (PFR) and continuously stirred tank reactors (CSTR) thanks to the effects of turbulence and the formation of Von Kármán and Bödewadt boundary layers [127, 128]. The Von Kármán layer forms along the rotor while the Bödewadt layer forms along the stator — a more detailed explanation of flow behaviours in these layers is provided in Section 2.5.

- *Mixing*: hydrodynamically, the rs-SDR operates like a PFR in the radial positions above and underneath the disk, while the high radial positions mimic a CSTR [126].

Experimental micromixing studies based on the Villermaux–Dushman test reaction agree that the mixing follows the engulfment model (E, s^{-1}) [129]. The Villermaux-Dushman reaction (also known as the iodate/iodate reaction) is a parallel competing reaction with an acid-base reaction in a borate buffer and a comproportionation reaction producing iodine. A further reaction between iodine and iodide yields triiodide [130]. In an ideal micromixing scenario, the acid-base reaction is the only one that occurs and no triiodide is made [130, 131]. The engulfment model itself, which describes vortical engulfment of one fluid by another and thus the growth rate of eddies, is a function of the energy dissipation rate, ϵ, and viscosity, ν [132]. In other words, E determines the degree to which mass exchange occurs between a fluid and its surroundings [133]. Overall, micromixing times in an rs-SDR, estimated via the engulfment model, range from 9×10^{-3} s to 1×10^{-4} s for rotational speeds between $10\,\mathrm{rad\,s^{-1}}$ and $180\,\mathrm{rad\,s^{-1}}$ and are indeed a function of ϵ [134]. Lower mixing times are possible with larger values of ϵ and thus rotational speeds. For example, some commercial rs-SDRs can operate at speeds as high as $600\,\mathrm{rad\,s^{-1}}$.

Other experimental research topics in the literature include photochemical oxidation and degradation [135], epoxidation of methyl oleate [136], transesterification of triglycerides [137], and synthesis of $BaTiO_3$ NPs [138]. The central theme in rs-SDR research is process intensification. Moreover, in the entire literature of SDRs (thin-film and rotor-stator), there is no research on the production of polymeric nanoparticles for drug delivery purposes.

This concludes the literature for sub-objective 2 (*Chapter 4: Continuous Nanoprecipitation of Poly(D,L-Lactide) in a Rotor-Stator Spinning Disk Reactor).* For a distilled summary of the literature concerning the synthesis of drug-loaded NPs on a large-scale, we refer the reader to Table 4.1. Overall, there are few experimental studies on rs-SDRs across research domains despite the plethora of applications these reactors are suited for. We are the first to apply the rs-SDR for the production of polymeric nanoparticles and drug-loaded polymeric nanoparticles.

2.5 Hydrodynamics in Rotor-Stator Spinning Disk Reactors

The hydrodynamics of rotor-stator systems is a crucial part in the development of these systems and has been studied in turbomachines [139], centrifugal pumps [140], high-shear mixers [141], and hydrodynamics reactors (e.g., for biodiesel production) [142]. For rs-SDRs specifically, the main elements to investigate are the transitions radius, r_t, and the time-averaged velocity profiles along the Von Kármán (rotor) and Bödewadt (stator) boundary

layers. The transition radius defines the point along the disk where the flow alternates from throughflow-governed to rotation-governed. The former is reminiscent of plug-flow reactors (PFR) while the latter of continuously-stirred tank reactors (CSTR). In addition, r_{t} decreases with increasing Re, gap ratio, and increases with increasing throughflow rates. There are four different flow regimes in which rs-SDRs operate that are a function of the rotational Reynolds number, $\mathrm{Re} = \frac{\omega R^2}{\nu}$, and the rotor-stator gap ratio, $G = h/r_{\mathrm{D}}$, where h is the axial distance between the rotor and the stator, and r_{D} is the radius of the disk. These regimes are classified I through IV and exhibit distinct or merged Von Kármán and Bödewadt boundary layers [143]:

- I - laminar flow with merged Von Kármán and Bödewadt layers and a continuous variation in velocity along h
- II - laminar flow with separated Von Kármán and Bödewadt layers and an inviscid core
- III - turbulent flow with merged Von Kármán and Bödewadt layers and a continuous variation in velocity along h
- IV - turbulent flow with separated Von Kármán and Bödewadt layers and an inviscid core

Regimes I and III are commonly referred to as torsional Couette flow [145], while regimes II and IV are commonly known as Batchelor flow [146]. The inviscid core in regimes II and III is a region in between both boundary layers that has a radial velocity of zero. In chapter 5, we work in regimes I and III. In torsional Couette flow, there are radial inflows in Bödewadt layer and radial outflows in the Von Kármán layer (Figure 2.7). The azimuthal velocity starts at zero at the stator and increases as you progress further along the disk (Figure 2.8). The difference between regimes I and III relate mainly to the azimuthal velocity. In the former case, the increase in velocity from the stator to the rotor is linear, whereas in the latter case, it is not. Moreover, the fluid profiles in the side channel between the edge of the disk and the side wall are reminiscent of toroidal vortices (pockets of upward and downward velocities) in classic Taylor-Couette flow [147].

2.5.1 Macroscopic Flow Behaviour

The flow structures in rs-SDRs are also influenced by the presence or absence of throughflow, often described by $C_w = Q\nu^{-1}r_{\mathrm{D}}$, where Q is the volumetric flowrate, ν is the kinematic viscosity, and r_{D} is the disk radius.

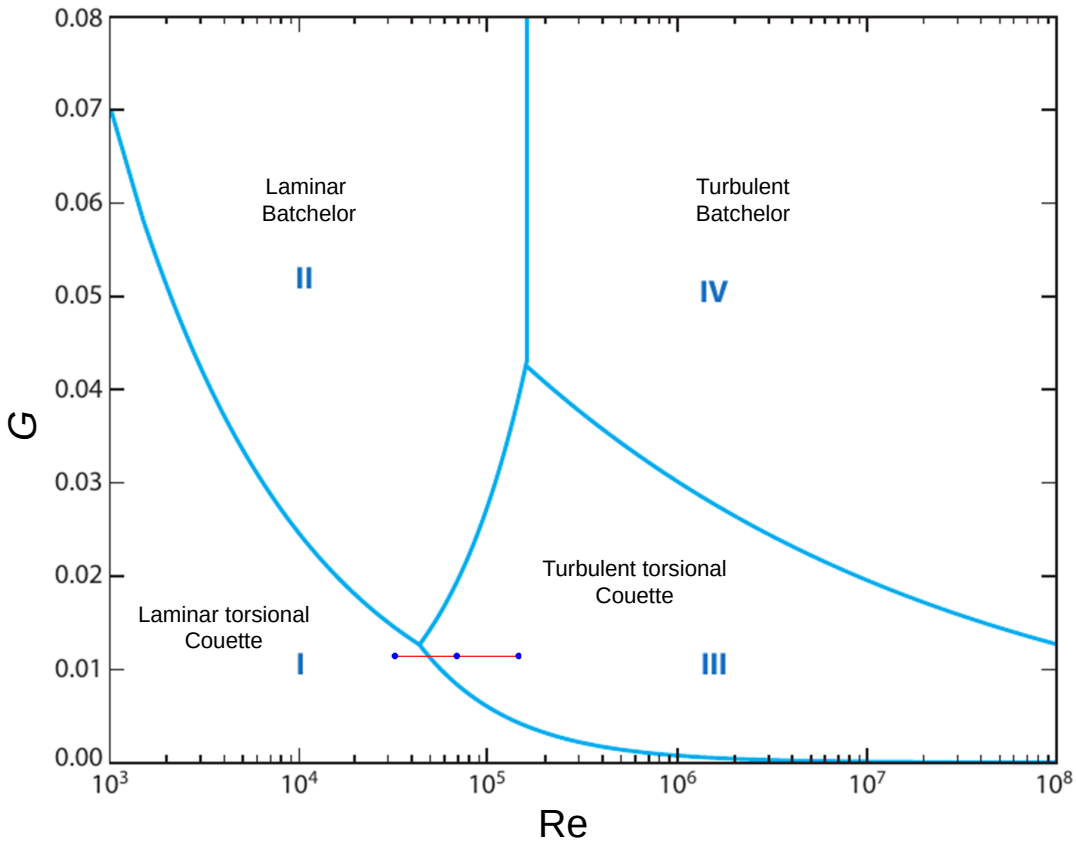

Figure (2.6) Flow regimes in a rs-SDR as a function of G and Re. The blue dots represent the region of operation for Chapter 4 and 5. Adapted from [144].

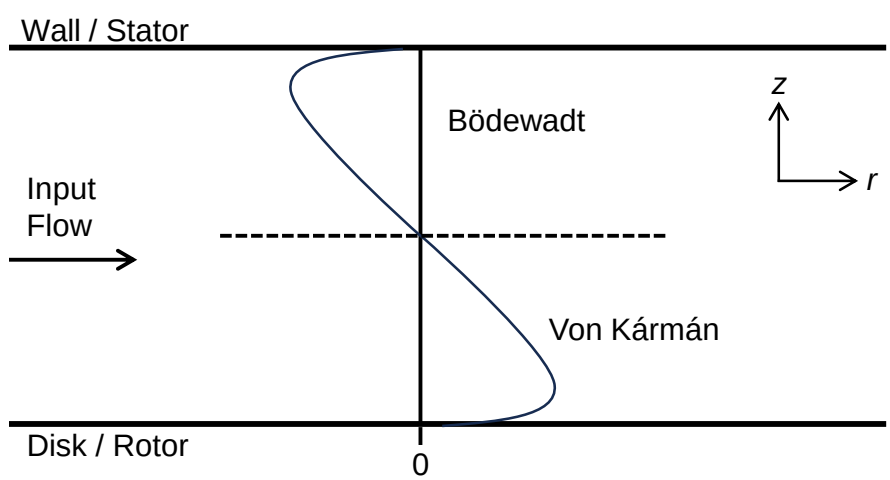

Figure (2.7) Time-averaged radial velocity profile in torsional Couette flow (regime III) in a rs-SDR. Adapted from [144].

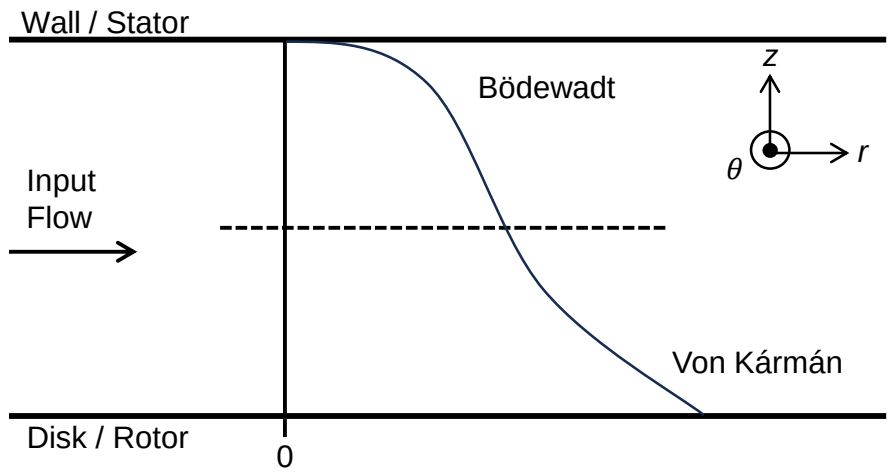

Figure (2.8) Time-averaged azimuthal velocity profile in torsional Couette flow (regime III) in a rs-SDR. Adapted from [144].

- $C_w = 0$ — With no throughflow, the flow along the Kármán layer exhibits centrifugal radial and negative axial velocities; the flow along the Bödewadt layer exhibits centripetal and positive axial velocities [144].
- $C_w > 0$ — Before r_t, and thus PFR/throughflow dominant flow, the radial velocity is positive at all positions and the tangential velocity is zero in the Bödewadt layer; after r_t, the radial velocity stays positive in the Von Kármán layer but becomes negative in the Bödewadt layer [144]. In other words the flow transitions to torsional Couette flow after r_t and radial backmixing occurs.

2.5.2 The Finite Element Method and `Lethe`

We studied the hydrodynamics in rs-SDRs with the Finite Element Method (FEM). It permits us to numerically solve fluid dynamic problems that involve fluids; the Navier-Stokes equations (Equation 2.6) for incompressible fluids is approximated within each element of the discretized (into small hexahedra) fluid domain [148].

$$\nabla \cdot \mathbf{u} = 0 \tag{2.5}$$

$$\frac{\partial \mathbf{u}}{\partial t} + (\mathbf{u} \cdot \nabla)\mathbf{u} = -\nabla p^* + \nu \nabla^2 \mathbf{u}. \tag{2.6}$$

where $\mathbf{u}$ is the fluid velocity, p^* is reduced pressure (p/ρ, where p is the pressure and ρ the

density of the fluid), and ν is the kinematic viscosity. This provides insights into the velocity fields of rs-SDRs with different operational parameters. In this thesis, the flows in an rs-SDR are solved using `Lethe`, an open-source high-order computational fluid dynamics (CFD) stabilized continuous Galerkin FEM solver for incompressible flows [149]. It relies on the open source library for finite element modeling, deal.II [150]. `Lethe` solves the Navier-Stokes equations in a matrix-free fashion using the Newton-Raphson method [151]. Matrix-free solvers do not require large data structures that need to be stored and later accessed for the computations, they are not bounded by memory or bandwith [151].

2.5.3 Experimental Studies

Itoh et al. studied turbulent flows in an enclosed rotating disk and focused on the boundary layers; they discovered that the boundary layer at the stator becomes turbulent at much lower Re compared to the boundary layer at the rotor (8×10^3 vs. 1.6×10^5) [152]. Another study explored the flow transitions between a rotating and stationary disk at different G and Re. At low aspect ratios ($0.0071 < G < 0.0179$), they observed spiral rolls (at Re $= 90 \times 10^3$), solitary waves (at Re $= 127 \times 10^3$), and spots (at Re $= 167 \times 10^3$) that appear in the laminar flow that eventually becomes turbulent [153]. At intermediate aspect ratios ($0.0179 < G < 0.0714$), they observed stationary spiral rolls (at Re $= 51 \times 10^3$), and even the superposition of circular rolls [153]. At high aspect ratios ($0.0714 < G < 0.143$), they observed circular rolls (at Re $= 17 \times 10^3$) and spiral rolls coexisting with each other and propagating radially outward [153]. Poncet et al. focused on the transition between Batchelor flow and Stewartson flow (one boundary layer on the rotor) at $C_w = 0$, 2579, 5159, 10317, and $G =$ 0.012, 0.036. At a constant C_w of 5159, the flow transitions from Stewartson to Batchelor-type as Re increases (beginning at Re $= 1 \times 10^6$) [154]. At C_w of 5159, Re of 1×10^6, and a G of 0.012, the flow is mainly Stewartson. At $G = 0.036$, the type of flow depends on the radial position — near the center of the disk, the flow is Stewartson, while near the edge it becomes Batchelor [154]. A similar study looked at these same transitions with a two-component laser Doppler velocimeter (LDV) but also included a negative C_w and a higher Re (4.15×10^6). The results at positive C_w (1976 to 9881) were in line with those previously stated. At negative C_w (-1976 to 9881), however, the flow is Stewartson, with fully centrifugal flow at all axial locations [155]. It should be noted, that [155] define $C_w < 0$ and $C_w > 0$ as centrifugal and centripetal throughflows, respectively, whereas most of the other studies (like [156]) and the work done in Chatper 5 are reversed ($C_w < 0$ is centripetal and $C_w >$ 0 is centrifugal). In a combination of simulation and experiments for biodiesel synthesis, Wen and Petera found that triglyceride conversion increases as G and the rotational speed decreases [157]. Conversions at $G = 0.1$ peak at 54 % at $105\,\mathrm{rad\,s^{-1}}$, whereas at $G = 0.2$ and

the same conditions the conversion drops to 40 %. As the rotational speed increases so does backflow, which hampers conversion (e.g. 54 % at 105 rad s^{-1} to 46 % at 209 rad s^{-1}) [157]. In conclusion, their results demonstrated that G and high rotational speeds produce large shear forces that intensify mixing and enhance conversion. However, at excessive rotational speeds (e.g., 209 rad s^{-1}) the backmixing also intensifies and reduces conversion [157].

2.5.4 Theoretical Studies

The volume of fluid plus $\kappa-\epsilon$ model simulated two types of flows in a rs-SDR: film and filament flow. The former is present at < 84 rad s^{-1} across flowrates (10 mL min^{-1} to 160 mL min^{-1}), while the latter is present at > 84 rad s^{-1} across the same flowrates [158]. In a different study, a spectral vanishing viscosity method for LES simulated the flows in a rotor-stator system at a G of 5 and a Re between 10×10^5 to 10×10^6. At Re $= 10 \times 10^5$ the boundary layer at the stator is turbulent while the one at the rotor is laminar. At Re $= 4 \times 10^5$ the rotor boundary layer starts becoming turbulent, and at Re $= 10 \times 10^6$ both layers are firmly turbulent [159]. These results were verified experimentally with LDV. Another LES study looked at a much larger G (36.5) for Re between 0.75×10^5 to 3.75×10^5. At Re $= 1.5 \times 10^5$, the boundary layer at the stator transitions to turbulence, followed by the boundary layer at the rotor at Re $= 2.25 \times 10^5$ forming spiral structures before transformation. At Re $= 3.75 \times 10^5$, the flow is fully turbulent with a thicker boundary layer at the stator, which produces stronger anisotropic turbulence [160]. At much lower G (0.03), Re $= 3.2 \times 10^4$ to 5.2×10^5, and $C_w = 150$, the flow is turbulent (regime III) and transitions from PFR to CSTR behaviour at 15 % of the radius of the disk at 75 rad s^{-1} [156]. These results were also validated experimentally with residence time distribution tests. Mathematical models are also developed to predict flow characteristics. For example, Bailey et al. have derived a predictive mathematical representation to determine the swirl ratio, pressure, and torque, in rotor-stator cavities of typical gas turbines. The swirl ratio is defined as the ratio between the tangential velocity of the core and that of the disk. As G increases from 0.05 to 0.5, the swirl ratio decreases by 40 % near the edge of the disk [161]. In addition, a rotating hub and a stationary shroud produced a swirl ratio of 0 near the center of the disk compared to 0.4 with a stationary hub and rotating shroud [161]. One fundamental paper studied the flow of a Newtonian fluid in the region between an infinitely long rotating disk and an infinitely long stationary disk, numerically. At $\mathrm{Re}_h = 100$, where $\mathrm{Re}_h = \omega h^2 v^{-1}$, the flow has a non-viscous core in the azimuthal velocity profile. At $\mathrm{Re}_h = 300$, the core is present in the axial and radial velocity profiles as well; at $\mathrm{Re}_h > 300$, the flow is Batchelor-type [162]. Interestingly, the flow profiles were also calculated with an analytical power series approximation that accurately described said flow profiles [162].

This concludes the literature for sub-objective 3 (*Chapter 5: Mixing and Hydrodynamics in a Rotor-Stator Spinning Disk Reactor*). For a distilled summary of the literature concerning the different studies of hydrodynamics in rs-SDRs, we refer the reader to Table 5.1.

2.5.5 Main Research Gaps

Overall, there are research gaps relating to:

- The dielectric properties of D,L-lactide as well as solvent selection for ROPs in microwave reactors.
- Easy-to-operate and scale-up technologies for industrial-scale production of drug-loaded NPs.
- Characterization of bulk mixing and fluid profiles in commercial rs-SDRs.

CHAPTER 3 ARTICLE 1 – MICROWAVE-ASSISTED POLY(D,L-LACTIDE) SYNTHESIS IN TOLUENE AND TETRAHYDROFURAN

Nicolas Patience[a], Halie Mei Jensen,[b] Xavier Banquy,[c] Daria C. Boffito[a]

Article submitted to Journal of Advanced Manufacturing and Processing on December 29, 2024

[a]Department of Chemical Engineering, Polytechnique Montréal, Montréal, Canada

[b]Department of Electrical, Computer, and Biomedical Engineering, Toronto Metropolitan University, Toronto, Canada

[c]Department of Pharmacy, Université de Montréal, Montréal, Canada

Author contribution for Nicolas Patience: Conceptualization, Investigation, Writing - original draft, Methodology, Validation, Visualization, Writing - review and editing, Software, Formal analysis, Project administration, Data curation, Supervision, Resources

3.1 Abstract

Poly(D,L-lactide) is a biocompatible and biodegradable polymer with applications in the biomedical field (drug delivery, implants) and packaging. Conventional synthesis with stannous octoate is slow ($> 4\,\mathrm{h}$) and can climb to over $30\,\mathrm{h}$. In order to reduce reaction times, we developed a microwave reactor process to ring-open polymerize D,L-lactide to form poly(D,L-lactide) in the presence of stannous octoate and an initiator, benzyl alcohol. We evaluated the suitability of toluene and tetrahydrofuran as solvents at $130\,^{\circ}\mathrm{C}$, $150\,^{\circ}\mathrm{C}$, and $170\,^{\circ}\mathrm{C}$ for the polymerization. Their respective dielectric loss (ϵ'') values are 0.1 and 0.35. Compounds with larger dielectric loss values are better at converting microwave energy to heat. The microwave's power input peaked at $420\,\mathrm{W}$ to reach $170\,^{\circ}\mathrm{C}$ with toluene, whereas with tetrahydrofuran the peak was $330\,\mathrm{W}$; afterwards, the power input to maintain that temperature was $10\,\mathrm{W}$ for both solvents. A reaction in toluene at $170\,^{\circ}\mathrm{C}$ after $1\,\mathrm{h}$ produced poly(D,L-lactide) with a molecular weight of $31\,\mathrm{kDa}$ and a dispersity index of 1.5. In tetrahydrofuran, at the same temperature, the molecular weight peaked at $11\,\mathrm{kDa}$ after $4\,\mathrm{h}$ with a dispersity

index of 1.2. Moreover, in the absence of microwaves the polymerization does not occur. Tetrahydrofuran is hygroscopic and water cleaves poly(D,L-lactide) chains resulting in a lower molecular weight despite the longer reaction time and larger dielectric loss compared to toluene, a water immiscible solvent.

3.2 Introduction

Polylactic acid (PLA) is an aliphatic polyester derived from α-hydroxy acids. It is a biocompatible and biodegradable polymer that degrades by hydrolysis of its ester bonds [12]. In addition, it is produced from lactic acid, which in turn is sourced from renewable feedstock (e.g., corn, sugarcane). These properties have cemented PLA as one of the most promising replacements for petroleum-based plastics, with uses in food packaging, medical device manufacture, and drug delivery purposes [15, 163, 164, 165]. PLA's monomer, lactic acid (LA), is an ingredient in the food industry and functions as an acidic flavouring buffer and a bacterial inhibitor in processed foods. Bacterial fermentation with lactic acid bacteria (LAB) accounts for 90 % of all lactic acid production. This process consumes little energy, operates at low temperatures, selectively produces D-lactic acid or L-lactic acid, and consumes renewable carbohydrate biomass [12]. Polymerization of D- and L-lactic acid yields poly-D-lactic acid (PDLA) and poly-L-lactic acid (PLLA). The former is amorphous while the latter is semi-crystalline [13]. The conventional method for synthesizing PLA requires heating lactic acid or lactide above 100 °C for 4 h or more [10], and with no dedicated initiator this climbs to over 30 h [166]. On the other hand, NatureWorks LLC patented a continuous ring-opening polymerization process of lactide with a tin-based catalyst at 160 °C for 8 h [167]. ROP of lactide to form PLA follows a coordination-insertion mechanism [168].

Microwave irradiation is a non-conventional way to provide energy to chemical processes and belongs to the pool of process intensification technologies [33] and provides volumetric and uniform heating [34]. It has proved to increase reaction rates for polymerizations (step-growth, ring-opening) compared to conduction heating [169]. Some advantages include faster heat transfer, which leads to shorter reaction times as well as inner heating of the reactor contents and reduced heat loss [170]. The two mechanisms of microwave heating are dipolar polarization and ionic conduction [35, 36]. In the former, molecules with dipoles rotate as a result of the electromagnetic field and in turn generate heat via molecular friction and collisions [37, 38]. In the latter, the microwave makes charged particles oscillate to generate heat through collisions [37, 39]. The three parameters that determine a material's ability to interact with microwaves are the loss tangent ($\tan\delta$, Equation 3.1), the dielectric constant

(ϵ), and the dielectric loss (ϵ'') [171].

$$\tan\delta = \epsilon''/\epsilon \tag{3.1}$$

ϵ represents the ease with which a material becomes polarized in the presence of an electric field, ϵ'' is the conductance of a material, and $\tan\delta$ is a parameter that indicates a material's efficiency in converting microwave energy into thermal energy [41]. Microwave heating accelerates the ROP of lactide compared to conduction heating — 24 h to produce PLA with a weighted-average molecular weight (MW) of 18 kDa at 140 °C compared to 6 h for 20 kDa at 160 °C [172, 173]. Ultimately, all microwave reactors operate at a frequency of 2.45 GHz [174] to avoid interfering with other microwave frequencies, for example, FM radio plus TV broadcasts (0.08 GHz to 0.8 GHz), mobile phones (0.045 GHz to 1.98 GHz), radar (0.03 GHz to 300 GHz) [175].

There are many viable catalysts for the ROP of lactide — so far, in microwave reactors, researchers have tested tin-based catalysts, titanium-based catalysts [66, 67], zinc-based catalysts [176], and solid super-acids [177]. The most common catalyst for ROP is tin(II) octoate ($Sn(Oct)_2$) — stannous octoate. It is soluble in lactones, can produce low and high MW PLA (from thousands to millions of Da), and is FDA-approved [12, 178]. However, the two octoate groups must be substituted by two alkoxide groups to form tin(II) alkoxide, the true initiator of the polymerization. OH groups derived from alcohols typically enable this substitution. $Sn(Oct)_2$ also reacts with water, hydroxy acids, and other OH-bearing impurities in the reaction mixture [29]. This increases the dispersity ($Đ$) of the resulting PLA because more chains of likely unequal length are initiated. Kinetically, ROP of lactide is first order [30]. The polymerization rate reaches a maximum when the ratio of $Sn(Oct)_2$ and the alcohol is 0.5 [29, 30]. In addition, the polymerization involves reversible deactivation and intermolecular, and intramolecular (back-biting) transesterification reactions, which decrease the final MW of PLA [168, 179] and prevent steady state conditions. We denote an umbrella term — MW reduction events — for the processes (depolymerization and transesterification) that reduce the final MW of PLA. These processes are also catalyzed by $Sn(Oct)_2$, and other metals (e.g., Zn, Al, Fe) [180] and are exacerbated by long reaction times (> 2 h) and high temperatures (> 180 °C). Depolymerization involves chain scission of the polymer due to oxidative cleavage [181] while transesterifications (mainly between polymer chains) modify the polymer end-groups and consequently the MW and dispersity [168].

L-lactide polymerized in a domestic microwave oven in the presence of $Sn(Oct)_2$ at 180 W, 360 W and between 5 min to 30 min at monomer-to-initiator (M:I) ratios of 1040/1, 2534/1, 5069/1. As the monomer-to-initiator ratio increased, so did the MW of the PLA. Fewer

initiator molecules formed fewer but longer chains. An M:I ratio of 2534:1 for 20 min at 180 W produced the highest MW (77 kDa) with a $Đ$ of 2 [49]. Similarly, another ROP of L-lactide in a microwave at 180 °C, 180 W, a M:I ratio of 5069:1 with $Sn(Oct)_2$ and no initiator produced PLA with a MW of 11 kDa — further microwave irradiation degraded the PLA [50]. In addition, [51] compared a second catalyst, dibutyltin dimethoxide (DBTM), to $Sn(Oct)_2$ at 150 °C with ratios of 1040:1, 2534:1, 5069:1, 10 069:1. DBTM outperformed $Sn(Oct)_2$ producing a MW a 30 kDa with a $Đ$ of 1.66 versus a MW of 22 kDa and a $Đ$ of 2 after 20 min. A microwave reactor under vacuum with N_2 sparging assisted the ROP of D-lactide in the presence of $Sn(Oct)_2$, BnOH, and toluenesulfonic acid (TSA). $Sn(Oct)_2$ paired with BnOH at an unspecified ratio was added at 0.03 % by weight of lactide and TSA at 0.4 % by weight of lactide. The highest MW was 20 kDa after 25 min at 280 W and 215 °C [31]. In another instance, L-lactide polymerized and grafted onto polyhedral oligomeric silsesquioxanes (POSS) in the presence of $Sn(Oct)_2$ and in the absence of solvent. At 45 W, 120 °C, and 45 min, a catalyst concentration of 1.5 wt% with respect to lactide and a molar ratio of L-lactide:POSS-$(OH)_{32}$ of 600 synthesized PLA tails with a molecular number of 50 kDa [54]. Alternatively, castor oil and $Sn(Oct)_2$ initiated the polymerization of L-lactide in a microwave reactor at 150 W and lactide:castor oil ratios ranging from 113 to 533 The optimal conditions were a ratio of 533:1 for 50 min which produced a MW of 25 kDa and a $Đ$ of 1.18 [55].

Thauvin et al. compared the effectiveness of $Sn(Oct)_2$ to 1,8-diazabicyclo(5.4.0)undec-7-ene (DBU) for the synthesis of PEG- PLA diblock copolymers; the monomers were mPEG2000 and D,L-lactide [56]. Conversion with DBU in chloroform after 5 min was 100 %, 94 %, and 40 % at 100 °C, 170 °C, and 60 °C, respectively. $Sn(Oct)_2$ was active at 170 °C and converted 95 % of the lactide but was inactive below 100 °C. Polyhydroxyalkanoates (PHAs) — thermoplastic polyesters produced from bacterial microorganisms under stress (reduced access to nutrients) — can also initiate the ROP of lactide. Microwave irradiated a mixture of D,L-lactide, PHA, toluene and $Sn(Oct)_2$ at 115 °C for 5 min. A lactide:PHA ratio of 250:1 produced a MW of 81 kDa with a $Đ$ of 1.8 and a conversion of 85 % [182]. ROP of lactide is quicker and achieves higher MWs in a microwave reactor compared to a vacuum-sealed vessel with conventional heating or a pressurized reactor. Conventional heating in a vacuum sealed vessel led to PLA with a MW of 250 kDa and a $Đ$ of 3 after 150 h at 150 °C. The pressurized reactor produced PLA with a MW of 190 kDa and a $Đ$ of 2.4 after 6 h at 120 °C and 140 kPa. In contrast, microwave irradiation led to PLA with a MW of 300 kDa and a $Đ$ of 1.7 at 100 °C for 30 min [59]. All monomer:initiator (M:I) ratios were 5000:1. A microwave-assisted ROP method synthesized PLA-PEG copolymers in 5 min in chloroform at 125 °C; the catalysts were $Sn(Oct)_2$ and DBU. The initiators were D,L-lactic acid and mPEG2000. A M:I ratio of

278:1 resulted in PLA-PEG polymers with a MW of 40 kDa and conversions of up to 35 % or 83 % with $Sn(Oct)_2$ or DBU, respectively [60]. Overall, despite plentiful literature (Table 3.1) on microwaves and the polymerization of lactide, none mention the dielectric properties of the reagents. The property of interest is the dielectric loss as it represents the amount of microwave energy released as heat. Compounds with larger dielectric loss values will attain desired temperatures with less power input (Figure 3.1).

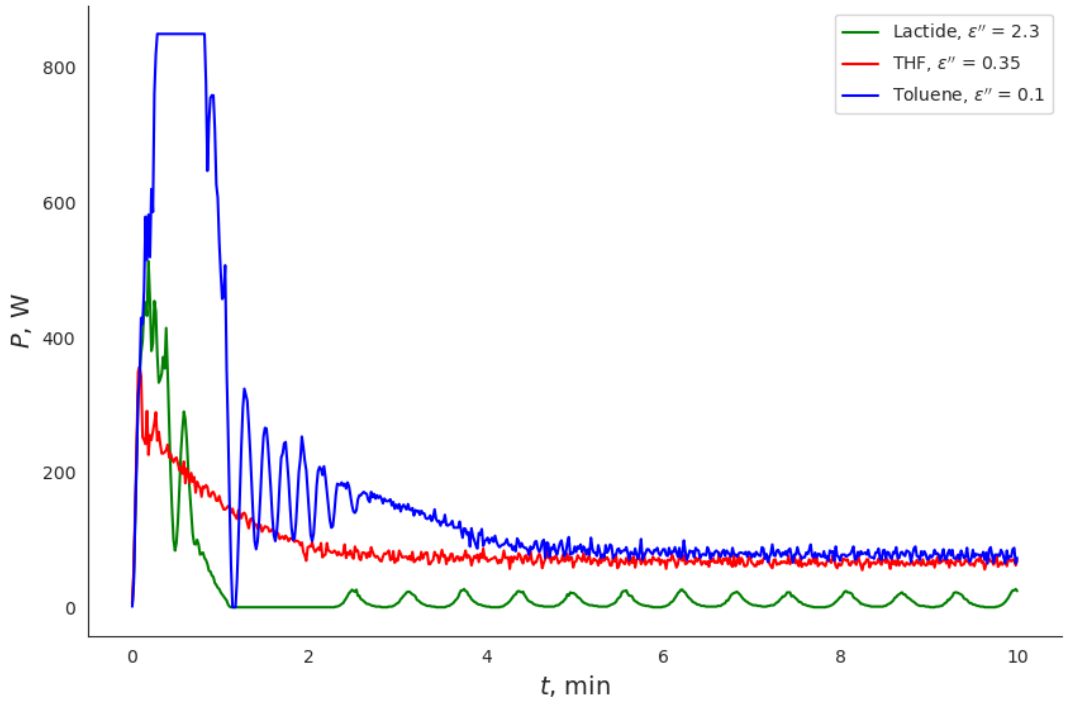

Figure (3.1) Power required to heat 4 mL of solvent to 170 °C. The values associated to each solvent are the dielectric loss value.

The literature lacks data on the dielectric properties of D,L-lactide as well as solvent selection for ring-opening polymerizations in microwave reactors. We thus evaluated the suitability of six different solvents (toluene, THF, acetone, acetonitrile, dimethylformamide (DMF), and dimethyl sulfoxide (DMSO) with dielectric loss values of 0.096, 0.348, 1.12, 2.33, 6.1, and 37.1, respectively) in the synthesis of PLA in a lab-scale Monowave 400 microwave reactor from Anton Parr. In addition, for the first time, we measure the dielectric properties of D,L-lactide at 2.45 GHz, the frequency at which the microwave reactor adopted in this study operates. Moreover, the high operational capacities of the latter (300 °C, 3000 kPa) permitted the polymerization of D,L-lactide high temperatures (130 °C, 150 °C, 170 °C) in THF. In other batch systems and modified domestic microwaves, the pressure generated from boiling THF

Table (3.1) Literature Summary. The conversion column reports the highest conversion achieved. The text in parentheses beside the conversion values represents the technique that determined said conversion. The * indicates that the authors of the study have not reported conversion and we are calculating it as we did in this study.

Reference	Catalyst	Solvent	M:I ratio	°C / W	min	MW, kDa	Đ	% conv.
[66]	Titanium-based	None	200:1	130 / 200	80	27	1.2	88 (^{1}H NMR)
[67]	Titanium-based	None	500:1	180 / 400	45	43	2.4	83 (^{1}H NMR)
[176]	Zinc-based	Toluene	-	130 / -	180	1.3	1.8	96 (^{1}H NMR)
[177]	Solid-Super Acids	None	-	260 / -	50	22	-	-
[49]	$Sn(Oct)_2$	None	2534:1	- / 180	20	77	2	11*
[50]	$Sn(Oct)_2$	None	5069:1	180 / 180	20	11	-	2*
[51]	$Sn(Oct)_2$	None	5069:1	150 / -	20	102	1.6	9*
[51]	DBTM	None	2534:1	150 / -	10	40	1.7	7*
[31]	$Sn(Oct)_2$	None	-	215 / 280	25	20	3.5	-
[54]	$Sn(Oct)_2$	None	600:1	120 / 45	45	50	-	-
[55]	$Sn(Oct)_2$	None	533:1	- / 150	50	25	1.2	90 (absent)
[182]	$Sn(Oct)_2$	Toluene	250:1	115 / -	5	81	1.8	85 (gravimetry)
[59]	$Sn(Oct)_2$	None	5000:1	100 / -	30	300	1.7	25*
[60]	$Sn(Oct)_2$	Chloroform	278:1	125 / -	5	40	-	100
This work.	$Sn(Oct)_2$	Toluene	380:1	170 / -	60	31	1.5	34*
This work.	$Sn(Oct)_2$	THF	380:1	170 / -	240	11	1.2	9*

at these temperatures would be dangerous. Furthermore, we developed a statistical model to predict MW and applied it to other microwave polymerization data in the literature.

3.3 Experimental

3.3.1 Materials

We purchased D,L-lactide, $Sn(Oct)_2$, anhydrous toluene, and benzyl alcohol (BnOH) from Sigma-Aldrich. We purchased THF with butylated hydroxytoluene (BHT) as a stabilizer, DMF, methanol, ethanol, and acetone from Fisher Scientific. All reagents, aside from D,L-lactide, were used without further treatment or purification. D,L-lactide was first recrystallized in ethanol and then in toluene and left to dry overnight in an oven under vacuum at 50 °C. It was then stored in the fridge at 4 °C under a nitrogen atmosphere. We did all the experiments with the same batch of purified lactide and within a 2-week timeframe to minimize variation in water content or other impurities. According to a Karl-Fischer analysis the water content of THF and BnOH was 250 ppm, and 300 ppm, respectively. The anhydrous toluene had less than $< 0.001\,\%$ water. $Sn(Oct)_2$ cannot undergo Karl-Fischer titration because it reacts with the titrant (Composite 5 from Honeywell). In addition, we did not distill it to remove impurities such as 2-ethylhexanoic acid because it reappears shortly after distillation [183]. Thus, its water content is unknown.

Solvent List

The CEM Corporation has a list of common solvents and their dielectric loss values on their website (Table 3.2).

Table (3.2) Solvents and their dielectric loss values

Solvent	Dielectric loss (ϵ'')
Ethylene glycol	50
Formic acid	42
DMSO	37
Ethanol	23
Methanol	21
Nitrobenzene	21
1-Propanol	15
2-Propanol	15
Water	9.9
1-Butanol	9.7
NMP	8.9
Isobutanol	8.2
2-Butanol	7.1
2-Methoxyethanol	6.9
DMF	6.1
o-Dichlorobenzene	2.8
Acetonitrile	2.3
Nitromethane	2.3
MEK	1.5
1,2-Dichloroethane	1.3
Acetone	1.1
Acetic acid	1.1
Chloroform	0.45
Dichloromethane	0.38
Ethyl Acetate	0.35
THF	0.35
Chlorobenzene	0.26
Toluene	0.1
o-Xylene	0.05
Hexane	0.04

We eliminated all solvents that bear any OH groups. An excess of hydroxyl moieties hinders polymerization by deactivating the catalyst, inducing chain scission, hydrolyzing PLA's ester linkages, and increasing chain transfer reactions [29, 181, 184]. All these processes result in a PLA with a lower MW and higher dispersity. Furthermore, we excluded ni-

trobenzene as it is highly toxic and nitromethane for the risk of explosion at our reaction conditions. We then evaluated the suitability of toluene, THF, acetone, acetonitrile, DMF, and DMSO with dielectric loss values of 0.096, 0.348, 1.12, 2.33, 6.1, and 37.1, respectively (table 3.2). Chlorobenzene, chloroform, and o-xylene are also suitable candidates but toluene is more common and was selected as the low dielectric loss solvent. Dichloromethane and hexane could function as low-dielectric-constant solvents but their boiling points are lower than toluene (40 °C and 69 °C versus 110 °C) and the pressure in the system at 170 °C with THF (boiling point = 66 °C) already reaches 800 kPa. Our vial caps for the reactor cannot withstand pressures above this for reaction times over 4 h, at which point they are already too deformed to be used again. Thus, we retained toluene and THF for the polymerization experiments.

3.3.2 Microwave Synthesis

The MWs of synthesized PLAs at identical reaction conditions differed across batches of re-crystallized D,L-lactide as well as different bottles of $Sn(Oct)_2$. For example, different fresh bottles of $Sn(Oct)_2$ produced lower MW PLAs compared to a one-year old bottle. Thus, to ensure reproducibility, all experiments were done with the same batch of re-crystallized D,L-lactide and $Sn(Oct)_2$ within the span of two weeks. An oven at 105 °C dried all glassware prior to the reactions to eliminate any traces of water. The reactor vials (made of quartz) were loaded with THF or toluene, $Sn(Oct)_2$, BnOH as the initiaitor, D,L-lactide and then filled with N_2. The amount of solvent and D,L-lactide was constant at 4 mL and 2 g, respectively. The molar ratios for D,L-lactide:$Sn(Oct)_2$ and $Sn(Oct)_2$:BnOH were fixed at 1550 and 0.25. On average, the monomer:initiator (D,L-lactide:BnOH) molar ratio was 380. The polymerization did not occur at D,L-lactide:$Sn(Oct)_2$ molar ratio of 3000. At 100, it is difficult to eliminate the catalyst from the synthesized PLA. The rest of the ratios are dependent on and derived from the D,L-lactide:$Sn(Oct)_2$ ratio. The reaction lengths and temperatures ranged from 0.25 h to 6 h and 130 °C to 170 °C. We precipitated the resulting PLA in a cooled methanol:water (3:1 volume ratio) bath twice and then evaporated any residual solvent in a furnace operating at 100 °C for 6 h and then 60 °C for 18 h to remove toluene first and then water. In cases where THF was the solvent, the furnace operated at 60 °C for 24 h. The samples were stored in vials in N_2 and placed in fridge at 4 °C. Theoretical values for number-average molecular weights of PLA can be predicted from the monomer-to-initiator ratio and the actual conversion of lactide to PLA [29, 185, 186, 187, 188]. We assume 100 % conversion to calculate the maximum number-average molecular weight possible for our PLA. We then divide this value with our experimental data to yield our actual conversion. In our case, we were required to purify the polymers after the reactions and store them for several

days before NMR analysis. As little to no free monomer remains after purification, calculating conversion (%) from NMR was not feasible. The MW values shown in the text refer to the weighted-average molecular weight unless otherwise specified. The number-average molecular weight served only to calculate the conversion. All experiments were conducted in an Anton Paar Monowave 400 microwave reactor. Temperature, pressure, and power input were recorded for the duration of the reactions. Its operational capacities are 300 °C and 3000 kPa and a max power input of 850 W.

3.3.3 Characterization

Proton Nuclear Magnetic Resonance (^{1}H NMR)

A Bruker AV-III 400 MHz spectrometer confirmed the structure of the PLA; samples were dissolved in $CDCl_3$. We analyzed the data with the help of the NMRium software. GPC was the method of choice to determine the molecular weight (number-average and weighted-average) as ^{1}H NMR's resolution begins to suffer and sensitivity decreases at higher molecular weights; purity also becomes an issue [189].

Gel Permeation Chromatography (GPC)

A Thermo Scientific UltiMate 3000 HPLC (high performance liquid chromatography) with a GPC module and columns (PL1110-6504, PL1510-1520, the latter being a guard column) from Agilent determined the MW of the PLA samples. THF eluted the samples at a flow rate of 1 mL min^{-1} at room temperature. We dissolved PLA samples of 0.1 g in 2 mL of THF and then filtered them with PTFE syringes (13 mL diameter, 0.2 µm pore size). A conventional calibration was done with polystyrene standards (from 0.3 kDa to 100 kDa) and a refractive index detector. However, this is a relative technique. The Mark-Houwink-Sakurada (MHS) equation enables the conversion of the MW values from relative ones to absolute ones. It relates the intrinsic viscosity of polymers to empirical constants (k, α) that depend on the analysis conditions (polymer, solvent, temperature) [190]. It is ever-present in the MW analysis of polymers (e.g., chitosan [191], acrylamides [192], cellulose [193]) and dates as far back as the 1980s for atatic polystyrene [194]. To correct the values of our PLA, we adopted a modified version of the MHS equation [168, 190] (Equation 3.2). The constants for k and α were taken from the literature; for polystyrene [194] and PLA [195] in THF the values are 0.014, 0.70, 0.014, and 0.75, respectively. However, we analyzed the uncorrected MW data for direct comparison with the microwave-synthesized PLA literature, much of which does not report any MHS corrections.

$$\log M_{\mathrm{X}} = (\frac{\alpha_{\mathrm{std}} + 1}{\alpha_{\mathrm{X}} + 1}) \log M_{\mathrm{std}} + (\frac{1}{\alpha_{\mathrm{X}} + 1}) \log \frac{k_{\mathrm{std}}}{k_{\mathrm{X}}} \tag{3.2}$$

Differential Scanning Calorimetry (DSC)

A Q2000 DSC (TA Instruments) ramped the temperature from 40 °C to 150 °C at 10 °C/min in N_2 and stabilized at this upper temperature for 10 min before returning to 40 °C for a 2nd cycle. A hermetic aluminum pan held the samples.

Thermal Gravimetric Analysis (TGA)

A TGA Q50 (TA Instruments) operated with N_2, a mass flow of 40 mL min^{-1} and a ramp of 10 °C min^{-1} up to 400 °C and maintained for 20 min.

Dielectric Property Measurement of D,L-Lactide

We measured the dielectric properties of our D,L-lactide with the HP 85070 dielectric probe kit at 2.45 GHz. The probe was calibrated in air and water at room temperature. The loss tangent, dielectric loss, and dielectric constant for lactide at room temperature were 0.017, 0.04, and 2.33. Thus, it requires more power to heat lactide alone compared to it being coupled with a solvent bearing a higher dielectric loss value.

3.4 Results and Discussion

3.4.1 Solvent Selection

Two solvents were appropriate for the experiments, toluene and THF. $Sn(Oct)_2$ and BnOH, the catalyst and initiator, respectively, were not soluble in acetone, acetonitrile, and DMSO — they formed cloudy mixtures. DMF is also unsuitable as it reacts violently with tin-based compounds (i.e., $Sn(Oct)_2$). After less than an hour at 170 °C the solution degraded and blackened.

3.4.2 Evolution of the Experimental Design

The initial iteration of the experimental design was a partial factorial that considered temperature and time as the two primary variables at three levels (2 h, 4 h, 6 h and 130 °C, 150 °C, 170 °C) and solvent at two levels (THF - $\epsilon'' = 0.348$, toluene - $\epsilon'' = 0.096$). It comprises the first 13 experiments of Table 3.3. In these experiments with toluene, the variation of the $Đ$ and MW across the times and temperatures were minimal — all the reactions produced

Table (3.3) Design of experiments. The solvent column lists the dielectric loss values (0.096 = toluene, 0.348 = THF). The experiment number refers to the order in which the experiments were completed. The MHS-Mn column lists the corrected values for the number-average molecular weight.

t, h	T, °C	Solvent	MW (kDa)	Mn (kDa)	MHS-Mn (kDa)	Conv. (%)	$Đ$	Exp.
0.25	170	0.096	8	4.2	3.3	7	1.9	17
0.5	150	0.096	18	12	9.2	25	1.5	16
0.5	150	0.348	4.4	4.1	2.9	7	1.1	18
0.5	170	0.096	17	11	8.2	20	1.6	15
1	170	0.096	31	21	16	34	1.5	14
2	130	0.096	23	18	13	35	1.3	2
2	130	0.348	1.5	1.4	1.1	3	1.1	13
2	150	0.348	4.5	4.1	3.2	7	1.1	8
2	170	0.096	27	18	14	32	1.5	1
2	170	0.348	5.2	4.7	3.7	9	1.1	4
4	130	0.348	4	3.6	2.9	7	1.1	10
4	150	0.096	26	17	13	33	1.5	11
4	170	0.348	11	9.2	7.1	17	1.2	5
6	130	0.096	27	18	14	35	1.5	9
6	130	0.348	4.2	3.8	3.0	7	1.1	12
6	150	0.348	6.7	6.1	4.8	11	1.1	3
6	170	0.096	26	16	12	33	1.6	7
6	170	0.348	3.4	3.1	2.5	6	1.1	6

MWs between 23 kDa to 27 kDa (Figure 3.2). Thus, we assumed that the levels for time were insufficient to identify the growth of the chains and as a result added 3 experiments. One at 1 h, the other at 0.5 h, and the last at 0.25 h. The MWs at 1 h, 0.5 h, and 0.25 h were 31 kDa, 17 kDa, and 8 kDa, respectively, indicating that chain growth outpaces MW reduction events (ester bond breakage, intramolecular transesterification caused by tin(II) alkoxide, intermolecular transesterifications with OH groups). At the 2 h mark, the overall MW begins to reduce as tin(II) alkoxide, Sn(Oct)2's initiating form, also catalyzes the above events that reduce MW [196].

3.4.3 Results of the Polymerizations in Toluene and THF

Dependency of MW and Conversion on Reaction Conditions

The solvent explained 80 % of the variance in the MW, $Đ$, and conversion data. Reactions with toluene produced PLA with MWs from 8 kDa to 31 kDa (Figure 3.2), whereas with THF the range was 1.5 kDa to 11 kDa (Table 3.3).

Toluene is immiscible with water. On the other hand, THF is hygroscopic so the water molecules within it hydrolytically cleave the PLA chains [197], which explains the different MW between solvents. THF's hygroscopic nature overshadowed any positive microwave coupling effect that would result from its larger dielectric loss value. In other words, water-miscbile solvents that absorb moisture from the air lead to lower MW PLAs. He et al. also reported higher MWs in their conduction-heated reactions with toluene compared to THF despite their THF being anhydrous (22 kDa vs. 7.3 kDa) [198]. This also occurred in ethylene polymerizations with a terphenyl derivative complex (2-Py) catalyst precursor — 38 kDa in toluene vs. 12 kDa in dried THF [199]. Thus, the water content in our THF is not the only driving factor for the difference in MWs. Further research into how the properties of solvents affect polymerizations is warranted. The reaction in toluene peaks at 1 h after which the risk of MW reduction events increases causing chains to break [185] and lowering the MW. This also accounts for the large standard deviation in the data past 1 h (Figure 3.2) as these events, like transesterifications, occur randomly [200]. Thus, we demonstrate the effect of long reaction times on the polymerization — the variation in the data is as high as 50 % after 2 h as deploymerization and transesterification are prevalent. Three repeat experiments at 6 h, 170 °C in toluene produced MWs of 12 kDa, 27 kDa, and 38 kDa. However, the trend is one of decreasing MW. The variation in molecular weight for experiments at 1 h and less is 15 %. Other articles that synthesize PLA with microwaves maintain reaction times between 5 min to 50 min [10, 49, 50, 55, 59, 182]. Higher temperatures and toluene (Figure 3.4) as a solvent instead of THF (Figure 3.5) produced higher MW PLA. Polymerization rate increases with increasing temperature [185, 201]. The highest MW achieved was 31 kDa with a $Đ$ of 1.5 in toluene, at 170 °C, for 1 h with a conversion of 34 %. Conversions in the literature range from 2 % [49] to 95 % [56, 60]. Impurities (OH-bearing species predominantly from water) are the cause of this large variance — the more there are, the lower the conversion, and hence lower MW. OH groups induce chain scission and can also prematurely terminate growing chains by acting as an initiator and forming OH-terminated chains. Water can also hydrolyze the lactide monomers to lactic acid and reduce the pool of available lactide — an increase in lactic acid and consequently OH groups also increases the likelihood of chain scission [181]. Itzinger et al. ring-open polymerized lactide and purposefully doped the reaction medium with increasing amounts of ethanol as an impurity (0.1 % by weight, 1 % by weight, 1.5 % by weight). The MW decreased from 30 kDa at an impurity level of 0.1 % by weight to 10 kDa at 1.5 % by weight [202] representing a 50 % drop in conversion. Our experimental procedure was unable to completely eliminate the sources of impurities which is reflected in the conversion. THF innately carries more impurities (water) than toluene, which partly explains the approximate threefold decrease in conversion between the two solvents. For

these reasons, $Sn(Oct)_2$ catalyzed the polymerization as opposed to DBU despite the latter's improved performance (higher conversion rates, yields, and is active at lower temperatures). For example, Thauvin et al. studied the performance of DBU vs. $Sn(Oct)_2$ and found that there was 100 % D,L-lactide conversion in DBU at 100 °C while $Sn(Oct)_2$ was inactive at this temperature; at 170 °C the conversion was still lower (95 %) [56]. In another ROP of D,L-lactide, at 125 °C, DBU and $Sn(Oct)_2$ had similar conversions (> 90 %) but yields with DBU were higher (60 % to 83 % vs. 23 % to 35 %) [60]. However, DBU is more susceptible to impurities compared to $Sn(Oct)_2$; acidic protons deactivate DBU and induce a cascade effect until there is none left to continue the polymerization [203]. However, the MW can still be increased/decreased despite the limited conversion by modifying the M:I ratio. For example, the reaction in THF at 2 h, 170 °C and a M:I of 380 produced PLA with a MW of 5.2 kDa and a $Đ$ of 1.1 for a total conversion of 9 %. At an M:I of 1000, the MW would be 13 kDa assuming the same conversion. However, this does not continue indefinitely — in one instance, there was no significant difference in MW between M:I ratios of 1041, 2534, and 10069 and the conversion dropped from 9 % at 1041 to 2 % at 10069 [51]. Overall, we are able to control the MW of our synthesized PLA between 1 kDa and 31 kDa. This range can be modified by changing the M:I ratio.

Dispersity ($Đ$)

Dubois et al. found that $Đ$ increased with increasing temperature as a result of intermolecular transesterifications with $Al(O\text{-}i\text{-}Pr)_3$ as the catalyst. The $Đ$ went from 1.25 to 1.4 as the temperature increased from 75 °C to 85 °C with conduction heating [185]. $Đ$ was independent of temperature in our system. For example, experiments 3, 6, 12 at 6 h and 130 °C, 150 °C, and 170 °C, respectively, in THF all resulted in a $Đ$ of 1.1 (table 3.3). In addition, $Sn(Oct)_2$ is more active between 125 °C to 180 °C than $Al(O\text{-}i\text{-}Pr)_3$, with which it can take days to achieve MWs of 10^4 - 10^5 Da [187]. Toluene produced higher $Đ$ (an average of 1.5) compared to THF (an average of 1.1). A lower $Đ$ indicates more uniformity among the lengths of the polymer chains. As the polymer chains lengthen and less monomer remains for the reaction, the polymerization slows while the risk of intermolecular transesterification increases [168, 204]. This leads to increased $Đ$. Nonetheless, these are both lower than most of the other reported $Đ$'s for microwave-synthesized PLA (Table 3.1).

3.4.4 Microwaves vs. Conduction Heating

In an effort to compare a conduction-heated reaction to the microwave reactions, we replaced the usual quartz vessels with a silicon carbide vessel. Silicon carbide will absorb all the

microwaves and thus heat the reaction medium via conduction [205]. At 170 °C for 4 h in THF with silicon carbide, the D,L-lactide did not polymerize at all. On the other hand, when the reaction medium is heated via microwaves, the resulting PLA had a MW of 11 kDa and a $Đ$ of 1.2. In addition, the same reaction without a dedicated initiator still produced PLA with a MW of 10 kDa and a $Đ$ of 1.2, whereas with conduction heating it could take more than 30 h [166]. Despite the shortcomings of the experimental setup at removing impurities, it still outperforms the traditional synthesis and functions as an example of process intensification.

3.4.5 Predictor Screening of Toluene and THF

The solvent dominated the predictor screening for the entire dataset. As a result, we redid a screening for THF and toluene, separately. For THF, temperature explained 61 % of the variance for the MW, while time accounted for 39 %. In contrast, for toluene, time accounted for 93 % of the variance in MW. Temperature's influence is more pronounced in the THF data. THF's boiling point is 66 °C — at 130 °C, 150 °C, 170 °C the corresponding pressures in the reactor were 250 kPa, 500 kPa, and 800 kPa. The reactions with toluene were all at atmospheric pressure. Higher pressures favour polymerization ([206, 207]), which explains temperature accounting for 61 % of the variance in MW for THF while with toluene it is only 7 %.

3.4.6 Proton Nuclear Magnetic Resonance (^{1}H NMR)

Signals at $\delta_H = 5.10$ and $\delta_H = 1.50$ belong to methine (a) and methyl (b) groups while the signal at $\delta_H = 4.30$ represents the methine end-group [208]. The presence of many tetrads in the range of the $\delta_H = 5.04$ to $\delta_H = 5.20$ indicates no stereocontrol in our PLA [208, 209] (Figure 3.3).

3.4.7 Differential Scanning Calorimetry (DSC)

The PLA samples had an average melting temperature of 150 °C and a glass transition temperature of 55 °C, the latter being similar to other reported values while the former is 10 °C to 20 °C lower [210, 211].

3.4.8 Thermal Gravimetric Analysis (TGA)

Three samples of PLA with MWs of 10 kDa, 23 kDa, and 31 kDa underwent a TGA analysis. The 10 kDa PLA sample lost 10 % of its mass at 259 °C and 99 % of its mass at 311 °C. The 23 kDa sample lost 10 % of its mass at 255 °C and 99 % of its mass at 305 °C. The

31 kDa sample lost 10 % of its mass by 269 °C (including the residual toluene that begins to evaporate at 105 °C) and 99 % of its mass at 318 °C. There is a minor dependence on degradation temperature and MW. The degradation temperature of our PLA is consistent with some of the literature [198, 211] and a little lower than others (269 °C vs. 290 °C) [212].

3.4.9 Statistical Model

We fit the data from our experimental design to a non-linear model that describes the growth and decay phases of the polymerization. The model contains three fitted parameters with two independent variables, reaction time (from 0.25 h to 6 h) and temperature (from 130 °C to 170 °C) (Equation 3.3). The latter corresponds to an exponential Arrhenius expression. The model's (Equation 3.3) R^2 for toluene and THF are 91 % (Figure 3.4) and 94 % (Figure 3.5), respectively.

$$\mathrm{MW} = \beta_0 * [-e^{-\beta_1 t} + e^{-\beta_2 t^2}] * e^{\frac{-Ea}{R}[\frac{1}{T+273} - \frac{1}{T_{ref}+273}]} \tag{3.3}$$

T_{ref} is the average temperature (150 °C), R is the universal gas constant in J mol^{-1} K^{-1}, and t is in h. The pseudo activation energies for toluene and THF are 12 kJ and 39 kJ.

The predicted MW begins to decrease as t approaches 4 h for toluene and as t approaches 6 h for THF as a result of depolymerization and transesterification reactions (represented by β_2), which are exacerbated at longer reaction times (Figure 3.4, Figure 3.5). The onset of MW reduction events is quicker in toluene ($\beta_2 = 0.009$) compared to THF ($\beta_2 = 0.007$) because it peaks sooner (31 kDa at 1 h versus 11 kDa at 4 h). Prior to this, the chains are growing exponentially, which is represented by β_1 term (1.45 for toluene, 0.34 for THF). The β_0 often represents the maximum achievable MW for a given system. The standard deviation between the experimental data and model predictions is 4 kDa in toluene (Figure 3.4). At longer reaction times (> 2 h) the MW reduction events become more prominent thereby decreasing the MW of the polymer chains. This process, however, is random [200] and thus so is the degree to which the MW decreases. As a result, the MW at longer reaction times varies more than those at shorter times. The data point at 6 h and 130 °C (Figure 3.4) is an example of this as it is 30 % above the predicted MW. On the other hand, the standard deviation of 3 repeats for the experiments in THF was 7 % (0.7 kDa). The deviation between the model and experimental data was 1.1 kDa, which is reasonable considering the reproducibility was 0.7 kDa (Figure 3.5). The model explains 94 % of the variance in the experimental data for THF and captures the increasing MW with time as well as the plateau. However, during the initial reaction period, the PLA MW of one experimental test (0.5 h, 150 °C), increased

much faster than expected.

Model Applied to Literature Data

We evaluated the efficacy of our statistical model by fitting it to three other datasets, at similar reaction conditions (microwave reactor, $Sn(Oct)_2$ as the catalyst), in the literature. The experiments from the first dataset were at a constant temperature (150 °C) but varying M:I ratios (1041, 2534); their MWs ranged from 15 kDa to 46 kDa [51]. Thus, the pseudo Arrhenius term equals 1, which leaves the power aspect of the model. For the data at an M:I of 1041, the model explained 71 % of the variance, with a β_0 of 24500, a β_1 of 14, and a β_2 of 0.35. However, the R^2 drops to 0.4 for the data at an M:I of 2534 with a β_0, β_1, and β_2 of 46000, 7.4, and 3.6, respectively. Moreover, by combing both datasets into one and incorporating a new term (β_3) to the model (Equation 3.4) to account for the change in M:I, the R^2, β_0, β_1, β_2, β_3 become 0.59, 59000, 14, 1, and -0.12, respectively. This low β_3 indicates that M:I had little effect on the final MW in their data [51].

$$MW = \beta_0 * [-e^{-\beta_1 t} + e^{-\beta_2 t^2}] * MI^{\beta_3} \tag{3.4}$$

The second dataset had a constant temperature of 180 °C [49]. We focused on the data at a constant M:I (1041) and power (360 W) with reaction times from 5 min to 20 min. The final data point (at 20 min) had no MW value as it significantly degraded. To increase the total number of data points, we assigned a MW to the 30 min sample equal to 10 % of the max MW in the dataset. The MWs ranged from 7 kDa to 10 kDa. The resulting R^2, β_0, β_1, and β_2 were 0.64, 9500, 29, and 8.8, respectively. The R^2 only varies between 0.68 and 0.61 if the assumption for the MW of the degraded sample is 20 % or 2 % of the max MW from the dataset.

The final dataset had a constant temperature of 100 °C. However, there were only 3 data points, and the model has 3 parameters so the resulting R^2 is 0.99, with a β_1 of 0.1. The latter is of interest as it represents the chain growth aspect of the polymerization, a lower value represents higher growth. At 10 min, 18 min, and 30 min the respective MWs were 80 kDa, 176 kDa, and 300 kDa [59] — the model predicts that the chains are growing linearly and not exponentially as evidenced by the low β_1. The M:I ratio is not specified in the article so the theoretical max is unknown.

3.5 Conclusion

We polymerized D,L-lactide in a microwave reactor in the presence of $Sn(Oct)_2$, BnOH and toluene or THF. The solvent had the biggest influence on the final MW of PLA. The molecular weights in toluene were 2-3x higher compared to THF at the same conditions. The presence of water in THF overshadowed any positive microwave-coupling effects of its higher dielectric loss; eliminating traces of water in all of the reagents would lead to larger molecular weights. However, this is not the only influential factor because even in conduction heating with toluene and anhydrous THF, the MWs produced with the former were 3x higher than those produced with the latter [198, 199]. After 1 h at 170 °C in toluene, the MW was 31 kDa. In THF, after 4 h at 170 °C, the MW only reached 11 kDa. In addition, we were able to eliminate numerous solvents as unfit for the ROP of D,L-lactide. Some, as with THF, are hygroscopic and will hinder the polymerizations, while others are unsafe at our reaction temperatures (130 °C to 170 °C). We also developed a statistical model that predicts the MW as a function of temperature, time, and the estimated max achieveable MW for a given system. Future work should involve a continuous experimental setup coupled with microwaves for the synthesis of PLA on a larger scale; if done in batch with large quantities, penetration depth becomes a considerable issue. Strategies for scale-up are already present in the literature [213] and are present in the agri-food industry, cosmetics, and vulcanisation of rubber [214]. However, due to D,L-lactide's low dielectric loss (0.04) we recommend the addition of polar species to improve energy transfer. Overall, microwaves are a great technology for PLA synthesis, however, proper removal of impurities is paramount; microwave reactor designs that allow for reagent purging would facilitate and improve the polymerization immensely, with the potential to push D,L-lactide conversion into the 80 % to 100 % range.

3.6 Conflicts of interest

There are no conflicts of interest to declare.

3.7 Acknowledgements

We acknowledge the support of the Natural Sciences and Engineering Research Council of Canada (NSERC), [funding reference number 466475120]. This work was supported again by NSERC via the stipend allocated to Nicolas Patience through the NSERC-CREATE PrEEmiuM program.

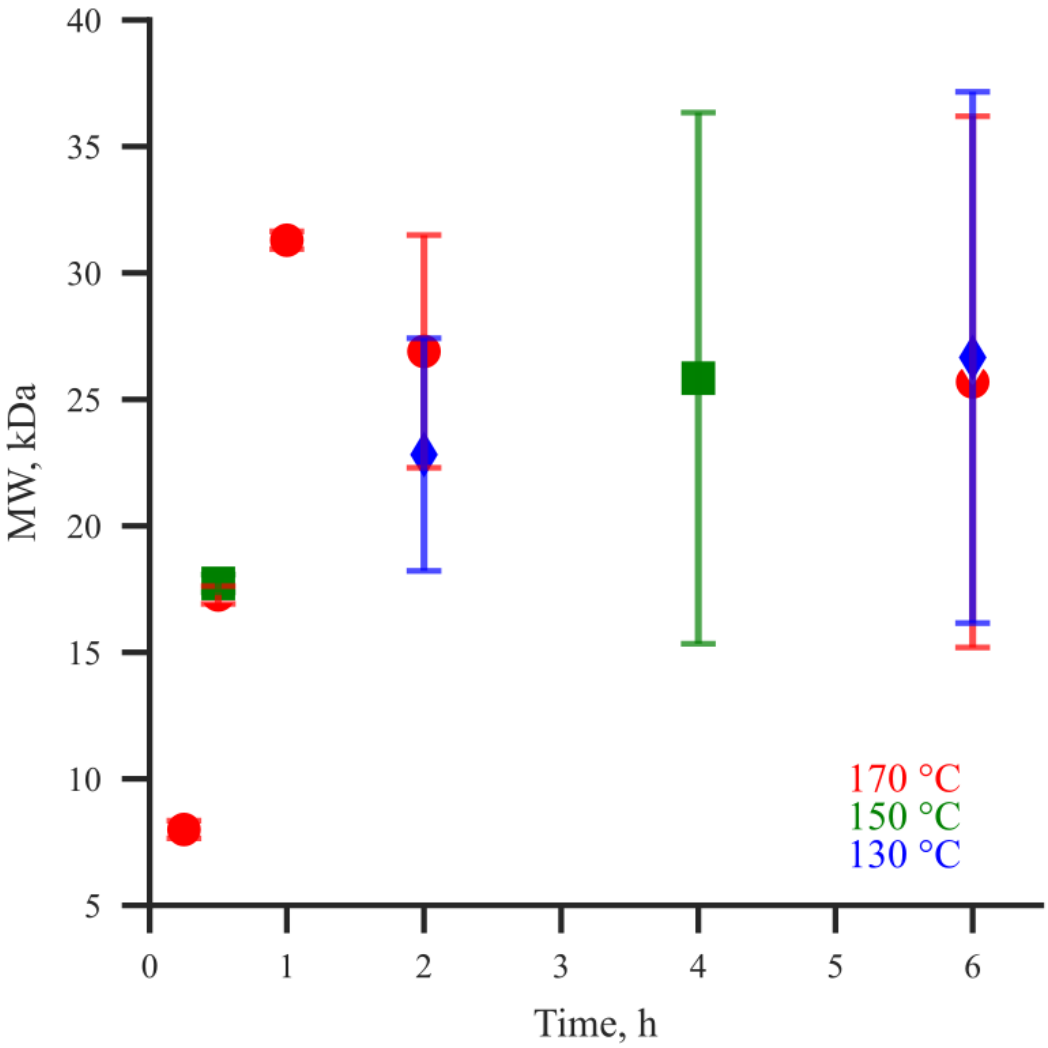

Figure (3.2) MW as a function of time and temperatures in toluene. Error bars represent the standard deviation. For the data between 0 h to 1 h the error bars are the size of the markers. The large standard deviations past 1 h is caused by the stochastic nature of the MW reduction events. Please refer to the main text for a more detailed explanation.

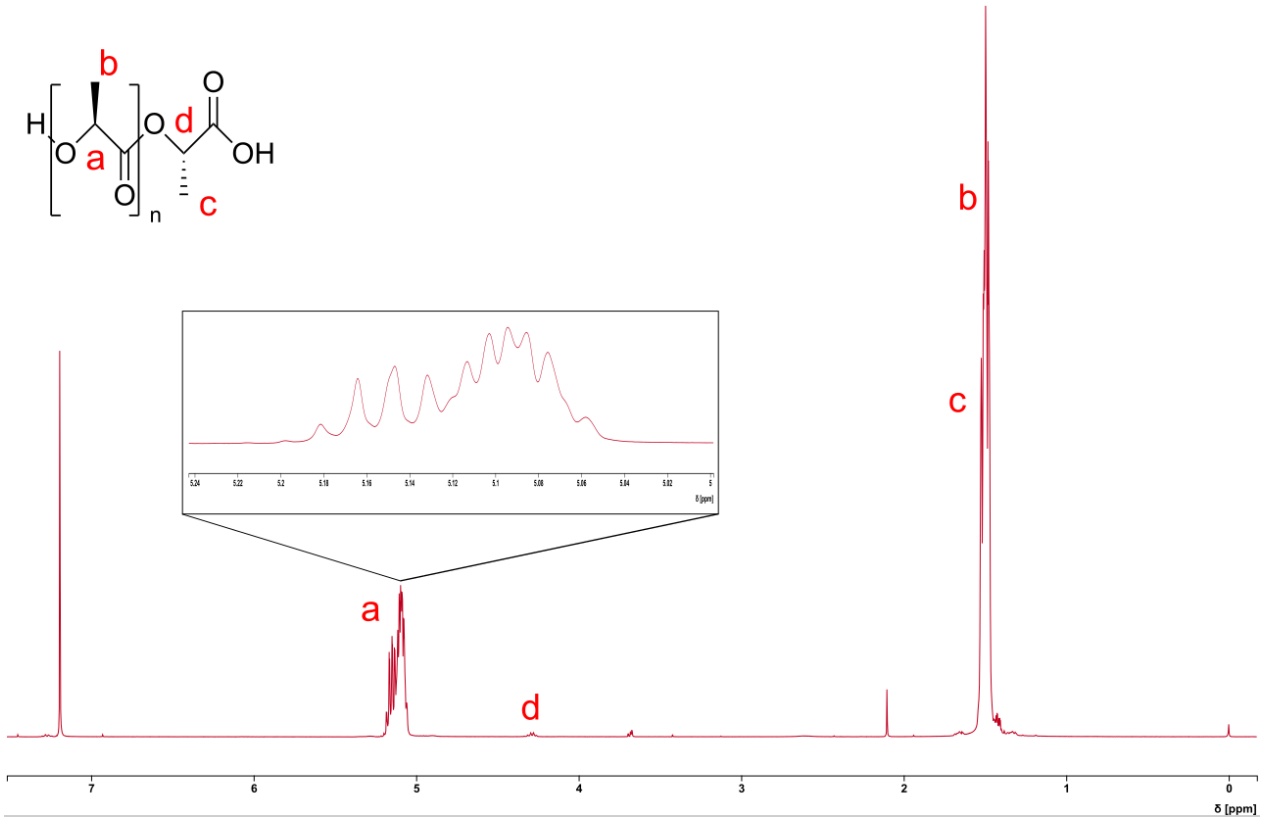

Figure (3.3) ^{1}H NMR spectra of poly(D,L-lactide).

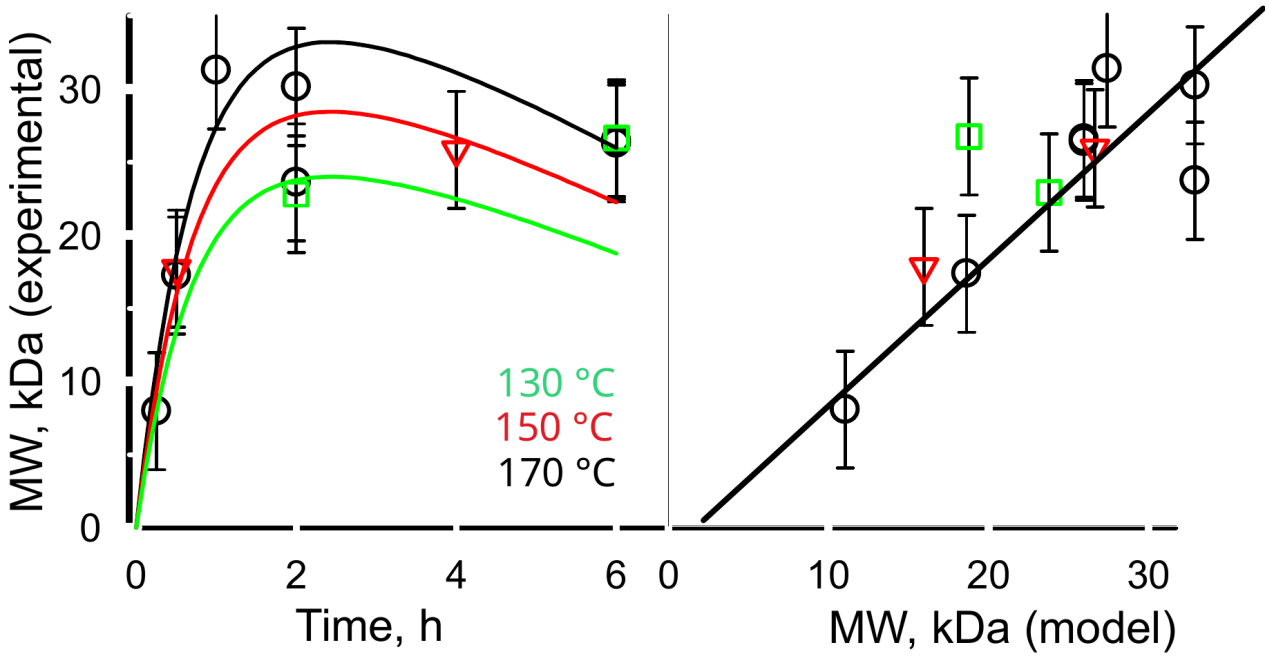

Figure (3.4) PLA MW as a function of time in toluene (left) and a standard parity plot (right). The lines represent the non-linear regression model (eq3) and the symbols the experimental data. $R^2 = 0.91$.

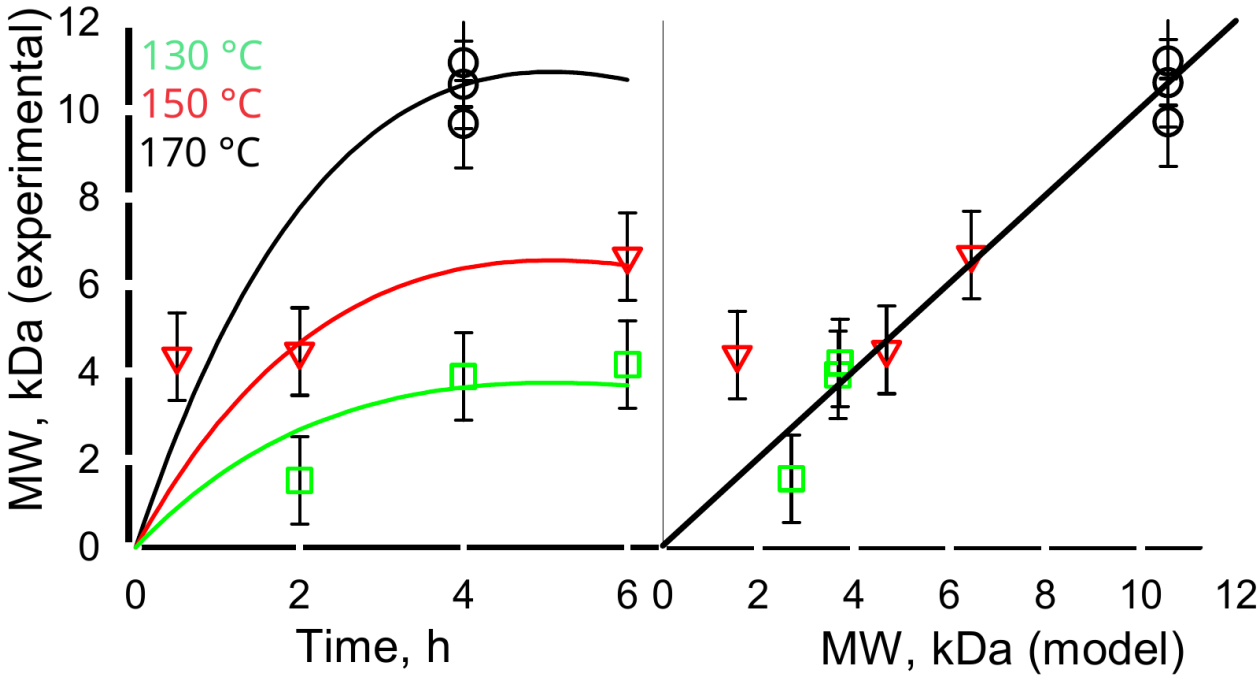

Figure (3.5) PLA MW as a function of time in THF (left) and a standard parity plot (right). The lines represent the non-linear regression model (eq3) and the symbols the experimental data. $R^2 = 0.94$.

CHAPTER 4 CONTINUOUS NANOPRECIPITATION OF POLY(D,L-LACTIDE) IN A ROTOR-STATOR SPINNING DISK REACTOR

In the previous chapter, we produced PLA with microwaves. However, the difficulties associated with removing impurities from the polymer lead us to a different synthesis mechanism outlined in Section 4.2.2. This also provided us with a solid PLA, facilitating dissolution in the organic phase prior to nanoprecipitation.

4.1 Introduction

Drug shortage is a global issue. In 2020, the United States alone was in short supply on 129 different medications with antimicrobials and oncological drugs topping the list [4]. Drugs require frequent administration and doses exceeding the body's absorption capacity to treat ailments. The former is attributed to the body's immune system that will degrade and eliminate drugs. The latter stems from the drug distribution within the body — little of it reaches the desired areas. This leads to drug concentration spikes in the body, which cause adverse side-effects and affects QoL [9]. In fact, these side-effects are estimated to account for 3 % of deaths in the general population [215]. Sustained and targeted drug delivery systems are a promising avenue to address these shortcomings — they maintain drug levels at the desired therapeutic level and aim at concentrating it in the necessary areas [9, 216]. These systems are often polymer-based, the most common being polyglycolic acid, PLA, polycaprolactone, and polydioxanone [217].

PLA is an aliphatic polyester derived from α-hydroxy acids. It is a biocompatible and biodegradable polymer that degrades by hydrolysis of its ester bonds [12]. The body metabolizes and excretes the degradation products without any physiological stress [13]. The FDA approved PLA in the 1970s and since, industries as well as researchers have studied it for suturing [15], scaffolds [163], and drug delivery [164]. Drug delivery applications usually requires MWs less than 50 kDa [14]. PLA alone is brittle ($<$ 10 % elongation at break), hydrophobic (which translates to low cell affinity and increased inflammatory responses), and lacks reactive side chains [13]. The latter being the main reason lactide is polymerized with other monomers, like glycolic acid, to create suitable drug carrier systems. PLGA is a staple carrier system [96]. Additionally, NPs of PEG chains grafted onto PLA function as stealth drug nanocarriers that resist protein adsorption and aggregation [218] — two important metrics to determine the viability of a nanocarrier. PLGA and PEG are also often combined for targeted drug delivery [219]. Research into PLA and its derivatives is one facet

of nanomedicine, a rapidly growing field of science focused on nano-sized materials that offer a plethora of applications among them tissue penetration [220], targeted drug delivery [221], and sustained drug release [222]. Since 1970, there have been over 600 new drug applications that contain nanomaterials with half of these occurring in the last 10 years [223].

4.1.1 Nanoprecipitation Mechanism

Nanoprecipitation is one of the most common techniques to synthesize nano-sized polymeric drug delivery systems. The process includes supersaturation, nucleation, and growth. *Supersaturation*: As the polymeric solution comes into contact with the anti-solvent it achieves a state of supersaturation. The particle size will increase as the concentration of the polymeric solution increases despite high levels of supersaturation promoting rapid nucleation [224] and smaller particles — with a higher concentration there is more opportunity for nuclei to grow by associating with other molecules. *Nucleation*: follows supersaturation once the energy barrier required to form nuclei is overcome and the system begins to thermodynamically stabilize. These nuclei start to grow by associating with other solute molecules until they are stable against dissolution [86]. Nucleation ends once the level of solute dips below the critical supersaturation concentration. Further growth is fuelled by aggregation. *Aggregation*: Van Der Waals interactions between NPs cause them to aggregate [225]. The frequency of collision (influenced by particle concentration, size, and motion of the system) between particles determines the degree of aggregation — stabilizers can limit the extent of aggregation [86].

The solvent chosen for dissolution of the polymer influences the mean particle size. Solvents with lower viscosities and higher diffusion coefficients in water will produce smaller particles. They promote faster mixing which leads to a higher degree of supersaturation [226]. In addition, as the solvent/water miscibility of the system increases, the particle size will decrease. For example, at a solvent:water ratio of 1:10, the particle size decreased from 150 nm in acetonitrile to 115 nm in acetone, and down to 90 nm in DMF [219].

Nanoprecipitation in microfluidic technologies is common in the literature for the continuous production of these nano-sized delivery systems. However, one of the main challenges is low production rates; microfluidic devices often produce on the µg to mg scale [227]. Feasible production rates for clinical studies and industry are $100\,\mathrm{g\,d^{-1}}$ and $1\,\mathrm{kg\,d^{-1}}$ [11]. Rs-SDRs have the potential to greatly exceed these production rates.

4.1.2 Rotor-Stator Spinning Disk Reactor (rs-SDR)

The following is a small recap from the literature review as it relates to this chapter.

Rs-SDRs fall under a class of PI technologies [33] with excellent heat and mass transfer capabilities well-suited for mulitphase chemistry (liquid-gas, liquid-liquid, gas-liquid-liquid). Liquid-liquid mass transfer rates in an rs-SDR are 25x higher than in packed columns and 15x higher than in microchannels [125]. Traditionally, they consist of one or more rotating disks confined in a narrow casing producing large shear and centrifugal forces and creating an environment conducive to intense mixing. The energy generated from the rotating disks is transferred into the reaction medium generating high energy dissipation rates, ϵ, that can reach $1 \times 10^5\,\mathrm{W\,kg^{-1}}$ [123]. These high rates translate into high levels of mass transfer [124, 228, 229], heat transfer [126, 230, 231], and low micromixing times [123, 129, 134, 232]. Residence times in a rs-SDR are solely based on the flowrate and reactor volume (Equation 2.4) as opposed to its counterpart, the tf-SDR, whose residence time is also determined by the rotational speed and viscosity (Equation 2.3) [121].

The search strategy ("rotor-stator" OR "rotor-stator system" OR "rotor-stator device") AND ("spinning disk reactor" OR "spinning disc reactor") generated 50 results (46 articles, 3 proceeding papers, and 1 letter) in the WoS Core Collection with articles dating back to 2010. The majority of articles are fundamental studies on heat and mass transfer [124, 125, 126, 230], residence time distribution [127, 128], micromixing [129, 134, 232, 233], and scale-up [234]. Experimental studies include photochemical oxidation and degradation [135, 235], epoxidation of methyl oleate [136], extraction of chromium (III) from aqueous solutions [236], tertiary amine N-oxdiation [237], production of sodium-ion cathodes [238], sulfite reduction of alkyl hydroperoxides [239], transesterification of trigylcerides [137], esterification of free fatty acids [240], and synthesis of $BaTiO_3$ NPs [138]. The overarching theme across rs-SDR studies is PI.

4.1.3 Novelty

There are only a few existing techniques that can satisfy clinical and/or industry scale production (Table 4.1). We propose the rs-SDR as a robust alternative. For the first time, we synthesize PLA NPs in an rs-SDR at rates of $> 100\,\mathrm{g\,d^{-1}}$, exceeding the requirements for large-scale clinical trials with the potential to surpass industrial-scale requirements, as well. The quality (size and $Đ$) of the NPs are suitable for drug delivery applications, and the batch-to-batch reproducibility is small (standard deviation for size and $Đ$ are 6 nm and 0.02, respectively). We also demonstrate the reactor's ability to load PLA and PLA-PEG NPs with ibuprofen.

Table (4.1) Different NP synthesis techniques with a focus on continuous large-scale production. (a) = pulsed, (b) = continuous experiments, * = theoretical calculation. The abbreviations are: GC = glass capillary, PDMS = polydimethylsiloxane, COP = cyclic olefin polymer, PID = polyimide, CTJM = coaxial turbulent jet mixer, HPH = high pressure homogenization, FFR = fiber fluidic reactor, Wa = water, Ac = acetone, Acn = acetonitrile, DCM = dichloromethane, DMSO = dimethyl sulfoxide, EA = ethyl acetate, PR = max production rate.

Technique	Polymer	Size, nm	Weighting	$Đ$	Solvents	PR ($g\,d^{-1}$)	Ref.
GC microfluidic	PLA / PCL	300 to 600	Z_{avg}	0.18 to 0.30	THF-Wa	0.04	[89]
GC microfluidic	PLGA	100 to 330	Intensity	0.05 to 0.15	Acn-Wa	240	[241]
PDMS micorfluidic	PLGA-Lipid	35 to 180	Volume	-	Acn-Wa	0.36	[242]
PDMS microfluidic	PLGA-PEG	24 to 34	Z_{avg}	-	Acn-Wa	0.1	[90]
PDMS microfluidic	PLGA-PEG	13 to 150	Volume	-	Acn-Wa	2	[109]
COP microfluidic	PLGA	63 to 260	-	0.08 to 0.42	Acn-Wa	324	[98]
PID microfluidic	PEG-PLGA	50 to 85	Volume	-	Acn-Wa	300	[99]
CTJM	PLGA-PEG	25 to 100	Volume	-	Acn-Wa	3000	[11]
HPH	PLGA	200 to 300	-	-	DCM-Wa	-	[96]
FFR	PLGA	90 to 180	-	0.05 to 0.15	Ac-Wa	53	[97]
Sonication	PLGA	100 to 200	Z_{avg}	0.07 to 0.12	DCM-DMSO-Wa	2000	[91]
Membrane	PLGA-PEG	250 to 400	Z_{avg}	0.13 to 0.18	Ac-Wa	4	[93]
Micromixer	PLGA	200 to 700	-	-	Ea-Wa	240	[104]
Lab-scale rs-SDR[a]	PLA	58 to 129	Z_{avg}	0.12 to 0.22	Ac-Wa	576	-
Lab-scale rs-SDR[b]	PLA	70 to 137	Z_{avg}	0.09 to 0.17	Ac-Wa	576	-
Lab-scale rs-SDR[b]	PLA-PEG	63 to 132	Z_{avg}	0.11 to 0.14	Ac-Wa	576	-
Pilot-scale rs-SDR	-	-	-	-	-	54000*	-

4.2 Experimental

4.2.1 Materials

BnOH (99.8 %, Sigma-Aldrich), the initiator for the polymerization, was filtered through a basic alumina column prior to use. D,L-lactide (99 %, Sigma-Aldrich) was recrystallized with methanol and then toluene and vacuum dried overnight prior to use. DBU (Sigma-Aldrich, 99 %) was dried over calcium hydride and vacuum distilled at 150 °C. It was then kept over 3 Å molecular sieves overnight prior to use. THF (99.6 % stabilized with BHT) was purchased from Fisher Scientific and purified with glass-vacuum filtration before use in the GPC instrument. Benzoic acid (99.5 %), methanol (99.8 %), toluene (99.8 %), DCM (99.8 %, with 40-150 ppm of amylene as a stabilizer), acetone (99.5 %) (all from Sigma-Aldrich except methanol that was from Fisher Scientific), and distilled water were used without treatment or further purification. We performed the nanoprecipitation reactions in a rs-SDR from FlowID (SpinPro R2) made from silicon carbide, with a volume of 19 mL, a max rotational speed of 6000 RPM, and able to withstand temperatures and pressures up to 140 °C and 1000 kPa. Acetone was our solvent of choice as it can yield particle sizes in our desired range (50 nm to

150 nm) and is considered by Pfizer to be the greenest solvent, excluding water [243]. The continuous experiments consumed approximately 0.5 L of acetone per run.

4.2.2 PLA, PLA-PEG Synthesis

A 50 mL round-bottom flask was flame-dried under reduced pressure with a propane torch and then filled with argon. This process was repeated three times. Afterwards, we transferred 21.7 µL (0.21 mmol dm^{-3}) of the initiator, BnOH, into the flask. In a separate vial, 4.5 g (31.5 mmol dm^{-3}) of D,L-lactide was combined with 10 mL of dry DCM, under argon, and subsequently added to the round-bottom flask. DBU (31.4 µL) was then injected to initiate the polymerization — the reaction occurred at room temperature and lasted 1 h. Benzoic acid (65 mg) quenched the polymerization. Finally, the solution was diluted with DCM and the polymer was obtained by precipitation into cold methanol and water (3:1 volume ratio). The same procedure was used for PLA-PEG except that the initiator was PEG(2k)-OH instead of BnOH.

4.2.3 Characterization

Proton Nuclear Magnetic Resonance (^{1}H NMR)

A Bruker AV-III 400 MHz spectrometer identified the PLA samples dissolved in $CDCl_3$ and we analyzed the data with the help of the NMRium software. ^{1}H NMR confirmed the structure and degree of polymerization of the PLA and PLA-PEG polymers.

Gel Permeation Chromatography (GPC)

The GPC measurements were performed with a Wyatt instrument equipped with two TSKgel GMHHR-L columns and one guard column, along with differential refractometer (RI) and light scattering (LS) detectors. The measurements were carried out in THF as the eluent, at a flowrate of 0.6 mL/min. Polystyrene (PS) standards with molecular-average numbers ranging from Mn = 2,000 Da to Mn = 1,800,000 Da were used. The MWs of the synthesized PLA and PLA-PEGs (PEG2k) were between 8 kDa and 54 kDa. The PEG content (% w/w) in the PLA-PEGs was 8 %.

Dynamic Light Scattering (DLS)

A Zetasizer Nano ZS from Malvern Instruments determined the particle size and $Đ$ of the PLA NPs. The NPs suspended in water were pipetted into a 2.5 mL BRAND polystyrene macro-

cuvette and then analyzed at 21 °C with an equilibration time of 120 s and a backscatter angle of 173°. The refractive index of PLA was set to 1.459 and each sample was analyzed 3 times. The reported particle sizes in the manuscript refer to the Z_{avg} and not the intensity-based particle size.

Transmission Electron Microscopy (TEM)

A Cold Field Emission Gun Transmission Electron Microscope (CFEG-TEM) from JEOL (model JEM-F200) operating at 200 kV photographed bright field images of the PLA. Short acquisition times (< 1 min) were necessary to avoid damaging the particles. We diluted the samples by a factor of 10 in distilled water and left them to dry on copper TEM grids covered with lacey carbon film before analysis.

Viscosity Measurements

A Rheometer HAAKE Viscotester iQ Air from Thermo Scientific configured with a CC27 coaxial cylinder measured the viscosity of the water-acetone combinations. An external water circulator stabilized the temperature at 25 °C, the same value as during the nanoprecipitations. We introduced 3 mL of sample and increased the shear rate (stepwise) from $50\,\text{s}^{-1}$ to $1500\,\text{s}^{-1}$.

4.2.4 Pulse Experiments in the rs-SDR

The pulse experiments involved injecting 5 mL of a PLA-acetone solution before switching back to a pure acetone feed. We opted for a full factorial design for the pulse experiments (Table 4.2). The 3 factors were the rotational speed (1500 RPM, 3250 RPM, 5000 RPM), the concentration of PLA in acetone ($10\,\text{mg}\,\text{mL}^{-1}$, $20\,\text{mg}\,\text{mL}^{-1}$, $30\,\text{mg}\,\text{mL}^{-1}$), and the flowrate ratio (10:25, 10:50, 10:100). The flowrate ratio is the ratio between the flowrate of PLA in acetone and water. The former is constant at $10\,\text{mL}\,\text{min}^{-1}$. We fed pure acetone and distilled water into the rs-SDR via 2 inputs and ramped up the rotational speed to the desired level. Afterwards, we moved the tube from the pure acetone to the PLA/acetone solution (5 mL) and once depleted, back to the pure acetone. We sampled every 10 s for 5 s and subsequently measured the particle size with DLS.

4.2.5 Continuous Experiments in the rs-SDR

For the continuous experiments, we opted for a 2-factor 3-level full factorial design with a third factor (RPM) at two-levels (1500 RPM, 3000 RPM) for a total of 18 runs, excluding

Table (4.2) DoE for pulsed experiments. * removed from analysis as an outlier. A:W R represents the acetone:water ratio.

Exp. ID	RPM	C	A:W R	Size (nm)	$Đ$
ST23	1500	10	10:25	77	0.15
ST25	1500	10	10:55	78	0.12
ST22	1500	10	10:110	76	0.12
ST12	1500	20	10:25	110	0.16
ST1	1500	20	10:55	125	0.15
ST8	1500	20	10:110	103	0.14
ST19	1500	30	10:25	129	0.14
ST4	1500	30	10:55	109	0.15
ST6	1500	30	10:110	124	0.14
ST26*	3250	10	10:25	102	0.16
ST20	3250	10	10:55	78	0.14
ST10	3250	10	10:110	65	0.15
ST27	3250	20	10:25	85	0.12
ST17	3250	20	10:55	78	0.14
ST5	3250	20	10:110	88	0.15
ST21	3250	30	10:25	87	0.15
ST14	3250	30	10:55	90	0.14
ST11	3250	30	10:110	89	0.16
ST3	5000	10	10:25	56	0.16
ST18	5000	10	10:55	59	0.15
ST16	5000	10	10:110	62	0.2
ST15	5000	20	10:25	81	0.16
ST24	5000	20	10:50	68	0.15
ST9	5000	20	10:110	62	0.15
ST13	5000	30	10:25	98	0.13
ST2	5000	30	10:55	58	0.14
ST7	5000	30	10:110	70	0.22

repeats (Table 4.3). The factors were the concentration of PLA in acetone ($5\,\mathrm{mg\,mL^{-1}}$, $10\,\mathrm{mg\,mL^{-1}}$, $15\,\mathrm{mg\,mL^{-1}}$) and the flowrate ratio (5:55, 10:50, 15:45, in $\mathrm{mL\,min^{-1}}$). The total flowrate was kept constant at $60\,\mathrm{mL\,min^{-1}}$. We fed pure acetone and distilled water into the rs-SDR via 2 inputs and increased the rotational speed to the desired level. Afterwards, we swapped the pure acetone feed for the PLA/acetone solution. Particles were measured via DLS directly after the reaction. Experiment 18 (A10) could not be completed, the high concentration of PLA associated with a larger acetone:water ratio (1/3) clogged the reactor channels. After we completed the DoE (design of experiments), we added 3 more runs at 2250 RPM and varying concentrations, as well as experiments with PLA-PEG (Table 4.3).

Table (4.3) DoE for continuous experiments. * removed from analysis as an outlier. Experiments PP1-PP3 were with PLA-PEG. A:W R represents the acetone:water ratio.

Exp. ID	RPM	C $\mathrm{mg\,mL^{-1}}$	A:W R	Size nm	$Đ$
C1	1500	5	1/11	80	0.11
C3	1500	5	1/5	79	0.11
C5	1500	10	1/11	94	0.10
C7	1500	10	1/5	88	0.17
A1	1500	5	1/3	74	0.12
A2	1500	10	1/3	97	0.11
A5	1500	15	1/11	121	0.11
A7	1500	15	1/5	106	0.13
A9*	1500	15	1/3	98	0.13
B1	2250	5	1/11	80	0.16
B2	2250	10	1/11	95	0.19
B3	2250	15	1/11	106	0.16
C9	3000	5	1/11	66	0.14
C11	3000	5	1/5	62	0.16
C13	3000	10	1/11	93	0.10
C15	3000	10	1/5	73	0.16
A3	3000	5	1/3	58	0.16
A4	3000	10	1/3	65	0.11
A6	3000	15	1/11	86	0.14
A8	3000	15	1/5	74	0.13
A10	3000	15	1/3	-	-
PP1	1500	5	1/11	63	0.11
PP2	1500	10	1/11	96	0.13
PP3	1500	15	1/11	132	0.14

4.2.6 Drug Loading Experiments in the rs-SDR

For the drug loading experiments, we fed pure acetone plus distilled water and set the rotational speed to 1500 RPM before switching the acetone feed to a PLA-drug-acetone solution (5 mg mL^{-1} of PLA and ibuprofen between 0.25 mg mL^{-1} to 1 mg mL^{-1} representing 5 % to 20 % of the polymer's mass). Samples were collected between the 4 min and 6 min mark and put under vacuum for 2.5 h to evaporate the acetone. Afterward, they were ultracentrifuged at 20000 RPM (47800 rcf) at 4 °C (Sorvall RC6, rotor SS-34, Thermo Fisher Scientific, Canada) for 2 h to ensure total sedimentation of the NPs [244]. In total, 3 h elapsed between the nanoprecipitation/encapsulation and the centrifugation. A few mL of the supernatant was then frozen at −80 °C until analysis with HPLC. The same procedure was followed for the PLA-PEG experiments with ibuprofen and acetaminophen.

Determination of Drug Loading and Encapsulation Efficiency with High Performance Liquid Chromatography (HPLC)

Direct quantification (wavelength analysis of NP-loaded drug pellets with a UV-visible spectrophotometer) of encapsulated drug in the NPs produces similar results to indirect quantification (HPLC analysis of the supernatant to determine the non-encapsulated fraction of drug) [244]. We indirectly quantified the amount of drug encapsulated with HPLC. The supernatant was injected into a Thermo Scientific UltiMate 3000 HPLC with a C18 columen at 0.5 mL min^{-1} with an injection volume of 20 µL in a mobile phase of acetonitrile-water-glacial acetic acid (75:24.9:0.1, v/v), with a column temperature of 40 °C. The UV-Vis detector was set to 222 nm and 243 nm for ibuprofen and acetaminophen, respectively. The calibration curve for acetaminophen was linear between 20 ppm and 200 ppm ($R^2 = 0.9997$). For ibuprofen, the calibration curve was linear between 1 ppm and 150 ppm ($R^2 = 0.9998$). Drug loading (DL) and encapsulation efficiency (EE) were calculated as follows:

DL, % = [(total drug mass - mass drug in supernatant) / total NP mass] * 100

EE, % = [(mass drug in NP) * 100] / total drug mass

4.2.7 Theory — Micromixing in an rs-SDR

Micromixing

We base the micromixing time in an rs-SDR on the engulfment model, in which engulfment of one fluid by another via vorticity is the rate-determining step in micromixing [245]. The engulfment rate in s^{-1}, E (Equation 4.1), is characterized by growing eddies in the viscous-

convective range, a range where eddies' motion are influenced by viscosity but convective mixing is still effective [245].

$$E = 0.05776 \left(\frac{\epsilon}{\nu}\right)^{\frac{1}{2}} \tag{4.1}$$

If we assume that this process dominates mixing at the smallest scale, the micromixing time can be calculated as (Equation 4.2):

$$\tau_{mix} = \frac{1}{E} \tag{4.2}$$

If we further assume that turbulence in an rs-SDR is homogeneous and isotropic then the micromixing time is linearly proportional to the Kolmogorov time scale, τ_{K} (Equation 4.3), which indicates the time for the smallest turbulent eddies to dissipate their energy as a result of viscosity effects [246]. τ_{K} is important for understanding the transition from small-scale motions dominated by viscosity to large-scale motions dominated by inertia [134], i.e., the viscous-convection range. ϵ is the local dissipation rate. ν is the kinematic viscosity, determined experimentally.

$$\tau_{\mathrm{K}} = \left(\frac{\nu}{\epsilon}\right)^{\frac{1}{2}} \tag{4.3}$$

Overall, we can approximate the micromixing time in an rs-SDR to that of a Rushton stirrer (Equation 4.4) [134, 247].

$$\tau_{\mathrm{mix}} = \tau_E = 17.3\tau_{\mathrm{K}} \tag{4.4}$$

Energy dissipation rate

There are four flow regimes (I to IV) that can be characterized in an rs-SDR that are determined by the rotational Reynolds number and the G ratio. Regime I concerns close clearance laminar flow, regime II separate boundary layers with laminar flow, regime III close clearance turbulent flow, and regime IV concerns separate boundary layers with turbulent flow [143]. We operate in regime III. The torque exerted by the spinning disk is related to the energy dissipation rate on the Kolmogorov scale [134]. Moreover, pressure drop contributes negligibly to the total energy dissipation rate versus the spinning of the disk such that it is approximately equal to the product of the rotational speed and the total torque exerted by the disk on the liquid (Equation 4.5) [248].

$$E_{\mathrm{dr}} \approx \omega \times M_{\mathrm{t}} \tag{4.5}$$

The total torque is calculated from the torque coefficient C_{m}, an empirical expression (Equation 4.6) developed to calculate the torque exerted by a disk operating in regime III flow.

$$C_{\mathrm{m(III)}} = \frac{0.08}{G^{1/6} \times \mathrm{Re}^{1/4}} \tag{4.6}$$

With C_{m}, the expression for the total torque of our system of 3 disks is (Equation 4.7)

$$M_{\mathrm{t}} = \frac{3}{2} \times C_{\mathrm{m}} \times \rho \times \omega^2 \times r_{\mathrm{D}}^5 \tag{4.7}$$

Where ρ is the density of the liquid. Afterwards, the total energy dissipation rate (E_{dr}) is related to the local energy dissipation (ϵ_{loc}) rate via a proportionality constant, α, and $r_{\mathrm{D}}^{15/4}$ (Equation. 4.8, 4.9) [248].

$$E_{\mathrm{dr}} = 2\alpha \int_{r_{\mathrm{axis}}}^{r_{\mathrm{D}}} r_{\mathrm{D}}^{15/4}\, dr \tag{4.8}$$

$$\epsilon_{\mathrm{loc}} = \frac{\alpha \int_{r_{local-0.5\Delta r}}^{r_{local+0.5\Delta r}} r_{\mathrm{D}}^{15/4}\, dr}{\pi s[(r_{local} + 0.5\Delta r)^2 - (r_{local} - 0.5\Delta r)^2]} \tag{4.9}$$

Where r_{local} is the radius of the region with a thickness of Δr where the reagents combine. Once the ϵ_{loc} is determined, we can calculate the mixing time in the rs-SDR (Equation 4.4).

4.3 Results and Discussion

4.3.1 Effect of Molecular Weight on Particle Size

The MW of the PLA did not affect the final particle size of the NPs. We repeated the same experiment (C1) with 4 different MWs, 8 kDa, 27 kDa, 44 kDa, and 54 kDa. The resulting sizes were 83 nm, 87 nm, and 77 nm, respectively (Table 4.4). Despite multiple reports stating that increasing the MW increases particle size [249, 250], the NPs synthesized with our shortest PLA (8 kDa) were larger than those synthesized with our longest PLA (54 kDa) — 83 nm vs. 77 nm. Legrand et al. reported PLA NP sizes of 80 nm, 85 nm, 140 nm, 250 nm with increasing MWs of 23 kDa, 32 kDa, 54 kDa, and 125 kDa, respectively, in their batch nanoprecipitation (BN) process under magnetic stirring at 300 RPM [251]. We hypothesize that MW does not affect particle size between 8 kDa to 54 kDa despite differences in viscosity

and polymer MW in our reactor. Others have reported similar findings with PLGA (12 kDa to 48 kDa) and polycaprolactone (PCL) (2 kDa to 80 kDa) NPs [252, 253]. As such, these experiments served as repeats to measure the variability of the system in addition to the repeats done at the same MW (standard deviation (SD) = 6 nm, $n = 5$).

Table (4.4) Particle size vs. MW (C1)

Size (nm)	NPs' Đ	MW (kDa)	PLA Đ
77	0.11	54	1.35
87	0.10	44	1.36
77	0.14	27	1.03
83	0.09	8	1.49

4.3.2 Transmission Electron Microscopy

The rs-SDR produced spherical particles (PLA and PLA-PEG) regardless of the experimental parameters (Figure 4.1). We initially hypothesized that an increase in the rotational speed would stretch the particles from spheres to ovals or even needle-like shapes. This stemmed from a tf-SDR's ability to squeeze/stretch spherical calcium carbonate particles at 1100 RPM to cubic particles at 1650 RPM [120]. However, the PLA and PLA-PEG particles remained spherical across all tested speeds (1500 to 5000 RPM). PLA is hydrophobic and minimizes its contact with the water-rich environment by remaining spherical.

4.3.3 Diffusion Limited Coalescence

Lebouille et al. expanded upon the theoretical framework for nanoprecipitation put forth by Lannibois et al. [254] and developed an analytical expression to predict the size of NPs based on a kinetic model for diffusion limited coalescence (DLC) (Equation 4.10). [255]. It quantifies transport and diffusion mechanisms in the nanoprecipitation process. It is the mixing time, diffusivity of the polymer and the surfactant that determine the final radius of the NPs (Equation 4.10).

$$R_{\mathrm{p}} = R_{\mathrm{p0}}(1+k)\left(1+\frac{\tau_{\mathrm{mix}}}{\tau_{\mathrm{cls}}}\right)^{1/3} \tag{4.10}$$

Where $R_{\mathrm{p0}} = (\frac{3M_{\mathrm{p}}}{4\pi N_{\mathrm{p}}\rho})^{\frac{1}{3}}$ is the smallest possible radius for the NPs [244]. M_{p} is the molecular weight of the polymer, N_{A} is Avogadro's number, and ρ is the density of the polymer, which we assumed to be constant at $1000\,\mathrm{kg\,m^{-3}}$. k represents the total area surfactant molecules

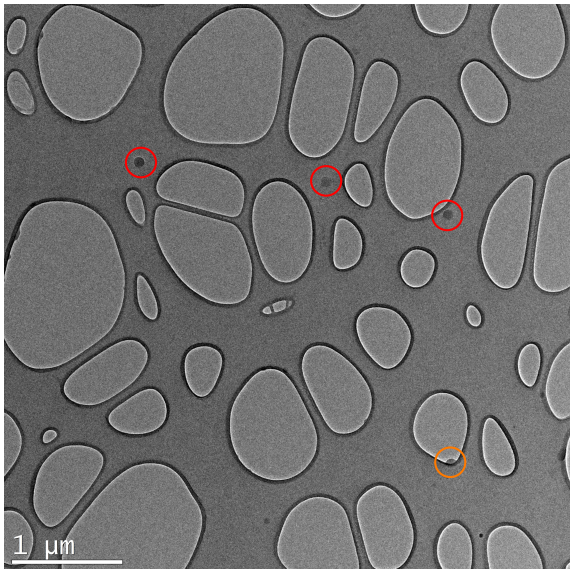

(a) PLA NPs (ID: A6).

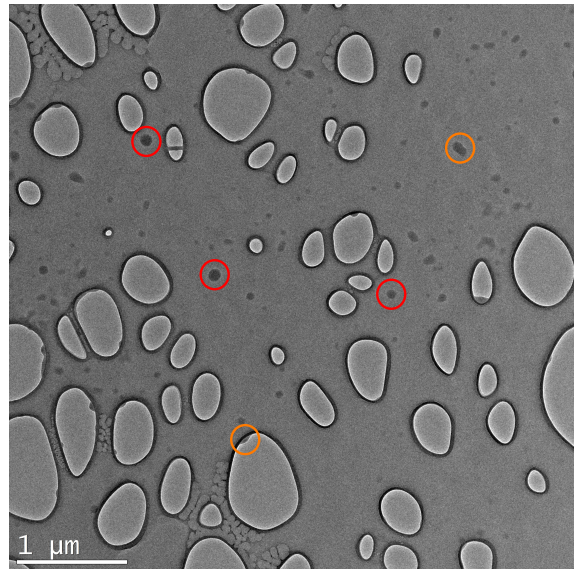

(b) PLA-PEG NPs (ID: PP2).

Figure (4.1) TEM images of PLA and PLA-PEG NPs. The red circles highlight well-shaped spherical particles. The orange circles highlight melting particles as a result of the beam from the TEM; images must be taken quickly to avoid complete deformation.

can cover. Finally, we calculate τ_{mix} from Section 4.2.7 and the coalescence time from $\tau_{\text{cls}} = \frac{3}{8}(\frac{\eta}{kT})(\frac{M_{\text{w}}}{N_{\text{A}}C_{\text{p}}})$ [255]. η is the dynamic viscosity of the solution, k is the Boltzmann constant, T is the temperature, M_{w} is the polymer molecular weight, and C_{p} is the concentration of polymer in the organic phase. For nanoprecipitation to occur, the organic and aqueous phases must be mixed more rapidly than the time spent in the reactor ($\tau_{\text{mix}} < \tau_{\text{res}}$). In our system, mixing times range from 0.03 ms to 0.19 ms while residence times are on the order of s. Moreover, if $\frac{\tau_{\text{mix}}}{\tau_{\text{cls}}} << 1$ the mixing is pseudo-instant and the particle radius tends to R_{p0} and depends on the MW of the polymer. When $\frac{\tau_{\text{mix}}}{\tau_{\text{cls}}} > 1$, the final particle size tends to follow $\left(\frac{\tau_{\text{mix}}}{\tau_{\text{cls}}}\right)^{1/3}$ and is independent of the MW of the polymer [244, 255], as we also demonstrated experimentally (Table 4.4). Our precipitations occur in this slow mixing regime and without surfactant. As a result, we modified Equation 4.10 by removing the surfactant term and folding in R_{p0} into a constant, β_0, since the final size will not tend towards it (Equation 4.11).

$$R_{\text{p}} = \beta_0 \left(1 + \frac{\tau_{\text{mix}}}{\tau_{\text{cls}}}\right)^{1/3} \tag{4.11}$$

The experimental data fits the DLC model and collapses onto a master curve (Figure 4.2). The model explains 80 % of the variance in the pulsed experiments, 89 % in the continuous,

and 77 % if both are considered as a single dataset. The concentration of polymer in the organic phase increases the final particle size — when τ_{cls} decreases due to a higher concentration the final size increases [255]. In addition, as the rotational speed increases, τ_{mix} decreases, and so the final size decreases.

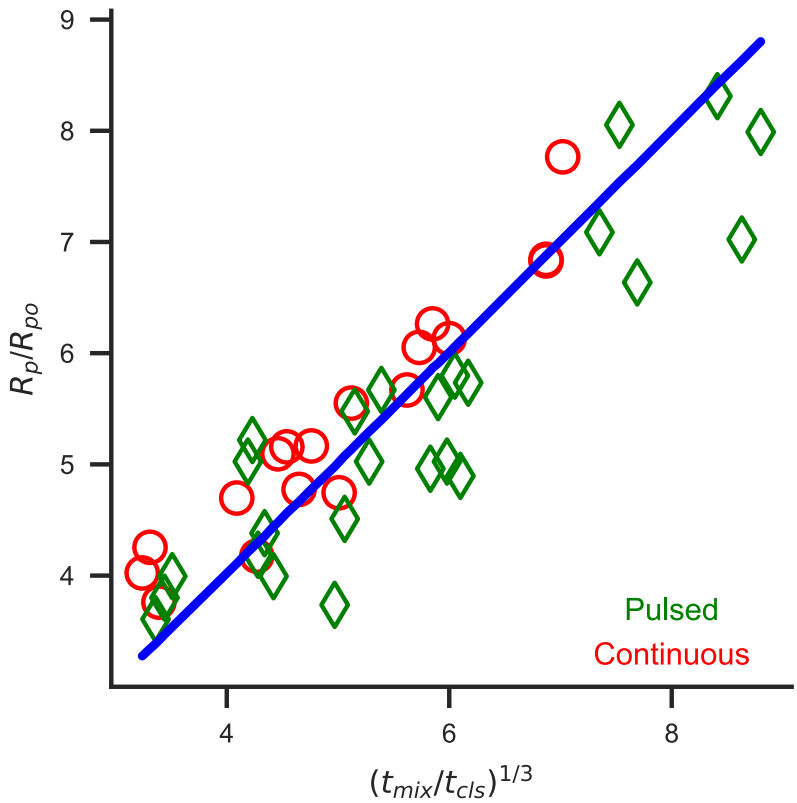

Figure (4.2) Rescaled mixing time and particle size of the experimental data overlayed onto the master curve depicting the DLC model. Pulsed: $R^2 = 0.80$, continuous: $R^2 = 0.89$, pulsed and continuous combied: $R^2 = 0.77$.

Our data reinforces the theoretical model developed by Lebouille et al. — NP size scales universally and is governed by the mixing time and the concentration of polymer in the organic phase in the slow mixing regime [255]. To date, it holds true for different polymer systems (PLA, PEG-*b*-PLA, PCL) and different NP synthesis techniques (batch, pressure injection, impinging jet mixer, herringbone mixer, rs-SDR) [244, 255], at flowrates in the low $\mathrm{mL\,min^{-1}}$ and high $\mathrm{mL\,min^{-1}}$ range. Thus, with the DLC model, it is possible to predict and adapt the NP size to suit clinical- and industrial-scale production.

4.3.4 Statistical Model for the Nanopreciptation of Polylactic Acid

We also regressed our experimental data according to a power law model (Table 4.5) to explore the explicit effects of the parameters in the DoE (rotational speed, flowrate ratio, concentration of PLA in acetone) on the particle size and $Đ$.

Pulsed

Initially, the regression contained four factors: concentration of PLA in the feed solution (C, mg/mL), total flowrate (F, mL/min), rotational speed (RPM), and the ratio of acetone:water (R). F and R had the strongest influence on the particle size according to the model ($R^2 = 0.82$) — 0.78 and 0.73 versus 0.31 and -0.35 for C and ω, respectively (Table 4.5). However, F and R exhibit collinearity since while the flowrate of the acetone feed remains constant at 10 mL, a change in the flow of water affects the total flowrate and ratio of acetone:water, simultaneously. Thus, when both factors are included in the model, their coefficients overestimate their effect on particle size. By removing either F or R, we can isolate their individual contributions; the model compensates by readjusting the relative importance of the factors. Without R, F's associated coefficient plummets to -0.05, while the R^2, β_1, and β_2 remain unaffected. An increase in F actually decreases the particle size, it's influence, however, is much lower than C and ω. Similarly, without F, R's coefficient decreases to 0.05, while R^2, β_1, and β_2 do not change. An increase in R increases the particle size, but again, its effect on the particle size is overshadowed by C and ω. Finally, eliminating both F and R only decreases the model's explanation of the variance by 1 % (Table 4.5). In other words, the total flowrate and the acetone:water ratio in pulsed experiments have negligible effects on the final particle size. As we are only injecting a brief 5 mL pulse of PLA in acetone, this is unsurprising as the ratio of acetone:water is more dominant with a continuous stream of PLA mixed acetone, as is common in continuous flow systems (e.g., microfluidics) [256]. In addition, the residence times decrease from 76 s to 10 s as the total flowrate increases from 15 mL min^{-1} to 120 mL min^{-1}, which is still 5 orders of magnitude higher than the mixing time and thus does not affect the final size of the NPs, as per the DLC model. An increase in the concentration of PLA in the acetone solution increases the final particle size, while an increase in the rotational speed decreases the particle size (Figure 4.3). Both these factors affect the mixing time and the coalescence time in a way consistent with the theoretical framework for nanoprecipitation [254, 255].

As the rotational speed of the disk increased so did $Đ$ of the particles (Figure 4.4). At 5000 RPM, there was pronounced backflow in the reactor potentially causing particles to prematurely precipitate thereby increasing the $Đ$ of the sample.

Table (4.5) Power model with varying parameters

Equation	β_1	β_2	β_3	β_4	R^2
$C^{\beta_1}\omega^{\beta_2}F^{\beta_3}R^{\beta_4}$	0.31	-0.35	0.78	0.73	0.82
$C^{\beta_1}\omega^{\beta_2}F^{\beta_3}$	0.31	-0.35	-0.05	-	0.82
$C^{\beta_1}\omega^{\beta_2}R^{\beta_3}$	0.31	-0.35	0.05	-	0.82
$C^{\beta_1}\omega^{\beta_2}$	0.31	-0.35	-	-	0.81

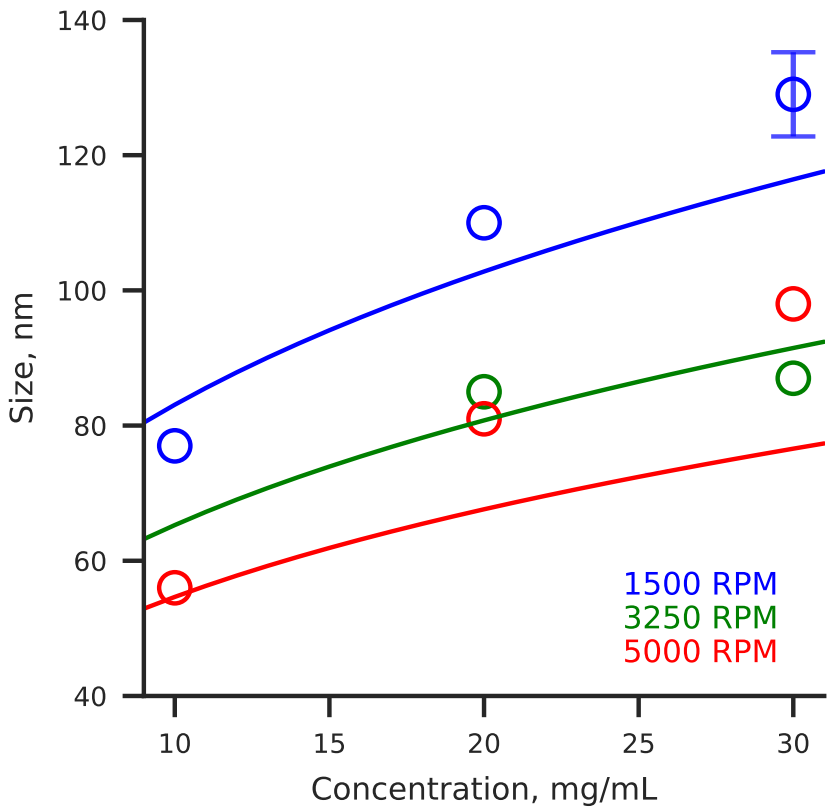

Figure (4.3) Size of PLA in pulse-mode nanoprecipitation at a acetone:water ratio of 1:11. The lines depict the statistical model and the circles, the experimental data.

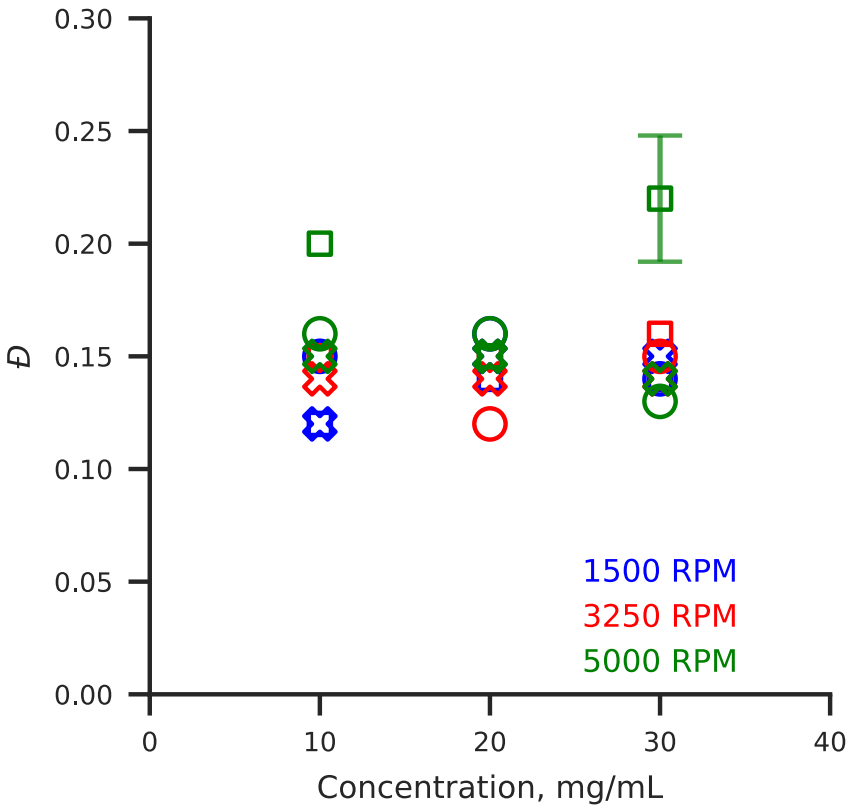

Figure (4.4) $Đ$ of the PLA NPs in pulse-mode nanoprecipitation. The symbols represent the different flowrate ratios: circle = 1/11, square = 1/5, cross = 1/3.

Continuous

We also regressed the experimental data for the continuous nanoprecipitation of PLA in the rs-SDR with a power law model (Equation 4.12, $R^2 = 0.88$).

$$D_{\text{continuous}} = 232C^{0.27}R^{-0.13}\omega^{-0.34} \tag{4.12}$$

D is the Z_{avg} diameter/size of the particles (nm). The model fits the continuous data better than the pulsed data ($R^2 = 0.88$ vs. 0.81). As long as the residence time in the reactor is greater than the mixing time, the total flowrate will have no effect on the particle size, according to the DLC model. We also demonstrated this experimentally, between 48 mL min^{-1} to 120 mL min^{-1} (Table 4.6) and thus fixed the total flowrate to 60 mL min^{-1}. Even if we consider that the nanoprecipitation occurs in first disk only ($V \approx 9$ mL) and the corresponding residence times drop to 11 s, 9 s, and 5 s for total flow rates of 48 mL min^{-1}, 60 mL min^{-1}, and 120 mL min^{-1}, respectively, the mixing time remains 4 orders of magnitude lower.

Table (4.6) Particle size and $Đ$ as a function of total flowrate. C, R, and ω were constant.

F (mL min^{-1})	Size (nm)	$Đ$
48	93	0.14
60	94	0.11
120	89	0.12

R has more impact and in the opposite direction in determining the particle size in continuous nanoprecipitation compared to pulsed ($R^{-0.13}$ vs. $R^{0.05}$). As R increases, the particle size decreases, whereas generally the reverse is true [74, 88]. We hypothesize that increasing the flowrate of the acetone feed enhances the mixing and shear forces at the water-acetone interface when the two phases initially clash, leading to more homogeneous supersaturation and nucleation. Nevertheless, R's influence on the particle size is a fraction of C's and ω's in likeness to the pulsed experiments. These two maintain their effects on the particle size (Figure 4.5) in a consistent manner with the theoretical framework for nanoprecipitation.

The $Đ$ of NPs in continuous mode follow no discernable trend with regards to the experimental parameters (Figure 4.6). The particles are highly uniform with a dispersity ranging from 0.09 to 0.19. Overall, the rs-SDR can produce PLA particles ranging from 60 nm to 120 nm by varying C and ω. PLA-PEG follows a similar trend as PLA. At 1500 RPM, a R of 1/11, and increasing concentrations of PLA-PEG in acetone (5 mg mL^{-1} to 15 mg mL^{-1}) the particle size ranged from 60 nm to 130 nm.

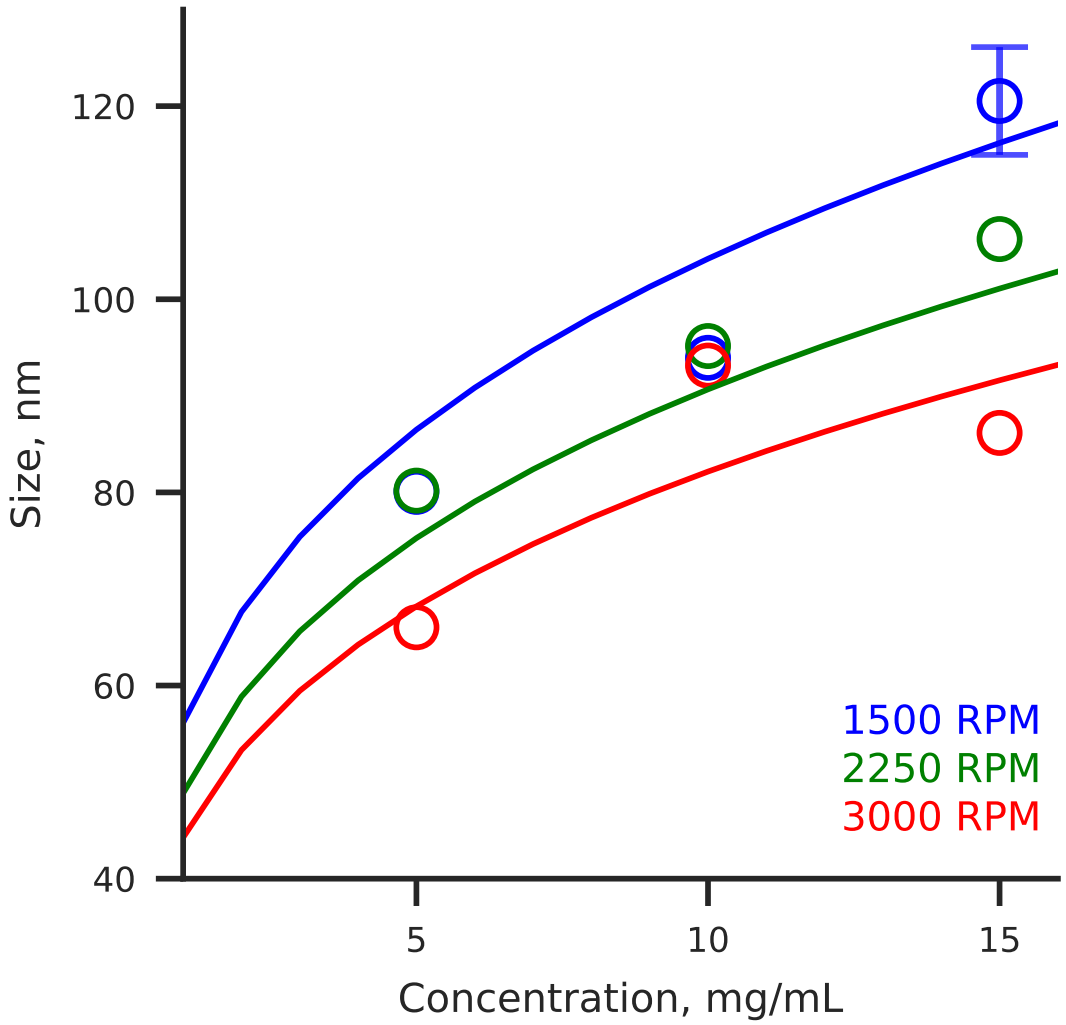

Figure (4.5) Size of PLA in continuous-mode nanoprecipitation at a acetone:water ratio of 1:11. The lines depict the statistical model and the circles, the experimental data.

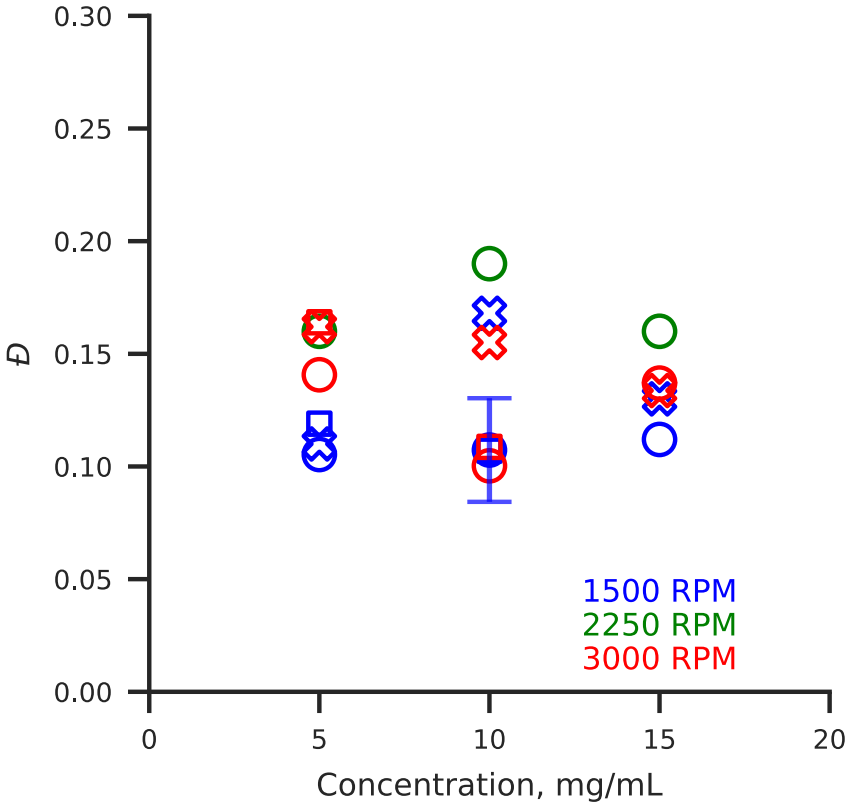

Figure (4.6) $Đ$ of the PLA NPs in continuous-mode nanoprecipitation. The symbols represent the different flowrate ratios: circle = 1/11, square = 1/5, cross = 1/3.

4.3.5 Drug Loading in an rs-SDR

The rs-SDR can produce uniform NPs in the desirable range for drug delivery systems. In order to be an eligible technology for these drug delivery systems, the rs-SDR must also be able to load drugs into the NPs. As a result, we tested the rs-SDR's ability to load ibuprofen into PLA plus PLA-PEG and acetaminophen into PLA-PEG. We do not expect any loading with acetaminophen as it is hydrophilic and the PEG forms a shell around the PLA to make it more stable in water. We loaded at drug:polymer (D:P) ratios (% w/w) of 5 to 20 and fixed F, R, C, and ω at 60 mL min^{-1}, 1/11, 5 mg mL^{-1}, and 1500 RPM, respectively. The NP size for PLA loaded with ibuprofen increased from 89 nm at a D:P of 5 to 118 nm at a D:P of 20. The $Đ$ was constant across D:Ps at an average of 0.15. For PLA-PEG loaded with ibuprofen the size increased from 120 nm at a D:P of 5 to 136 nm at a D:P of 20. PLA-PEG loaded with acetaminophen showed no change in size, with an average of 108 nm across D:Ps. DL and EE for PLA and PLA-PEG were similar across D:Ps (Figures 4.7, 4.8). Peak DL and EE for PLA-ibuprofen was 6 % and 30 %, respectively. For PLA-PEG-ibuprofen, peak DL and EE was 5.5 % and 37 %, respectively. The rs-SDR was unable to load any acetaminophen in PLA-PEG as this drug is water soluble and will preferentially dissolve into the aqueous phase as opposed to associating with PLA-PEG.

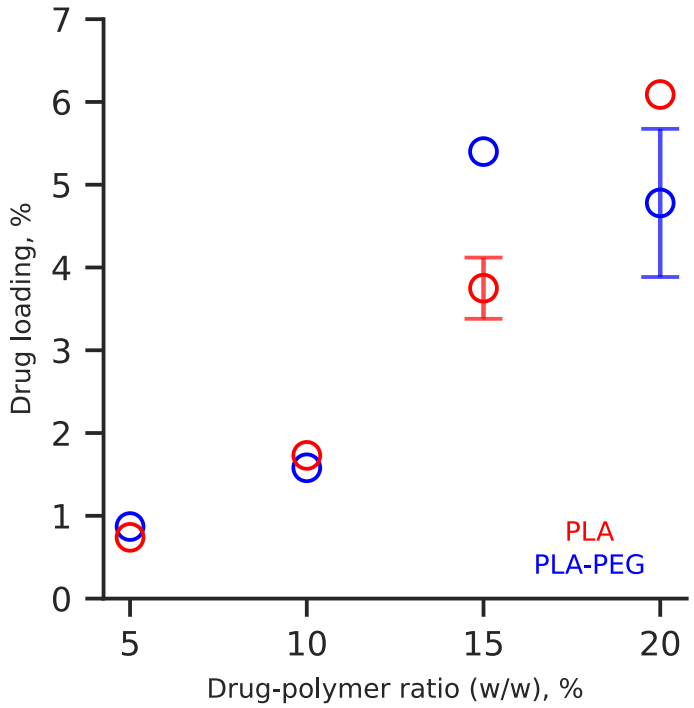

Figure (4.7) Drug loading.

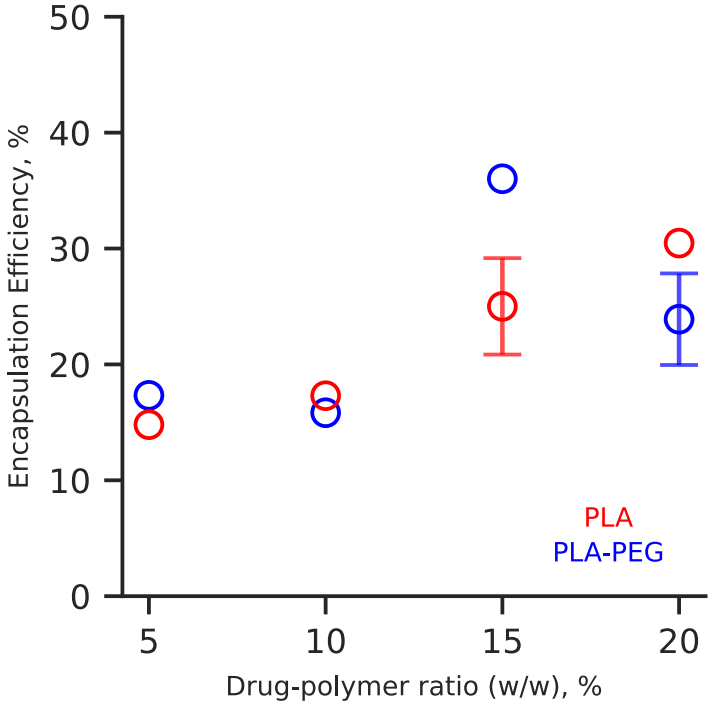

Figure (4.8) Encapsulation efficiency.

The partition coefficient, P, in the pharmaceutical industry is a tool to measure how drugs/-molecules move between biological environments and their hydrophobicity [257]. Ibuprofen is highly hydrophobic with a solubility in water of approximately 20 ppm and a measured P of 2.5-3.5 [258, 259]. Ketoprofen has a similar profile with a P of 3.1 [260] and is more common in the literature, thus we use it as a basis for DL and EE comparison. At a D:P of 20 with a PLA-PEG (MW = 34 kDa, 8.3 % w/w PEG content) and ketoprofen system, BN, CIJM, and a staggered herringbone micromixer (SHMN) had DL of 4 %, 6 %, and 7 %, respectively [244] — the rs-SDR achieved 6 %. In addition, the max EEs at a D:P of 10 for BN, CIJM, and SHMN was 25 %, 20 %, and 35 %, respectively [244]. At this same D:P for the rs-SDR the EE for PLA was 17 % and for PLA-PEG 18 %. Multiblock copolymer PLA-PEG (MW = 4 kDa, 8.9 % w/w PEG content) NPs prepared by an HPH emulsion-solvent evaporation method had an EE of 25 % with ibuprofen as the model drug [261]. Overall, the DL across different methods, polymers, and drugs often ranges from 1 % to 15 % [262, 263, 264, 265, 266, 267]; the rs-SDR is able to load drugs at a level similar to other techniques further reinforcing its suitability for large-scale production of particles in a pharmaceutical setting.

4.3.6 Nanoprecipitation Technologies: Potential for Scale-Up

Nanoprecipitation in microfluidic channels consistently produces NPs suited for drug delivery purposes (narrow particle size distributions plus batch-to-batch reproducibility). The factors that govern a microfluidic system are the size of the microchannels, the total flowrate, the flowrate ratio, the polymer concentration, the drug concentration, the chosen organic solvent, and the type(s) of polymer. The potential for customization grants the ability to tune NP size, distribution, as well as drug loading and release. For instance, with a PDMS HFF microfluidic channel and PLGA-PEG, the particle size was reproducible to within 1 nm [90]. However, this degree of reproducibility was limited to the same batch of polymer; the authors did not report the uncertainty across polymer batches. The shortcomings of microfluidics lies in scale-up, as organic solvents are incompatible with PDMS channels and it is costly and complex to fabricate glass or silicon channels. In addition, it is difficult to replicate reactors (scaling requires parallelization) and their channels, to maintain consistent mixing across all channels, and to distribute reagents across the entire system. Furthermore, they generally synthesize on the order of µg to mg [227]. Target clinical study and industrial-scale production rates are $100\,\mathrm{g\,d^{-1}}$ and $1\,\mathrm{kg\,d^{-1}}$, respectively [11].

PLGA, a common drug-carrying polymer aggregates onto the walls of PDMS-based microfluidic channels, which hinders scale-up [107]. In diffusion and convection microfluidic mixers, production rates peak at $0.07\,\mathrm{g\,d^{-1}}$ and $0.36\,\mathrm{g\,d^{-1}}$, respectively [90, 242]. HFF solves aggregation issues and increases production rates. This technique squeezes fluid flow into a thin stream along the microfluidic wall (2D) to reduce diffusion distance as well as enhance mixing at low pressures [268, 269, 270]. In 3D HFF, there are two sheath flows that create a thin stream in the center of the channel, which reduces aggregation [271]. The properties of NPs synthesized with 2D HFF and 3D HFF are similar [108]. A single 3D HFF PDMS microchannel synthesized PLGA-PEG at a production rate of $0.25\,\mathrm{g\,d^{-1}}$; the authors then created a system of 8 parallel microchannels to produce $2\,\mathrm{g\,d^{-1}}$ [109]. The production rate of PLGA NPs in PDMS-based microfluidic chips is generally less than $7.2\,\mathrm{g\,d^{-1}}$ [107]. Alternatively, PDMS as the base material for microfluidic channels can be eliminated in favour of glass or PTFE — this eliminates all aggregation issues associated with PDMS and elevates the system's endurance to pressure [107]. The latter translates to higher permissible flow rates and thus higher production rates. For example, glass capillary devices are able to produce PLGA NPs at production rates of $240\,\mathrm{g\,d^{-1}}$ with a single microchannel [241]. In addition, glass is resistant to a plethora of chemicals and can withstand higher pressures than PDMS, permitting more process diversity. Nonetheless, glass is difficult to micro-fabricate and does not have the ability to mold into complex channel shapes like PDMS [110]. The

latter affords more control over the nanoprecipitation process and thus can produce more complex NPs [107]. Eight PID microchannels, on the other hand, coupled with 3D HFF produced PEG-PLGA NPs at 300 g d^{-1} [99]. However, the standard deviation of the PEG-PLGA NPs synthesized at this rate is approximately 25 nm. In addition, PID microchannels are fabricated via laser ablation and resulting properties such as surface roughness cannot be controlled and vary with manufacturing parameters [272]. In another example, COP-based microfluidic channels were capable of producing PLGA NPs at 324 g d^{-1} [98].

Outside of microfluidics and in terms of mixers, a PTFE-based CTJM, a collection of coaxial cylindrical tubes in which the anti-solvent flows through an outer tube and NP precursors are injected into the anti-solvent via an inner tube with a syringe needle, output NPs at a rate of 3 kg d^{-1} while maintaining control over particle size (25 nm to 100 nm) [11]. Furthermore, the company KNAUER offers industrial-scale impinging jet mixers for NPs. These mixers produce particles via a flash nanoprecipitation process through the clashing of two streams (jets) in a confined volume that collide at high velocity producing a turbulent regime for mixing [273, 274]. One SingleCore NanoProducer from KNAUER can output NPs at 7.2 kg d^{-1}, with each extra unit adding another 7.2 kg d^{-1}.

We propose the rs-SDR for clinical- and industrial-scale NP synthesis. In the FlowID SpinPro R2 (V = 19 mL), we can produce PLA NPs at a rate of 864 g d^{-1} (Table 4.5). In addition, the resulting particle sizes are fit for drug delivery purposes (between 50 nm to 150 nm), have low $Đ$ (0.1 to 0.22), and are reproducible within and across polymer batches. The standard deviation for size was 6 nm and 0.02 for $Đ$ in the continuous experiments. The deviations for size in microfluidics are generally higher, i.e. 20 nm or more [101, 105]. In many cases, the dispersities are also higher ranging from 0.1 to 0.5 [101, 242, 275].

Table (4.7) Production Rates in the rs-SDR

C, mg/mL	F, mL min^{-1}	Production Rate, g d^{-1}
5	10	72
	24	173
	40	288
10	10	144
	24	346
	40	576
15	10	216
	24	518
	40	864

FlowID designs their SpinPro reactors to maintain similar performances per unit volume

across different sizes. For example, the pilot scale SpinPro R3 ($V = 166\,\mathrm{mL}$) retains mixing times in the ms range even with a max allowable flowrate through the reactor of $600\,\mathrm{L\,h^{-1}}$. At our experimental conditions, the mixing times in the R2 range from 0.1 ms to 0.2 ms and in the R3, the mixing times would range from 0.1 ms to 1 ms. The G in the R3 is identical to the R2 while r_D increases from 0.035 m to 0.075 m. At a total flowrate of $600\,\mathrm{L\,h^{-1}}$, a flowrate ratio of 1/3, and a concentration of PLA in acetone of $15\,\mathrm{mg\,mL^{-1}}$, the R3's production capacity peaks at $54\,\mathrm{kg\,d^{-1}}$ outperforming KNAUER's industrial scale impinging jet mixers as well as all other technologies in the literature (Table 4.1). One R3 reactor equates to 7.5 industrial scale impinging jet mixers. The industrial scale SpinPro (R4) is still in development and is thus omitted from our analysis. The mixing time in the R3 is still lower than the residence time at $600\,\mathrm{L\,h^{-1}}$ (1 s). In addition, the predicted NP sizes in the R3 are only 10 nm to 20 nm larger than the R2, well within the desired range for drug delivery systems.

4.4 Conclusion

We have developed a new process for the continuous production of drug-loaded PLA NPs in an rs-SDR. Micromixing times in the R2 by Flowid ranged from 0.03 ms to 0.2 ms across pulse-mode and continuous-mode nanoprecipitation and rotational speeds between 1500 and 5000 RPM. This process produces NPs with sizes ranging from 58 nm to 132 nm, with $Đ$ between 0.1 and 0.2. Peak DL and EE with ibuprofen in PLA peaked at 6 % and 30 %, respectively, at a D:P of 20. For PLA-PEG, these values reached 5.4 % and 36 %, respectively, at a D:P of 15. In the R2 reactor, the max production rate is $864\,\mathrm{g\,d^{-1}}$ and theoretically climbs to $54\,\mathrm{kg\,d^{-1}}$ in the R3. The next steps involve validating this process with other polymer combinations (e.g., PLGA) and drugs, lipids, and mRNA. In addition, reproducing the process in the larger rs-SDRs (e.g., the R3 and R4 from FlowID) to confirm whether scale-up is feasible or collapses at much higher flowrates.

CHAPTER 5 MIXING AND HYDRODYNAMICS IN A ROTOR-STATOR SPINNING DISK REACTOR

5.1 Introduction

As previously mentioned, rs-SDRs have been studied in a wide range of applications including photochemical oxidation and degradation [135, 235], chromium (III) extraction [236], trans-esterification of triglycerides [137], esterification of free fatty acids [240], and the synthesis of $BaTiO_3$ NPs [138]. They are a type of PI technology that offers low mixing times [129, 134], high heat [126, 230, 231] and mass [124, 228, 229] transfer (compared to packed columns and microchannels) with energy dissipation rates (ϵ) that can attain values of $1 \times 10^5\,\mathrm{W\,kg^{-1}}$ [123], making them highly effective for multiphase reactions (liquid-gas, liquid-liquid, and gas-liquid-liquid) [33].

In a short recap of their features, these reactors typically contain one or more rotating disks housed within a narrow casing, which generate significant shear and centrifugal forces, thereby improving mixing. In addition, the spinning disks create two boundary layers — one at the rotor and one at the stator, called the Von Kármán layer and the Bödewadt layer, respectively. Without superposed throughflow ($C_w = 0$, where $C_w = Q\nu^{-1}r_D$) the Von Kármán layer generally exhibits centrifugal radial velocity with a characteristic net negative radial velocity, i.e., fluid flows inward. On the other hand, the Bödewadt layer exhibits centripetal radial velocity with a characteristic net positive radial velocity, i.e., fluid flows outward [144]. With superposed throughflow ($C_w > 0$), the radial velocity is positive in the Von Kármán layer and negative in the Bödewadt layer [144]. Rs-SDRs can operate in four different flow regimes based on the rotational Reynolds number and G [143, 156]. These flow regimes are classified I through IV and exhibit either merged or distinct boundary layers (Von Kármán [276] and Bödewadt [277]):

- I (III): laminar (turbulent) flow with merged boundary layers on the rotor and stator; a continuous variation of velocity exists across h
- II (IV): laminar (turbulent) flow with separated boundary layers and a region in between with no changes in velocity

If we recall that drug side effects are responsible for approximately 3% of all deaths worldwide [215] and that production rates in continuous flow processes, like microfluidic systems, have not been scaled up, to date, to satisfy large-scale clinical trials and industry ($100\,\mathrm{g\,d^{-1}}$,

$1\,\mathrm{kg\,d^{-1}}$, respectively) [11, 227], then rs-SDRs are an attractive technology as we have already produced drug-loaded NPs at rates in the hundreds of g with the lab-scale R2. We believe that these commercial rs-SDRs (that operate in flow regime III), are well-suited for producing nano-sized drug delivery systems due to their low micromixing times (ms), which impacts particle size, dispersity, and drug loading, and highly permissible throughputs (hundreds of mL to hundreds of L). However, to better understand and leverage these reactors' ability to produce NPs, investigations into how the experimental conditions and reactor geometry affect the hydrodynamics is crucial. There already exist studies of this kind that take varying approaches, from experimental to numerical methods using CFD (**Table 5.1**). However, in the current CFD studies, the inlets are separated by the reactor's shaft; the fluids do not immediately interact upon entering. This chapter quantifies the effect of the disk rotational speed on the fluid dynamics of the first disk from FlowID's R2 three-stage SDR. We begin by verifying that the time-averaged velocity profiles spatially converge before discussing the transition and critical mixing radii to describe the mixing capabilities of the R2. Finally, we broach the time-averaged velocity profiles along the disk to verify their behaviour in relation to the literature and commonly observed phenomena in rs-SDRs.

5.2 Theoretical Background

Mixing is a crucial aspect of synthesizing nano-sized drug delivery systems. Inadequate mixing leads to large particle sizes unsuitable for drug delivery ($> 200\,\mathrm{nm}$), diverse size distributions, and failed drug loading. Nanoprecipitation is the culmination of reactant mixing at the micro- and macro-scale as well as subsequent nucleation and growth of the particles. More specifically, it is supersaturation that dominates the mechanism and kinetics of the nucleation and growth processes. For nano-sized drug-delivery systems, homogeneous nucleation is necessary as it ensures more uniform particle sizes — which is crucial for quality control ($Đ < 0.2$ [279]) — compared to heterogeneous nucleation. The mixing intensity (governed by the rotational speed and flowrate) is a major driver of particle size and distribution because it influences all steps of nanoprecipitation (phase separation, nucleation, growth, and aggregation) [280, 281].

5.2.1 Micromixing - Recap

On the micro-scale, the DLC model quantifies the diffusion and transport mechanisms of nanoprecipitation while the polymer, the surfactant diffusivity, and mixing time dictate the size of the NPs (Equation 4.10) [254, 255]. [134] calculated τ_{mix} in rs-SDRs between $10\,\mathrm{rad\,s^{-1}}$ and $188\,\mathrm{rad\,s^{-1}}$ to be $9\,\mathrm{ms}$ to $0.1\,\mathrm{ms}$. If we assume water as the fluid and follow the same

Table (5.1) A summary of literature studying the hydrodynamics in rotor-stator systems. * is a theoretical study of the boundary layers between two parallel infinite disks. G is the gap ratio ($G = h/r_D$). Re_{TC} is the Taylor-Couette Reynolds numbers, i.e., $r_{\mathrm{disk}} \times \omega \times (r_{\mathrm{stator}} - r_{\mathrm{disk}}) \times \nu^{-1}$. Abbreviations are as follows: EXP = experimental, LES = large eddy simulation, ILES = implicit large eddy simulation, PMM = predictive math model, NA = numerical and analytical, NRTM = numerical reaction transport model, and VKE = volume of fluid plus $k - \epsilon$ model. [1]assuming fluid is water.

Ref.	Methodology	G	Re	Re_{TC}	C_w
[143]	EXP	0.013 to 0.22	10^3 to 10^6	-	0
[152]	EXP	0.08	10^5 to 10^6	-	0
[153]	EXP	0.007 to 0.14	10^4 to 10^5	900 to 17000	0
[154]	EXP	0.012, 0.036	10^5 to 10^6	12000 to 50000[1]	0, 2579, 5159, 10317
[155]	EXP	0.036	10^6	12000 to 50000[1]	0, 1976, 5929, 9881
[159]	LES	5	10^5 to 10^6	600 to 6000	0
[278]	EXP	0.024, 0.036, 0.048	10^6	8000 to 50000	10317
[161]	PMM	0.05 to 0.5	Based on [152, 159]	Based on [152, 159]	0
[160]	LES	36.5	10^5	-	0
[162]*	NA	-	-	-	-
[156]	LES	0.0303	10^4 to 10^5	600 to 5000	150
[157]	NRTM	-	-	-	-
[158]	VKE	0.01	10^3 to 10^5	200 to 3000	2 to 67
[144]	EXP	0.017, 0.03	10^4 to 10^6	6000 to 300000	127, 211, 295, 421
This article	ILES	0.014	10^4 to 10^5	1300 to 5500	29

methodology, the τ_{mix} in our simulated disk ranges from 2 ms at 38 rad s^{-1} to 0.1 ms at 314 rad s^{-1}. For nanoprecipitation to occur without large size distributions, the polymer and aqueous solutions must be mixed more rapidly than the residence time of the reactor ($\tau_{\mathrm{mix}} < \tau_{\mathrm{res}}$). The residence time in rs-SDRs is V/Q, where V is the volume of the reactor and Q is the flowrate. Our τ_{res} ranges from 18 s to 4.5 s at 30 mL min^{-1} to 120 mL min^{-1}, with a volume of 9 mL (for the first disk) meaning that nanoprecipitation will occur.

5.2.2 Transition Radius and Flow Profiles

Bulk flow behaviour in rs-SDRs with positive throughflows ($C_w > 0$) generally has two zones. The first zone, near the inlet and outlet, behaves as a PFR and is throughflow dominant, whereas the second zone, further along the disk, behaves as a CSTR and is rotation dominant. The transition radius, r_{t} (Equation 5.1), is defined as the radius at which the behaviour transforms from PFR to CSTR [278, 282].

$$r_{\mathrm{t}} = \left(\frac{1}{c}\frac{C_w}{\mathrm{Re}^{0.8}}\right)^{\frac{5}{13}} r_D \tag{5.1}$$

For the case of torsional Couette, in the throughflow region (top and bottom parts of the disk,

i.e., D_E and D_O from Figure 5.1), the time-averaged radial velocity in the Bödewadt layer is almost linear and has a smaller magnitude compared to the flow in the Von Kármán layer, while the time-averaged azimuthal velocity is zero outside of the Von Kármán layer. As the flow approaches r_t, the flow magnitude in the Bödewadt layer approaches zero and decreases in the Von Kármán layer. Once r_t is crossed, the velocity gradients in both layers (positive in the Von Kármán layer and negative in the Bödewadt layer) increase as rotation-governed flow dominates [144, 156]. In the lateral zones of the disk, the flow is reminiscent of classic Taylor-Couette with the formation of toroidal vortices [283].

5.3 Model Formulation

We simulate the flow in the reactor using `Lethe` [149], an open-source CFD software based on the FEM library deal.II [150]. The software applies the FEM to solve the incompressible Navier-Stokes equations:

$$\nabla \cdot \mathbf{u} = 0 \tag{5.2}$$

$$\frac{\partial \mathbf{u}}{\partial t} + (\mathbf{u} \cdot \nabla)\mathbf{u} = -\nabla p^* + \nu \nabla^2 \mathbf{u}. \tag{5.3}$$

where $\mathbf{u}$ is the fluid velocity, p^* is reduced pressure (p/ρ, where p is the pressure and ρ the density of the fluid), and ν is the kinematic viscosity. In `Lethe`, we apply the Streamline-Upwind/Petrov-Galerkin (SUPG) and Pressure-Stabilizing/Petrov-Galerkin (PSPG) stabilization [284, 285]. For details regarding the formulation, we refer the reader to [149]. `Lethe` solves the continuity (5.2) and momentum (5.3) equations in a monolithic fashion using the Newton-Raphson method. The linear systems are solved using the matrix-free implementation of `Lethe` [151] by combining a GMRES linear solver with geometric multigrid preconditioning.

In the formulation, the energy dissipation of eddies that are too small to be adequately resolved by the mesh is accounted for by the induced diffusion of the SUPG term. Hence, we apply an Implicit Large Eddy Simulation (ILES) approach for turbulence. We refer the reader to [151, 286] for further details and information on the validity of the approach.

5.4 Simulation Setup

The mesh was generated with Pointwise, the standard CFD mesh generator [287], and contained 307k elements. The physical parameters for the mesh were taken directly from FlowID's R2 SDR model (**Table 5.2, Figure 5.1**). G and Re are critical in determining the

flow regime; the simulations in this article are in the laminar (at $38\,\mathrm{rad\,s^{-1}}$) and turbulent torsional Couette (at $79\,\mathrm{rad\,s^{-1}}$ and $157\,\mathrm{rad\,s^{-1}}$) flow regimes [144, 288]). Second (Q_1) to fourth (Q_3) order accurate elements were used for velocity and pressure. The time-stepping method for the simulation was 2nd order backward differentiation (bdf2). We set 7 boundary conditions: one for the inlets, two for the disk, two for the casing of the reactor (no slip), one for the outlet wall (slip) and one for the outlet. The kinematic viscosity of the fluid and the tracer diffusivities were set to 1×10^{-6} ($\mathrm{m^2\,s^{-1}}$) and 1×10^{-5} ($\mathrm{m^2\,s^{-1}}$), respectively.

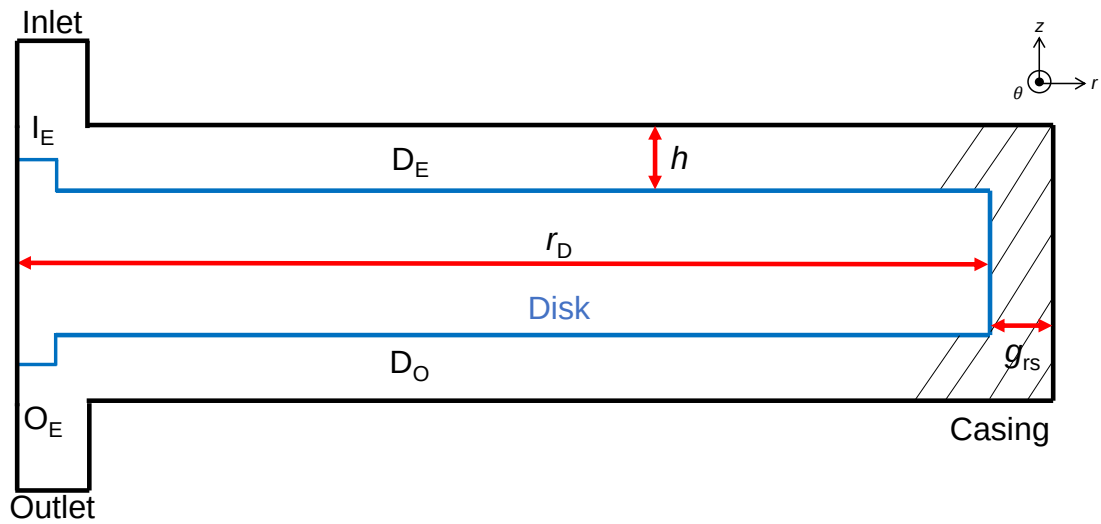

Figure (5.1) 2D slice of the rs-SDR. The left wall is an axis of symmetry. $\mathrm{I_E}$, $\mathrm{D_E}$, $\mathrm{D_O}$, and $\mathrm{O_E}$ represent the entrance of the reactor, the region on the disk where fluid is on its way in, the region of the disk where the fluid is going towards the outlet, and the exit of the reactor, respectively. The shaded part is the sectioned area in the time-averaged velocity in z figures 5.3, 5.10. r_D is the radius of the disk, and g_rs is the axial distance between the disk and the stator.

5.4.1 Mesh Sensitivity Analysis

Figure 5.2 presents the time-averaged radial velocity at three radial position in the interstice at $\mathrm{D_E}$ and Figure 5.3 shows the time-averaged axial velocity between the two cylinders. The time-averaged profiles obtained are converged in terms of spatial resolution for Q_2 and above.

5.5 Results and Discussion

As shown in the theoretical assessment of micromixing time, nanoprecipitation will occur at all permissible flowrates in our model. To further inform future design decisions, we have

Table (5.2) Physical parameters from FlowIDs R2 used for mesh creation and resulting operating conditions.

Physical Parameters
$h = 0.5\,\mathrm{mm}$
$r_D = 35\,\mathrm{mm}$
$g_{rs} = 1\,\mathrm{mm}$
$G = 0.014$
Operating Conditions
$Re = 4.8 \times 10^4$ to 3.8×10^5
$Re_{\mathrm{TC}} = 1.3 \times 10^3$ to 1.1×10^4
$C_w = 29$

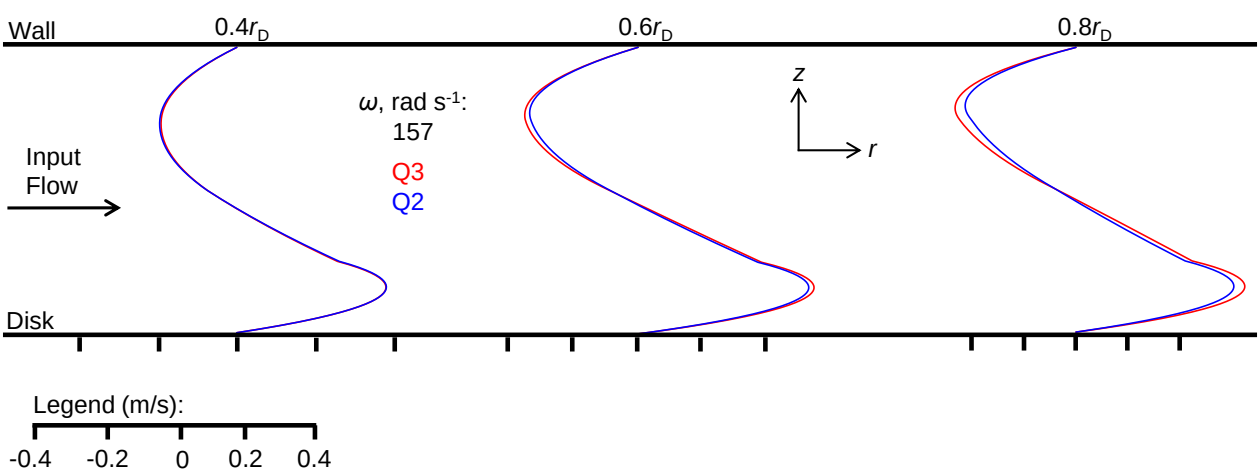

Figure (5.2) Time-averaged radial velocity in Q3 and Q2.

characterized the transition radius, mixing on the macro-scale and the time-averaged velocity flow profiles.

5.5.1 Transition and critical mixing radii

r_{t} demarks the point along the disk at which fluid flow alters from throughflow-dominant to rotation-dominant and is only present at $C_w > 0$. We define the critical mixing radius (on the macro-scale) as the point along the disk at which the injected tracers are 95 % or 99 % mixed with the bulk fluid.

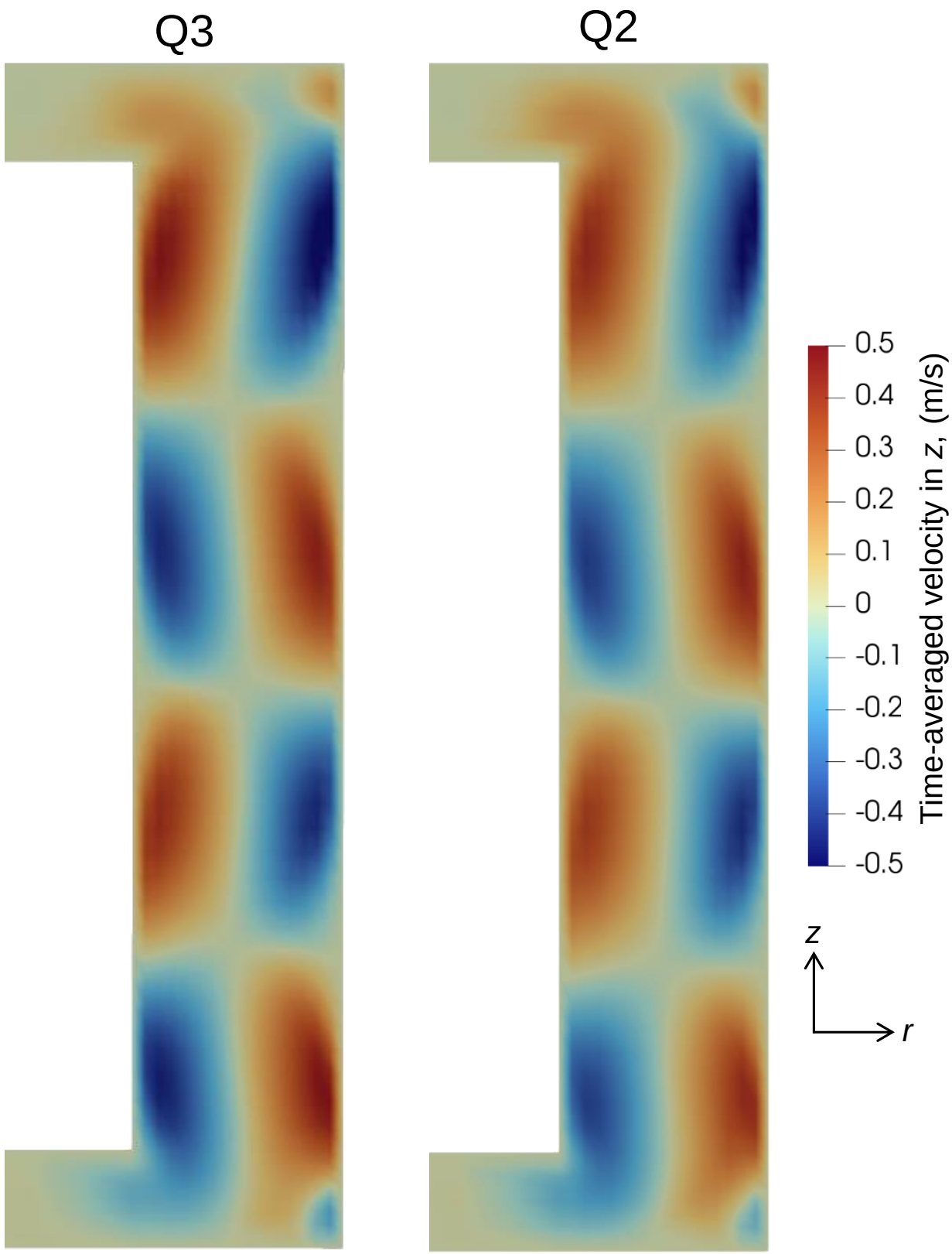

Figure (5.3) Time-averaged velocity in z at Q3 and Q2 with no discernible difference.

Transition Radius

We observed no transition radius in our simulation. All points across the disk, from the center to r_D, are rotation governed with clear radial inflows (Figure 5.4).

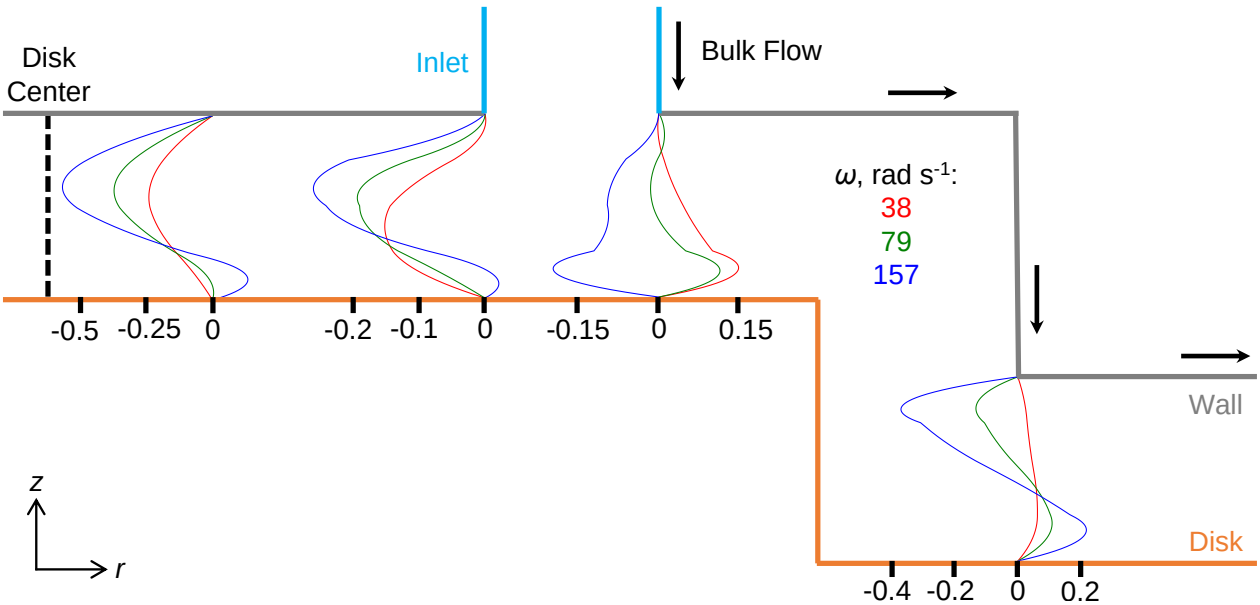

Figure (5.4) Time-averaged radial velocity adjacent to the disk's center, before and after the inlet, and across the dip towards r_{D}.

The two points pre-inlet have strong radial inflows along the Bödewadt layer and a slight radial outflow in the Von Kármán layer. This is in opposition to other studies that have demonstrated positive radial velocities for all axial positions at low radial positions in rotor-stator systems [155, 278, 282, 289]. The same can be said for rs-SDR cases [144, 156], however, the inlets of our geometry are expelling fluid into the same region which eliminates any PFR flow behaviour. Instead, there are strong radial inflows along the stator at all ω and weak radial outflows along the rotor exclusively at $\omega = 157\,\mathrm{rad\,s^{-1}}$ (Figure 5.4). Post-inlet, there is radial outflow along all axial positions at ω of $38\,\mathrm{rad\,s^{-1}}$ (which we attribute to the laminar torsional Couette flow regime), inflows and outflows at $79\,\mathrm{rad\,s^{-1}}$ and at $157\,\mathrm{rad\,s^{-1}}$ it is fully inward (Figure 5.4). Centripetal forces are dominant at this position. The exit's radial inflow at the bottom of the step along the stator (between $\mathrm{I_E}$ and $\mathrm{D_E}$) is twice as fast as the radial outflow along the rotor (Figure 5.4), it is beginning to resemble rotationally-dominated torsional Couette flow that is present along $\mathrm{D_E}$ (Figure 5.8). However, the bulk fluid is still moving outwards away from the center. If we section all positions at and around the inlet, the sum of the fluid profiles will be one that is moving away from the center of the disk (Figure 5.5). The geometry and position of the inlet(s) plays a significant role in the flow profiles at the entrance. A second inlet expelling fluid in proximity of the first eliminates any

PFR behaviour otherwise found in rs-SDRs and leaves only rotation-governed flow profiles (Figure 5.5).

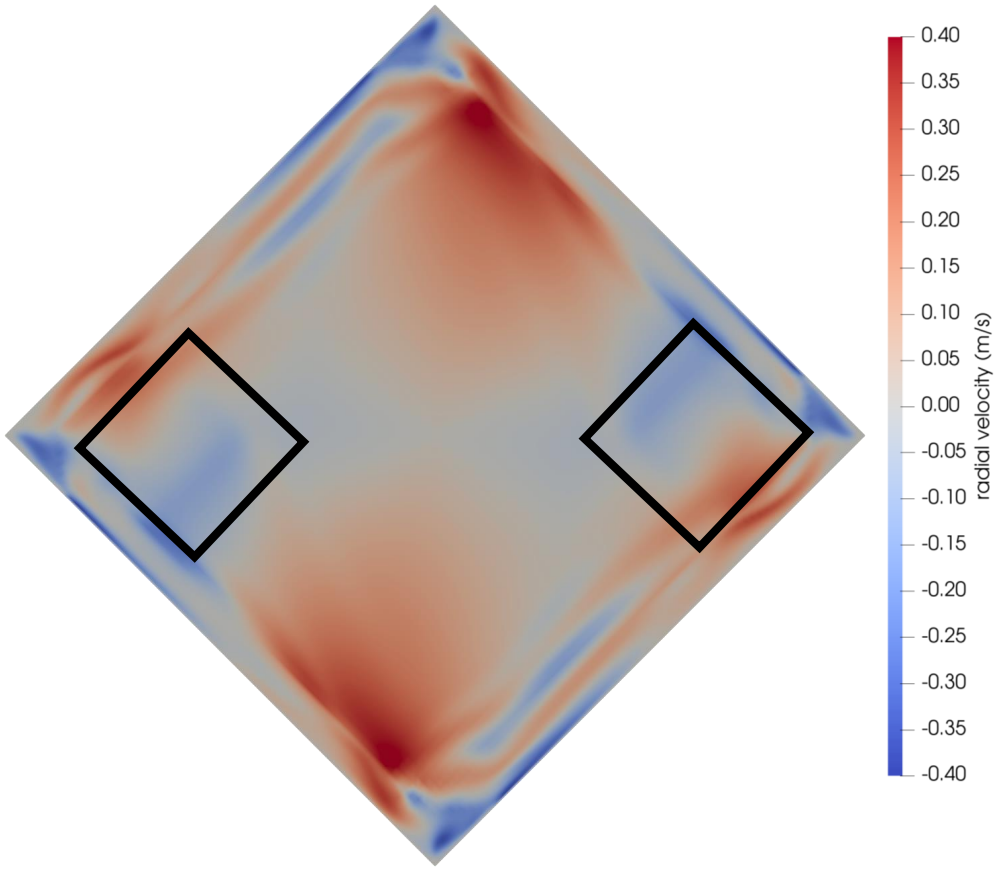

Figure (5.5) Top view of the radial velocity of the entrance region. The two inlets are on opposing sides along the horizontal plane. The black squares indicate the approximate location of the inlets. There are clear radial inflows and outflows even near the center of the disk.

Critical Mixing Radius

We simulated the injection of two tracers at $60\,\mathrm{mL\,min^{-1}}$ for rotational speeds of $38\,\mathrm{rad\,s^{-1}}$, $79\,\mathrm{rad\,s^{-1}}$, and $157\,\mathrm{rad\,s^{-1}}$ to elucidate the macro-mixing behaviour. We denoted two mixing states, 99 % and 95 %, with respect to the concentration of the tracers (with absolute values of 1 and -1). Regions of 99 % mixing represent tracer values of $\pm$ 0.01 or lower and regions of 95 % mixing represent tracer values of $\pm$ 0.05 or lower (Figure 5.7). We define the term, r_{crit}, as the threshold radius required for the two tracers to cross to be considered mixed. At 99 % mixing, as ω increases the radial distance the fluids need to travel decreases from 25 mm at $38\,\mathrm{rad\,s^{-1}}$ to 17 mm at $157\,\mathrm{rad\,s^{-1}}$ as it begins to plateau (Figure 5.6). At 95 %, the

distance decreases from 19 mm to 10 mm. Moreover, at 38 rad s^{-1} and 79 rad s^{-1} a uniform concentration of both tracers is never attained (Figure 5.7), but mixing remains sufficient for nanoprecipitation. Even on the macro-scale, the mixing time is still far below the residence time (2 s to 0.3 s compared to the lowest residence time in the disk at 4.5 s). Thus, much higher flow rates are permissible without compromising the nanoprecipitation process in rs-SDRs. For example, at a flow rate of 600 mL min^{-1} the residence time remains above the bulk mixing at 157 rad s^{-1} (0.9 s vs. 0.88 s). At a polymer concentration of 15 mg mL^{-1} in the polymer solution and a polymer:aqueous volumetric feed input of 1:3, the production rate of NPs reaches 4 kg d^{-1} — far above clinical and industry requirements. Furthermore, from a design perspective for nanoprecipitation, once the fluids are fully mixed, any volume afterwards is unnecessary and could be removed to increase production.

5.5.2 Time-Averaged Velocities

The time-averaged radial velocities at $0.4r_{\mathrm{D}}$, $0.6r_{\mathrm{D}}$, and $0.8r_{\mathrm{D}}$ all exhibit torsional Couette/rotation-governed flow at different magnitudes [144], with a peak velocity at $0.8r_{\mathrm{D}}$ of 0.65 m s^{-1} in the Von Kármán layer flowing outwards and 0.35 m s^{-1} in the Bödewadt layer flowing inwards (Figure 5.8). This flow pattern is also consistent across rotational speeds but the magnitudes in the boundary layers are less than half for 79 rad s^{-1} and approximately one-tenth for 38 rad s^{-1}. In addition, this behaviour is mirrored in the bottom region of the geometry towards the outlet ($\mathrm{D_O}$). Overall, as there is no transition from PFR-like to CSTR-like flow behaviour, this rs-SDR geometry behaves entirely like a CSTR at all rotational speeds (38 rad s^{-1} to 157 rad s^{-1}). However, Hop et al. [156] found that at 10 rad s^{-1}, and thus in laminar flow, there was no radial inward flow — the flow field behaved as a PFR. At 75 rad s^{-1}, they observed PFR and CSTR flow behaviour. In our case, PFR behavior was entirely absent likely due to the nature of the inlet.

As for the time-averaged azimuthal velocities, the simulation at 38 rad s^{-1} belongs to flow regime I — a laminar torsional Couette flow with the tangential velocity varying linearly from the wall to the disk (Figure 5.9) [143]. Otherwise, the simulations at 79 rad s^{-1} and 157 rad s^{-1} belong in flow regime III — turbulent torsional Couette — and the flows behave as such (Figures 2.7, 2.8) as the velocity is zero only at the stator and then increases as we get closer to the disk (Figure 5.9); a profile of rotation-governed flow [144]. This velocity profile is also mirrored at $\mathrm{D_O}$.

In the region at the rim of the disk where the fluid will traverse from the top of the disk to the bottom (shaded area in Figure 5.1), the time-averaged velocity profile consists of pockets of upward and downward velocities (i.e., toroidal vortices in classic Taylor-Couette flow [283])

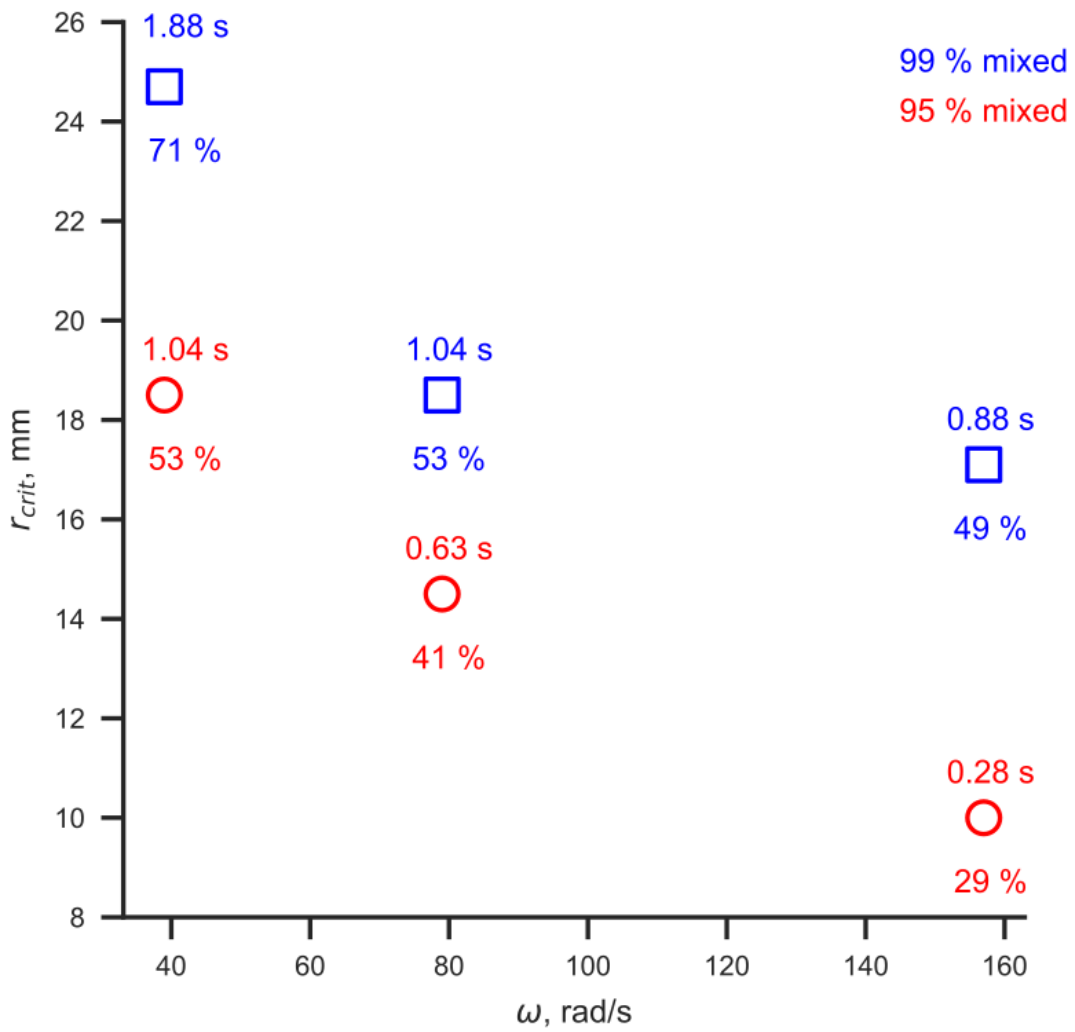

Figure (5.6) Time and distance across the disk's radius required to achieve 99 % (squares) and 95 % (circles) mixing. The percentage underneath the markers represent the fraction of the disk's radius necessary to achieve indicated mixing.

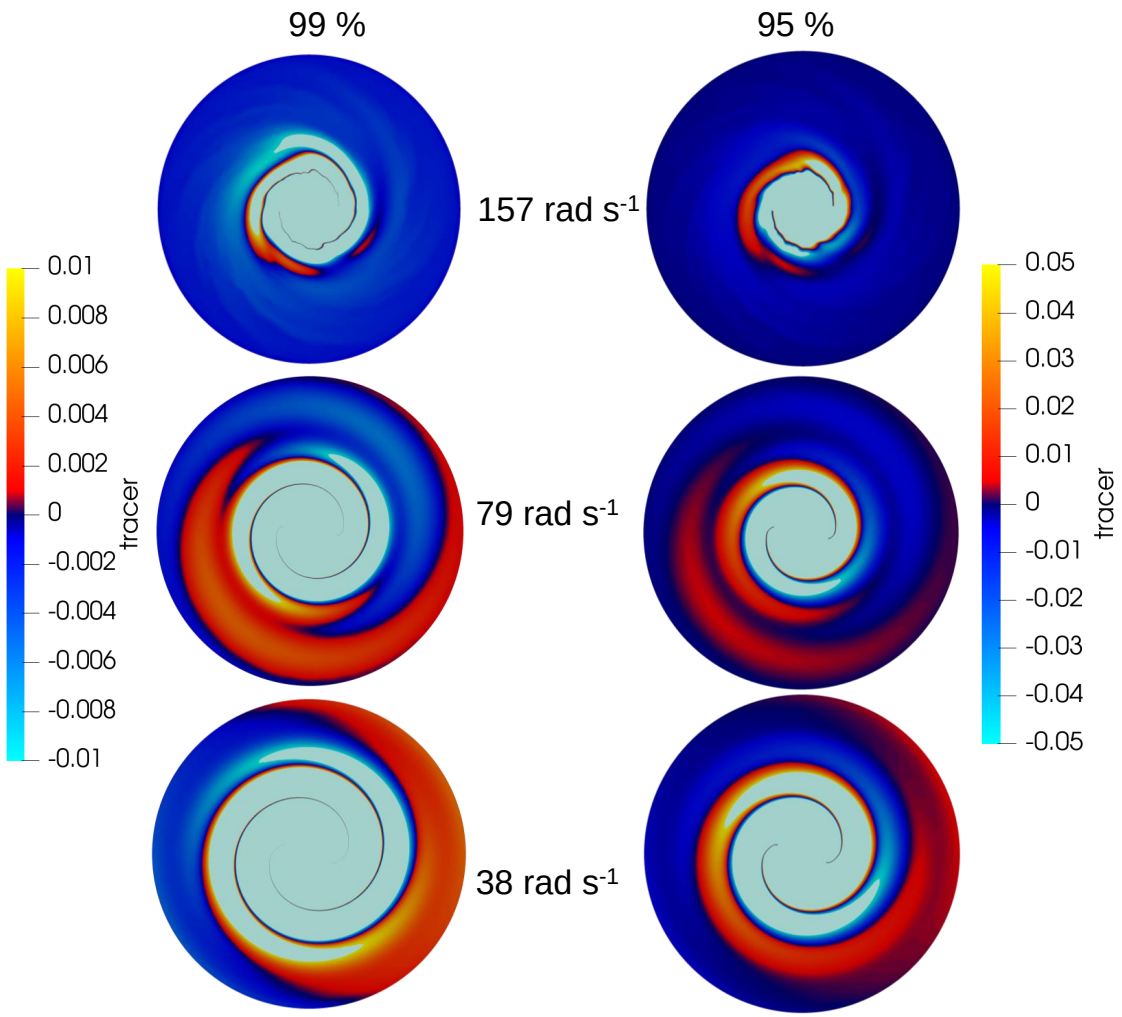

Figure (5.7) Visual depiction of tracers mixing and critical radii for 99 % and 95 % mixing. The center (turquoise) are areas of mixing inferior to 99 % and 95 %. The critical radius is the distance from the center of the disk to the intersection point between non-mixed and fully mixed. The scales indicate the concentration gradients for the tracers.

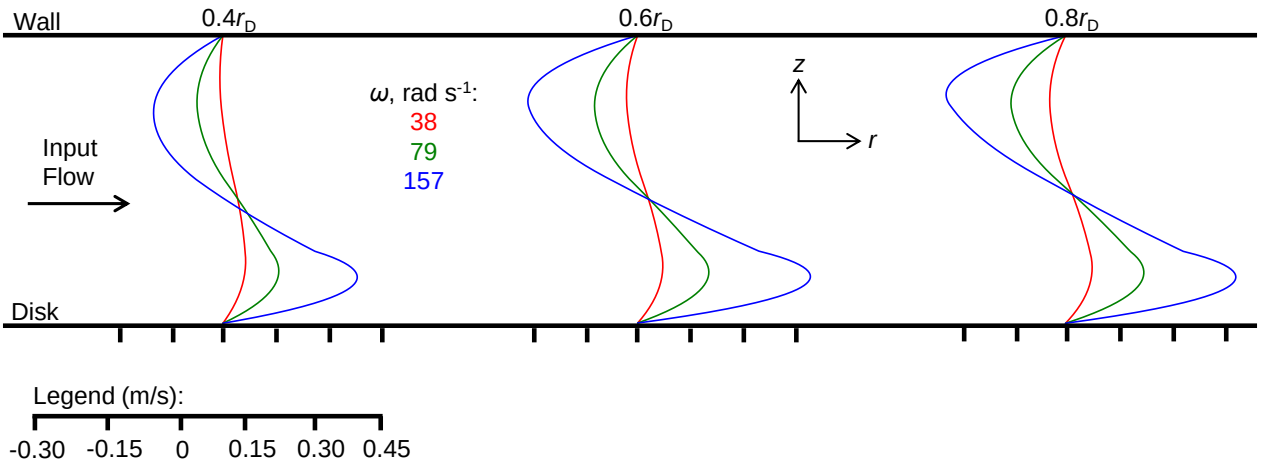

Figure (5.8) Time-averaged radial velocity profiles for rotational speeds of $38\,\mathrm{rad\,s^{-1}}$ to $157\,\mathrm{rad\,s^{-1}}$ at $0.4r_\mathrm{D}$, $0.6r_\mathrm{D}$, and $0.8r_\mathrm{D}$.

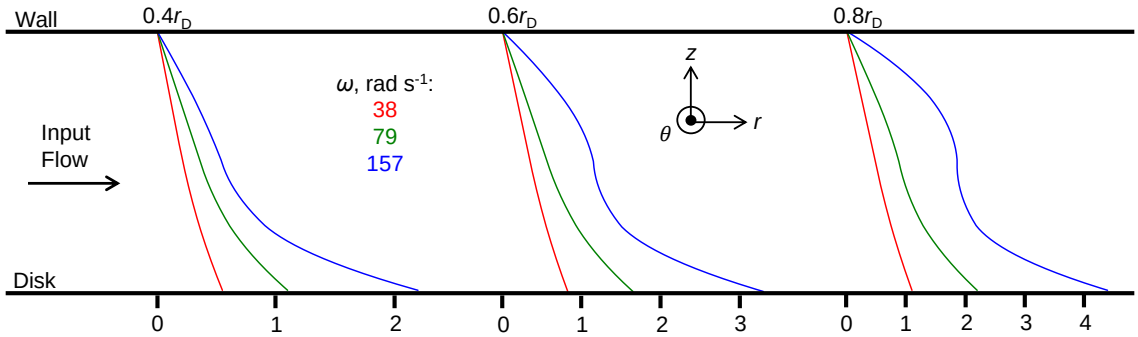

Figure (5.9) Time-averaged azimuthal velocity profiles for rotational speeds of $38\,\mathrm{rad\,s^{-1}}$ to $157\,\mathrm{rad\,s^{-1}}$ at $0.4r_\mathrm{D}$, $0.6r_\mathrm{D}$, and $0.8r_\mathrm{D}$.

whose magnitude is related to the rotational speed to a maximum of $0.5\,\mathrm{m\,s^{-1}}$ at $157\,\mathrm{rad\,s^{-1}}$ (Figure 5.10).

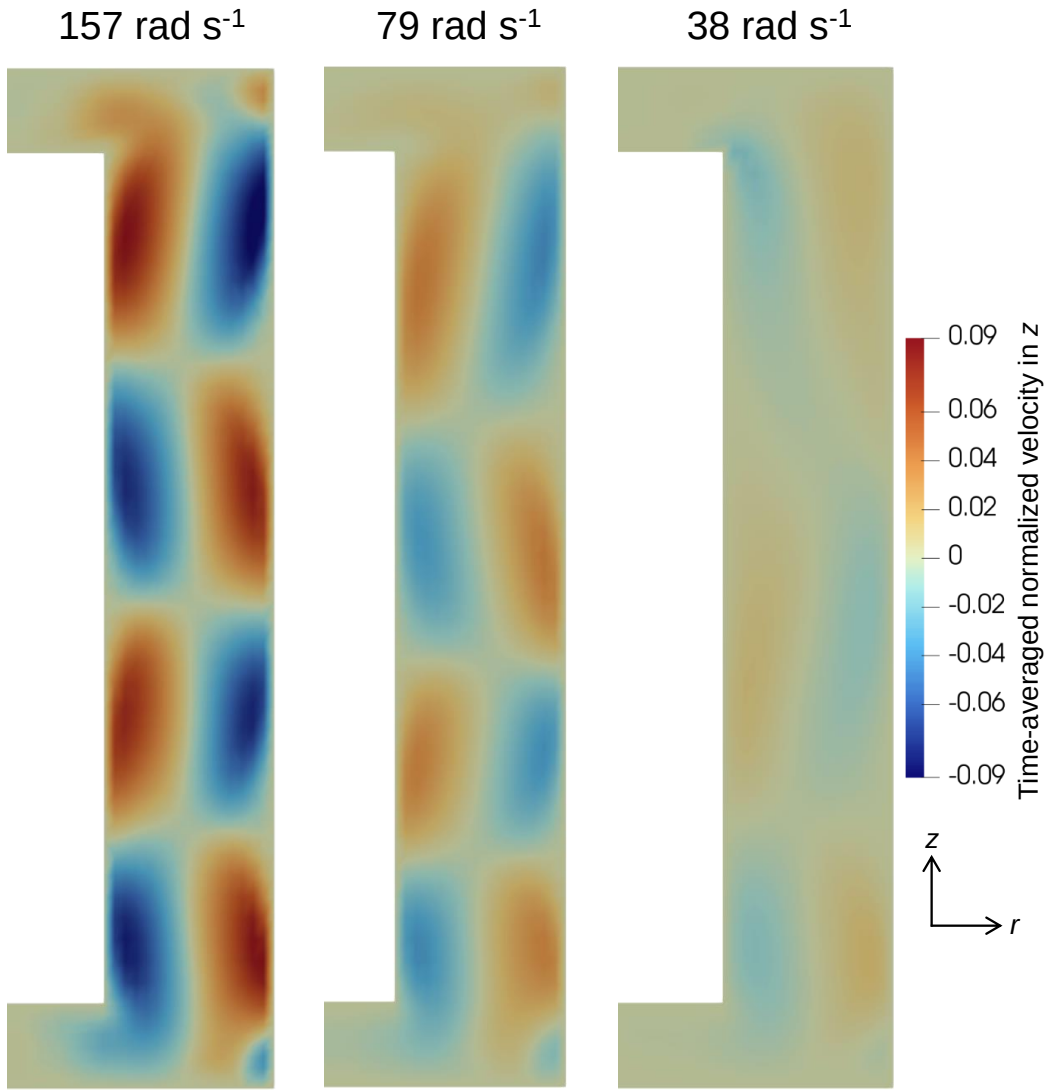

Figure (5.10) Normalized (velocities divided by ωr_{D}) time-averaged velocities in z.

The flow in an rs-SDR with inlets expelling fluid into the same region leads to pure CSTR/rotation-governed flow behaviours. The turbulent nature of the flow is conducive to nanoprecipitation. Moreover, the impinging jet behaviour at the inlet is also a feature that enables nanoprecipitation. We have demonstrated the synthesis of NPs in an rs-SDR upon which the model presented here is based on. Higher rotational speeds lead to smaller NPs (as low as 58 nm at $314\,\mathrm{rad\,s^{-1}}$ compared to 74 nm at $157\,\mathrm{rad\,s^{-1}}$). The rotational speed was the strongest

predictor of particle size followed by concentration of polymer in the organic phase. Drug loading was also successful at a similar performance to other techniques.

5.6 Conclusion

We have simulated the hydrodynamics (flow, tracer mixing) with `Lethe` in a one disk rs-SDR modeled after FlowID's R2 reactor. The flow profiles along the disk radius are consistent with the literature — radial inflows at the stator boundary layer and radial outflows at the rotor boundary layer. There was no transition radius, the flow was purely rotation-governed as a result of the inlets expelling fluid into the same area. At $157\,\mathrm{rad\,s^{-1}}$, the flows at the inlet are drawn toward the center and collide with each other, in a similar fashion to impinging jets, before being ejected outwards. Bulk mixing occurs in the millisecond range at $157\,\mathrm{rad\,s^{-1}}$. It is possible that bulk mixing can occur in the microsecond range at the operational limits of these reactors (e.g. FlowID's R2 can operate at $600\,\mathrm{rad\,s^{-1}}$). Future work at higher rotational velocities (to predict behaviours in commercial reactors), varying flow rates and inlet geometries is necessary to inform further design decisions. Rs-SDRs could be tailored to specific processes; for nanoprecipitation, mixing times and volume requirements could be reduced and thus create a more intensified process (increased production rates while simultaneously minimizing the size of the reactor).

CHAPTER 6 DISCUSSION

PLA is a biocompatible and biodegradable polymer with applications in drug delivery. We ROPed D,L-lactide to produce PLA in a microwave reactor with toluene and THF. The MWs in toluene and THF peaked at 31 kDa after 1 h and 11 kDa after 4 h, respectively. The $Đ$s ranged from 1.1 (THF) to 1.5 (toluene), which is lower than many reported values in the literature with $Sn(Oct)_2$ as a catalyst. THF's innate water content lowers the molecular weight of PLA as it cleaves PLA chains. Moreover, we did not anticipate the difficulty associated with removing toluene and THF from PLA after synthesis. Despite dissolving and precipitating PLA multiple times, ^{1}H NMR still detected THF and toluene. Even heating PLA in a furnace for 24 h at the boiling points of toluene and THF after synthesis was insufficient to remove them. Bulk polymerization would allow for a solventless reaction and thus remove sources of impurities in the final production, however, in Anton Parr's Monowave 400 microwave reactor D,L-lactide solidifies and beings to degrade after a few min. This may be because lactide is rapidly polymerizing and thus the viscosity becomes too great for the stirrer to function. Volume of solvent required to enable lengthy polymerizations while minimizing impurities would have been an interesting parameter for the design of experiments. Furthermore, we were unable to isolate the influence of the dielectric properties of solvents on the polymerization of D,L-lactide. Solvents that interact well with microwaves often have OH groups — too many of these hinders the polymerization. Furthermore, the high dielectric loss solvents without OH groups (e.g., DMF, DMSO) were also unsuitable as a result of solubility issues. Perhaps, we would have been better to polymerize D,L-lactide with solid polar elements with varying dielectric loss properties. Finally, the dielectric properties of D,L-lactide were measured in powder form at room temperature. However, these properties change as a function of temperature and the presence of air within the powder potentially hindered the readings.

The majority of current technologies are unable to produce drug-loaded NPs on a scale sufficiently large for clinical trials or industry. We are the first to produce uniform ($Đ < 0.2$) NPs with sizes suitable for drug delivery (58 nm to 132 nm) at rates up to $0.8\,\mathrm{kg\,d^{-1}}$ in a rs-SDR. The DLC model adequately predicts ($R^2 = 0.89$) the particle size in the slow mixing regime. Concentration and the disk's rotational speed are the dominating factors that determine particle size and $Đ$. Nevertheless, we could not test rotational speeds below $157\,\mathrm{rad\,s^{-1}}$ due to the manufacturer's guidelines. In addition, the pronounced backflow at elevated rotational speed ($500\,\mathrm{rad\,s^{-1}}$) compromised the continuous experiments and thus, only operation between $157\,\mathrm{rad\,s^{-1}}$ to $314\,\mathrm{rad\,s^{-1}}$ was possible. In fact, even at $314\,\mathrm{rad\,s^{-1}}$,

at concentrations of PLA in acetone of $10\,\mathrm{mg\,mL^{-1}}$ and above, the reactor would clog. Only PLA and PLA-PEG with ibuprofen were tested for the nanoprecipitation and drug loading; lipids, and other molecules and drugs were not tested.

We also simulated mixing and the time-averaged velocity flow profiles in the rs-SDR to elucidate its ability to produce suitable drug-loaded NPs. Large eddy simulations with `Lethe` captured the flow and bulk mixing profiles at $38\,\mathrm{rad\,s^{-1}}$ to $157\,\mathrm{rad\,s^{-1}}$, a C_w of 29 and a G of 0.014. The disk is entirely rotation-governed; radial outflows in the Von Kármán layer and radial inflows in the Bödewadt layer. The geometry of the inlet determines the presence of throughflow-governed flow profiles. Macro-mixing was simulated by injecting two tracers of opposite signs and determining the critical mixing radius. It decreases with increasing rotational speed. Although it is well understood that mixing/impact between a polymer containing organic phase and an aqueous phase produces nanoparticles (nanoprecipitation), it was encouraging to see such a low dispersity (< 0.2) with the rs-SDR. This is also in spite of the backflows, which could recirculate PLA particles into areas with a higher concentration of acetone and risk re-solubilization. In addition, the impinging jet behaviour at the entrance of the reactor and the absence of throughflow-governed flow was a surprise. We also suspect that this behaviour is a contributing factor for nanoprecipitation in the rs-SDR. This would strengthen our observation that the flowrate ratio had little impact on the properties of the NPs. In other technologies, like microfluidics, the flowrate ratio is a principal factor. In fact, keeping other parameters constant a decrease in the flowrate ratio between the organic and aqueous phase actually decreases the size and $Đ$ of the NPs. In the rs-SDR, we saw the opposite effect but its influence was not as pronounced as with the rotational speed and concentration of PLA in acetone. The biggest surprise was the hydrodynamics at the inlet of the rs-SDR. The majority, if not all of the literature on rs-SDR hydrodynamics show PFR-dominant behaviour near the inlets that then transitions to CSTR-dominant. However, in our simulations, there was no evidence for this PFR behaviour — the flow was CSTR governed. Our geometry (Figure 6.1, left) differs from that of the literature in that the inlets are not separated by any physical entity. The fluids enter the reactor in proximity to each other and thus begin interacting almost immediately. It may also be that this PFR behaviour is only present in the idealized reactor geometries in the literature. Despite the novelty, the simulated flows occurred at a single viscosity. Multiple fluids with varying viscosities would have painted more realistic fluid profiles and bulk mixing behaviours. The two injected tracers had the same diffusivity; varying diffusivities is required to better assess the simulation's robustness and to properly characterize the mixing hydrodynamics of a system like that of water, acetone, and PLA. Also, the mesh geometry was a simplified version of the actual reactor (Figure 6.1). Finally, the hydrodynamic study was not validated with experimental

observations in the actual reactor.

Figure (6.1) 2D slice of the simulated geometry (left), 2D slice of the actual reactor geometry (right). The arc in the center represents a pill-shaped magnet that couples with the magentic motor of the rs-SDR.

CHAPTER 7 CONCLUSION

PLA is integral to the development of nano-sized drug delivery systems. These systems will be crucial for alleviating drug shortages while simultaneously improving patient outcomes and decreasing side-effects. However, the synthesis of PLA and drug-delivery systems is not at a level to satisfy industry requirements. Here we present alternative technologies (microwave and rs-SDRs) with the aim of increasing the pool of knowledge required to push production to larger scales.

1. Microwaves as a heating medium reduce polymerization times of D,L-lactide compared to traditional heating methods. The catalyst and initiator were $Sn(Oct)_2$ and BnOH, respectively. The solvent influenced the final MW of PLA with those synthesized in toluene being 2 to 3 times higher than those synthesized in THF. This is likely due to the presence of water in THF and other physical properties that have yet to be identified in the literature. In addition, the majority of solvents that readily interact with microwaves are unfit for ROP of D,L-lactide as the presence of too many OH groups hinders the reaction. Furthermore, we developed a statistical power-law model that predicts MW as a function of experimental parameters.

2. A lab scale rs-SDR from FlowID (the R2) continuously produced PLA (and PLA-PEG) NPs at rates up to $0.8\,\mathrm{kg\,d^{-1}}$, which satisfies large-scale clinical trial requirements. The NPs $Đ$ ranged from 0.1 to 0.2 and their sizes between 58 nm to 132 nm and fit the DLC model ($R^2 = 0.89$). The concentration of polymer in the organic phase and the rotation of the disk determined the size of the nanoparticles. In addition, the rs-SDR successfully loaded ibuprofen into PLA and PLA-PEG. Futhermore, the pilot scale rs-SDR (the R3) could potentially produce nanoparticles at rates up to $50\,\mathrm{kg\,d^{-1}}$, far outperforming any other available technology and satisfying industry requirements.

3. `Lethe` simulated the hydrodynamics (flow, bulk mixing) in an rs-SDR geometry modeled after the first disk of FlowID's R2 reactor. Bulk mixing of two tracers occurs in less than 1 s at $157\,\mathrm{rad\,s^{-1}}$ and up to 2 s at $39\,\mathrm{rad\,s^{-1}}$. Radial inflows are present in the Bödewadt layer and radial outflows in the Von Kármán layer — a commonality with the literature. However, there was no transition radius that demarked a flow transformation from throughflow-governed (PFR) to rotation-governed (CSTR). The inlet geometry dictates the existence of the transitions radius. At $157\,\mathrm{rad\,s^{-1}}$, the flows enter the reactor and collide with each other before being pushed outwards.

It seems that the technologies to produce these nano-sized drug delivery systems already exist. It is now a matter of leveraging the knowledge, and applying it on larger scales. And, of course, ensuring the safety of these systems in the human body.

7.1 Future Research

The main goal of this project was to intensify the production of drug carriers starting from the synthesis of the polymer. It has taken steps in the right direction, however, there is still much to be done. As such, future research should focus on:

1. A screening DoE to determine what physical properties of solvents influence the polymerization of lactide. Anhydrous THF still produced lower MW PLAs compared to toluene despite the absence of water; information regarding this is absent in the literature. This suggests other factors are at play that we could potentially leverage.

2. Alternatively, introduce solid polar elements and microwaves into a continuous setup for the polymerization of lactides with no solvent. This would maintain the positive effects of microwave heating on the polymerization while removing the issues surrounding solvents (impurities, purification, physical properties) and reduce the environmental footprint of the reaction.

3. Investigate lower rotational speeds ($1\,\mathrm{rad\,s^{-1}}$ to $157\,\mathrm{rad\,s^{-1}}$) to determine the minimum rotation required to produce monodisperse NPs with adequate sizes. This is crucial because as the reactors scale in size, the speed at which the disks can rotate decreases. For example, FlowID's lab-scale R2 reactor can rotate up to $630\,\mathrm{rad\,s^{-1}}$, while the pilot scale R3 (which is 10-15x larger in terms of volume) can only rotate up to $314\,\mathrm{rad\,s^{-1}}$. In addition, higher rotational speeds induce stronger backflows which, as we have demonstrated in this work, hinders the nanoprecipitation. Furthermore, at $314\,\mathrm{rad\,s^{-1}}$, we were already approaching the lower limit for acceptable NP size (50 nm). Energy expenditures are minimized by operating at the lowest possible rotational speed, which is important as processes scale-up.

4. The simulation results show that the shortly after the fluids enter the inlets they collide in the manner of an impinging jet. We suspect that this a contributing factor to the rs-SDR's ability to produce monodisperse NPs despite the backflow and re-circulation that occurs further along the disk. This flow behaviour and the critical mixing radius must be substantiated, experimentally. For example, by replacing the top of the reactor with a transparent cover, we would be able to image the flow and macromixing patterns

with a colorimetric method (e.g., with a fast acid-base indicator reaction as outlined in [290]) and a high-speed camera.

5. Scale-up with rs-SDRs to a commercial size will necessitate an understanding of the local hydrodynamics. For example, G is an important parameter that will vary to accommodate higher throughputs and larger volumes. A hydrodynamic study examining the relationship between G, r_{D}, inlet geometry, and even inlet placement will ensure a more successful scale-up for nanoprecipitation.

REFERENCES

[1] J. K. Aronson, C. Heneghan, and R. E. Ferner, “Drug shortages. part 2: Trends, causes and solutions,” *British Journal of Clinical Pharmacology*, vol. 89, no. 10, pp. 2957–2963, 2023. [Online]. Available: http://dx.doi.org/10.1111/bcp.15853

[2] C. LYNCH, “Medical department of the japanese army,” *The Boston Medical and Surgical Journal*, vol. 155, no. 3, pp. 51–57, 1906. [Online]. Available: http://dx.doi.org/10.1056/NEJM190607191550301

[3] K. H. Coward, E. W. Kassner, and L. W. Waller, “Shortage of calcium in the "poorer-class" diet,” *BMJ*, vol. 1, no. 4018, pp. 59–64, 1938. [Online]. Available: http://dx.doi.org/10.1136/bmj.1.4018.59

[4] S. Shukar, F. Zahoor, K. Hayat, A. Saeed, A. H. Gillani, S. Omer, S. Hu, Z.-U.-D. Babar, Y. Fang, and C. Yang, “Drug shortage: Causes, impact, and mitigation strategies,” *Frontiers in Pharmacology*, vol. 12, no. nil, p. nil, 2021. [Online]. Available: http://dx.doi.org/10.3389/fphar.2021.693426

[5] M. P. Socal and J. M. Sharfstein, “Drug shortages-a study in complexity,” *JAMA Network Open*, vol. 7, no. 4, p. e244168, 2024. [Online]. Available: http://dx.doi.org/10.1001/jamanetworkopen.2024.4168

[6] US Food and Drug Administration, “Drug shortages: Root causes and potential solutions,” https://www.fda.gov/media/131130/download, 2019.

[7] US Government Accountability Office, “Drug shortages: Public health threat continues, despite efforts to help ensure product availability,” https://www.gao.gov/products/gao-14-194, 2014.

[8] K. C. Kim, S. D. Rothenberger, M. Tadrous, I. Hernandez, W. F. Gellad, J. W. Devine, T. B. Hershey, L. M. Maillart, and K. J. Suda, “Drug shortages prior to and during the covid-19 pandemic,” *JAMA Network Open*, vol. 7, no. 4, p. e244246, 2024. [Online]. Available: http://dx.doi.org/10.1001/jamanetworkopen.2024.4246

[9] R. James, O. S. Manoukian, and S. G. Kumbar, “Poly(lactic acid) for delivery of bioactive macromolecules,” *Advanced Drug Delivery Reviews*, vol. 107, no. nil, pp. 277–288, 2016. [Online]. Available: http://dx.doi.org/10.1016/j.addr.2016.06.009

[10] P. Singla, R. Mehta, and S. Upadhyay, "Microwave assisted in situ ring-opening polymerization of polylactide/clay nanocomposites: Effect of clay loading," *Applied Clay Science*, vol. 95, no. nil, pp. 67–73, 2014. [Online]. Available: http://dx.doi.org/10.1016/j.clay.2014.03.012

[11] J.-M. Lim, A. Swami, L. M. Gilson, S. Chopra, S. Choi, J. Wu, R. Langer, R. Karnik, and O. C. Farokhzad, "Ultra-high throughput synthesis of nanoparticles with homogeneous size distribution using a coaxial turbulent jet mixer," *ACS Nano*, vol. 8, no. 6, pp. 6056–6065, 2014. [Online]. Available: http://dx.doi.org/10.1021/nn501371n

[12] D. Garlotta, "A literature review of poly(lactic) acid," *Journal of Polymers and the Environment*, vol. 9, no. 2, pp. 63–84, 2001. [Online]. Available: http://dx.doi.org/10.1023/A:1020200822435

[13] T. Casalini, F. Rossi, A. Castrovinci, and G. Perale, "A perspective on polylactic acid-based polymers use for nanoparticles synthesis and applications," *Frontiers in Bioengineering and Biotechnology*, vol. 7, no. nil, p. nil, 2019. [Online]. Available: http://dx.doi.org/10.3389/fbioe.2019.00259

[14] N. Amreddy, A. Babu, A. Munshi, and R. Ramesh, *Poly(α-hydroxy acid)-Based Nanoparticles for Drug/Gene Delivery for Cancer Therapy*, ser. Polymeric Nanoparticles as a Promising Tool for Anti-cancer Therapeutics. Elsevier, 2019, pp. 81–99. [Online]. Available: http://dx.doi.org/10.1016/B978-0-12-816963-6.00005-4

[15] Y. Cheng, S. Deng, P. Chen, and R. Ruan, "Polylactic acid (PLA) synthesis and modifications: a review," *Frontiers of Chemistry in China*, vol. 4, no. 3, pp. 259–264, 2009. [Online]. Available: http://dx.doi.org/10.1007/s11458-009-0092-x

[16] S. Corneillie and M. Smet, "PLA architectures: the role of branching," *Polymer Chemistry*, vol. 6, no. 6, pp. 850–867, 2015. [Online]. Available: http://dx.doi.org/10.1039/C4PY01572J

[17] R. Donate, M. Monzón, M. E. Alemán-Domínguez, and Z. Ortega, "Enzymatic degradation study of PLA-based composite scaffolds," *REVIEWS ON ADVANCED MATERIALS SCIENCE*, vol. 59, no. 1, pp. 170–175, 2020. [Online]. Available: http://dx.doi.org/10.1515/rams-2020-0005

[18] M. Puthumana, P. S. G. Krishnan, and S. K. Nayak, "Chemical modifications of PLA through copolymerization," *International Journal of Polymer Analysis*

and Characterization, vol. 25, no. 8, pp. 634–648, 2020. [Online]. Available: http://dx.doi.org/10.1080/1023666X.2020.1830650

[19] R. Gref, M. Lück, P. Quellec, M. Marchand, E. Dellacherie, S. Harnisch, T. Blunk, and R. Müller, "'Stealth' corona-core nanoparticles surface modified by polyethylene glycol (PEG): Influences of the corona (PEG chain length and surface density) and of the core composition on phagocytic uptake and plasma protein adsorption," *Colloids and Surfaces B: Biointerfaces*, vol. 18, no. 3-4, pp. 301–313, 2000. [Online]. Available: http://dx.doi.org/10.1016/S0927-7765(99)00156-3

[20] A. Zhu, P. Lu, and H. Wu, "Immobilization of poly(ϵ-caprolactone)-poly(ethylene oxide)-poly(ϵ-caprolactone) triblock copolymer on poly(lactide-co-glycolide) surface and dual biofunctional effects," *Applied Surface Science*, vol. 253, no. 6, pp. 3247–3253, 2007. [Online]. Available: http://dx.doi.org/10.1016/j.apsusc.2006.07.036

[21] D. R. Perinelli, M. Cespi, G. Bonacucina, and G. F. Palmieri, "Pegylated polylactide (PLA) and poly (lactic-co-glycolic acid) (PLGA) copolymers for the design of drug delivery systems," *Journal of Pharmaceutical Investigation*, vol. 49, no. 4, pp. 443–458, 2019. [Online]. Available: http://dx.doi.org/10.1007/s40005-019-00442-2

[22] K. Zhang, X. Tang, J. Zhang, W. Lu, X. Lin, Y. Zhang, B. Tian, H. Yang, and H. He, "PEG-PLGA copolymers: Their structure and structure-influenced drug delivery applications," *Journal of Controlled Release*, vol. 183, no. nil, pp. 77–86, 2014. [Online]. Available: http://dx.doi.org/10.1016/j.jconrel.2014.03.026

[23] A. Ignatius and L. Claes, "In vitro biocompatibility of bioresorbable polymers: poly(L, DL-Lactide) and poly(L-lactide-co-glycolide)," *Biomaterials*, vol. 17, no. 8, pp. 831–839, 1996. [Online]. Available: http://dx.doi.org/10.1016/0142-9612(96)81421-9

[24] D. Pandita, S. Kumar, and V. Lather, "Hybrid poly(lactic-co-glycolic acid) nanoparticles: Design and delivery prospectives," *Drug Discovery Today*, vol. 20, no. 1, pp. 95–104, 2015. [Online]. Available: http://dx.doi.org/10.1016/j.drudis.2014.09.018

[25] S. Rezvantalab, N. I. Drude, M. K. Moraveji, N. Güvener, E. K. Koons, Y. Shi, T. Lammers, and F. Kiessling, "PLGA-based nanoparticles in cancer treatment," *Frontiers in Pharmacology*, vol. 9, no. nil, p. nil, 2018. [Online]. Available: http://dx.doi.org/10.3389/fphar.2018.01260

[26] Y. Zheng, B. Yu, W. Weecharangsan, L. Piao, M. Darby, Y. Mao, R. Koynova, X. Yang, H. Li, S. Xu, L. J. Lee, Y. Sugimoto, R. W. Brueggemeier, and

R. J. Lee, "Transferrin-conjugated lipid-coated PLGA nanoparticles for targeted delivery of aromatase inhibitor 7α-APTADD to breast cancer cells," *International Journal of Pharmaceutics*, vol. 390, no. 2, pp. 234–241, 2010. [Online]. Available: http://dx.doi.org/10.1016/j.ijpharm.2010.02.008

[27] Y. Xu, C. Kim, D. M. Saylor, and D. Koo, "Polymer degradation and drug delivery in PLGA-based drug-polymer applications: a review of experiments and theories," *Journal of Biomedical Materials Research Part B: Applied Biomaterials*, vol. 105, no. 6, pp. 1692–1716, 2016. [Online]. Available: http://dx.doi.org/10.1002/jbm.b.33648

[28] H. R. Kricheldorf and S. M. Weidner, "Polymerization of L-Lactide with $SnCl_2$: a Low Toxic and Eco-Friendly Catalyst," *Journal of Polymers and the Environment*, vol. 29, no. 8, pp. 2504–2516, 2021. [Online]. Available: http://dx.doi.org/10.1007/s10924-020-02042-w

[29] A. Kowalski, A. Duda, and S. Penczek, "Kinetics and Mechanism of Cyclic Esters Polymerization Initiated With Tin(II) Octoate. 3. Polymerization of L,L-dilactide," *Macromolecules*, vol. 33, no. 20, pp. 7359–7370, 2000. [Online]. Available: http://dx.doi.org/10.1021/ma000125o

[30] S. J. Moravek, "Synthesis, Propagation Kinetics, and Characterization of D,L-Lactide-Based Polyols and Polyurethanes Therefrom," Ph.D. dissertation, Hattiesburg, MS, 2008.

[31] Y. M. Harshe, G. Storti, M. Morbidelli, S. Gelosa, and D. Moscatelli, "Polycondensation Kinetics of Lactic Acid," *Macromolecular Reaction Engineering*, vol. 1, no. 6, pp. 611–621, 2007. [Online]. Available: http://dx.doi.org/10.1002/mren.200700019

[32] E. Thostenson and T.-W. Chou, "Microwave processing: fundamentals and applications," *Composites Part A: Applied Science and Manufacturing*, vol. 30, no. 9, pp. 1055–1071, 1999. [Online]. Available: http://dx.doi.org/10.1016/S1359-835X(99)00020-2

[33] D. C. Boffito and D. F. Rivas, "Process intensification connects scales and disciplines towards sustainability," *The Canadian Journal of Chemical Engineering*, vol. 98, no. 12, pp. 2489–2506, 2020. [Online]. Available: http://dx.doi.org/10.1002/cjce.23871

[34] J. Chaouki, S. Farag, M. Attia, and J. Doucet, "The development of industrial (thermal) processes in the context of sustainability: the case for microwave heating,"

The Canadian Journal of Chemical Engineering, vol. 98, no. 4, pp. 832–847, 2020. [Online]. Available: http://dx.doi.org/10.1002/cjce.23710

[35] C. Kappe, *Microwave-Assisted Chemistry*, ser. Comprehensive Medicinal Chemistry II. Elsevier, 2007, pp. 837–860. [Online]. Available: http://dx.doi.org/10.1016/B0-08-045044-X/00109-7

[36] S. S. Bukhari, J. Behin, H. Kazemian, and S. Rohani, "Synthesis of zeolite NA-A using single mode microwave irradiation at atmospheric pressure: The effect of microwave power," *The Canadian Journal of Chemical Engineering*, vol. 93, no. 6, pp. 1081–1090, 2015. [Online]. Available: http://dx.doi.org/10.1002/cjce.22194

[37] J. Anwar, U. Shafique, W. uz Zaman, R. Rehman, M. Salman, A. Dar, J. M. Anzano, U. Ashraf, and S. Ashraf, "Microwave chemistry: Effect of ions on dielectric heating in microwave ovens," *Arabian Journal of Chemistry*, vol. 8, no. 1, pp. 100–104, 2015. [Online]. Available: http://dx.doi.org/10.1016/j.arabjc.2011.01.014

[38] C. O. Kappe, A. Stadler, and D. Dallinger, *Microwaves in organic and medicinal chemistry*. John Wiley & Sons, 2012, vol. 52.

[39] A. Metaxas, "Foundations of electroheat. A unified approach," *Fuel and Energy Abstracts*, vol. 37, no. 3, p. 193, 1996. [Online]. Available: http://dx.doi.org/10.1016/0140-6701(96)88691-7

[40] J. M. Hill and T. R. Marchant, "Modelling microwave heating," *Applied Mathematical Modelling*, vol. 20, no. 1, pp. 3–15, 1996. [Online]. Available: http://dx.doi.org/10.1016/0307-904X(95)00107-U

[41] C. Gabriel, S. Gabriel, E. H. Grant, E. H. Grant, B. S. J. Halstead, and D. M. P. Mingos, "Dielectric parameters relevant to microwave dielectric heating," *Chemical Society Reviews*, vol. 27, no. 3, p. 213, 1998. [Online]. Available: http://dx.doi.org/10.1039/A827213Z

[42] J. Mijović and J. Wijaya, "Review of cure of polymers and composites by microwave energy," *Polymer Composites*, vol. 11, no. 3, pp. 184–191, 1990. [Online]. Available: http://dx.doi.org/10.1002/pc.750110307

[43] M. Chen, E. J. Siochi, T. C. Ward, and J. E. McGrath, "Basic ideas of microwave processing of polymers," *Polymer Engineering & Science*, vol. 33, no. 17, pp. 1092–1109, 1993. [Online]. Available: http://dx.doi.org/10.1002/pen.760331703

[44] J. Tang, "Unlocking potentials of microwaves for food safety and quality," *Journal of Food Science*, vol. 80, no. 8, p. nil, 2015. [Online]. Available: http://dx.doi.org/10.1111/1750-3841.12959

[45] M. C. Navarro, "Water, toluene, methanol, and ethanol under microwave irradiation: Numerical simulations of the effect of the vessel's size," *Journal of Heat Transfer*, vol. 142, no. 10, p. nil, 2020. [Online]. Available: http://dx.doi.org/10.1115/1.4047512

[46] S. Horikoshi, T. Sumi, and N. Serpone, "Unusual effect of the magnetic field component of the microwave radiation on aqueous electrolyte solutions," *Journal of Microwave Power and Electromagnetic Energy*, vol. 46, no. 4, pp. 215–228, 2012. [Online]. Available: http://dx.doi.org/10.1080/08327823.2012.11689838

[47] F. Wiesbrock, R. Hoogenboom, and U. S. Schubert, "Microwave-assisted polymer synthesis: State-of-the-art and future perspectives," *Macromolecular Rapid Communications*, vol. 25, no. 20, pp. 1739–1764, 2004. [Online]. Available: http://dx.doi.org/10.1002/marc.200400313

[48] C. O. Kappe, "My twenty years in microwave chemistry: From kitchen ovens to microwaves that aren't microwaves," *The Chemical Record*, vol. 19, no. 1, pp. 15–39, 2018. [Online]. Available: http://dx.doi.org/10.1002/tcr.201800045

[49] P. Singla, R. Mehta, D. Berek, and S. N. Upadhyay, "Microwave assisted synthesis of poly(lactic acid) and its characterization using size exclusion chromatography," *Journal of Macromolecular Science, Part A*, vol. 49, no. 11, pp. 963–970, 2012. [Online]. Available: http://dx.doi.org/10.1080/10601325.2012.722858

[50] P. Singla, P. Kaur, R. Mehta, D. Berek, and S. Upadhyay, "Ring-opening polymerization of lactide using microwave and conventional heating," *Procedia Chemistry*, vol. 4, no. nil, pp. 179–185, 2012. [Online]. Available: http://dx.doi.org/10.1016/j.proche.2012.06.025

[51] P. Singla, R. Mehta, D. Berek, and S. N. Upadhyay, "Ring opening polymerization of lactide in a monomode microwave using stannous octoate and dibutyltin dimethoxide catalysts," *Journal of Macromolecular Science, Part A*, vol. 51, no. 4, pp. 350–361, 2014. [Online]. Available: http://dx.doi.org/10.1080/10601325.2014.882701

[52] T. P. University, G. Guba, A. Gusar, T. P. University, E. Mamaeva, T. P. University, V. Popova, T. P. University, I. Dolgov, T. P. University, A. Bakibayev, N. R. T. S. University, R. Ahmedjanov, and T. S. P. University, "Polymerization

of lactic acid oligomers under microwave irradiation," *Bulletin of the Karaganda University. "Chemistry" series*, vol. 96, no. 4, pp. 8–17, 2019. [Online]. Available: http://dx.doi.org/10.31489/2019Ch4/8-17

[53] B. Luo, J. Yang, J. Zhao, C. Hsu, J. Li, and C. Zhou, "Rapid synthesis and characterization of chitosan-*g*-poly(D,L-lactide) copolymers with hydroxyethyl chitosan as a macroinitiator under microwave irradiation," *Journal of Applied Polymer Science*, vol. 125, no. S2, p. nil, 2012. [Online]. Available: http://dx.doi.org/10.1002/app.35603

[54] L. Huang, J. Tan, W. Li, L. Zhou, Z. Liu, B. Luo, L. Lu, and C. Zhou, "Functional polyhedral oligomeric silsesquioxane reinforced poly(lactic acid) nanocomposites for biomedical applications," *Journal of the Mechanical Behavior of Biomedical Materials*, vol. 90, no. nil, pp. 604–614, 2019. [Online]. Available: http://dx.doi.org/10.1016/j.jmbbm.2018.11.002

[55] D. Kojić, T. Erceg, N. Vukić, V. Teofilović, I. Ristić, J. Budinski-Simendić, and V. Aleksić, "The catalytic microwave synthesis of biodegradable polyester polyols based on castor oil and l-lactide," *IOP Conference Series: Materials Science and Engineering*, vol. 163, no. nil, p. 012048, 2017. [Online]. Available: http://dx.doi.org/10.1088/1757-899X/163/1/012048

[56] C. Thauvin, P. Maudens, and E. Allémann, "Microwave-assisted synthesis of self-assembling bi-functionalizable amphiphilic diblock copolymers," *Journal of Drug Delivery Science and Technology*, vol. 61, no. nil, p. 102255, 2021. [Online]. Available: http://dx.doi.org/10.1016/j.jddst.2020.102255

[57] J. Ramier, E. Renard, and D. Grande, "Microwave-assisted synthesis and characterization of biodegradable block copolyesters based on poly(3-hydroxyalkanoate)s and poly(D,L-lactide)," *Journal of Polymer Science Part A: Polymer Chemistry*, vol. 50, no. 7, pp. 1445–1455, 2012. [Online]. Available: http://dx.doi.org/10.1002/pola.25916

[58] A. Nan, R. Turcu, and J. Liebscher, "Magnetite-polylactic acid core-shell nanoparticles by ring-opening polymerization under microwave irradiation," *Journal of Polymer Science Part A: Polymer Chemistry*, vol. 50, no. 8, pp. 1485–1490, 2012. [Online]. Available: http://dx.doi.org/10.1002/pola.25920

[59] I. S. Ristić, L. Tanasić, L. B. Nikolić, S. M. Cakić, O. Z. Ilić, R. Z. Radicević, and J. K. Budinski-Simendić, "The properties of poly(l-lactide) prepared by different synthesis procedure," *Journal of Polymers and the Environment*, vol. 19, no. 2, pp. 419–430, 2011. [Online]. Available: http://dx.doi.org/10.1007/s10924-011-0297-1

[60] C. Thauvin, J. Widmer, I. Mottas, S. Hocevar, E. Allémann, C. Bourquin, and F. Delie, "Development of resiquimod-loaded modified PLA-based nanoparticles for cancer immunotherapy: a kinetic study," *European Journal of Pharmaceutics and Biopharmaceutics*, vol. 139, no. nil, pp. 253–261, 2019. [Online]. Available: http://dx.doi.org/10.1016/j.ejpb.2019.04.007

[61] S. Yin, M. Ji, and R. Yao, "One-Step Synthesis of Polylactide-Dextran Grafted Copolymers and Its Controlled Release on Coenzyme A," *Asian Journal of Chemistry*, vol. 25, no. 13, pp. 7561–7566, 2013. [Online]. Available: http://dx.doi.org/10.14233/ajchem.2013.15249

[62] T. Xu, Y. Ma, J. Huang, H. Lai, D. Yuan, X. Tang, and L. Yang, "Self-organized thermo-responsive poly(lactic-co-glycolic acid)-graft-pullulan nanoparticles for synergistic thermo-chemotherapy of tumor," *Carbohydrate Polymers*, vol. 237, no. nil, p. 116104, 2020. [Online]. Available: http://dx.doi.org/10.1016/j.carbpol.2020.116104

[63] K. Salimi, M. Topuzogullari, S. Dincer, H. M. Aydin, and E. Piskin, "Microwave-assisted green approach for graft copolymerization of L-lactic acid onto starch," *Journal of Applied Polymer Science*, vol. 133, no. 6, p. nil, 2015. [Online]. Available: http://dx.doi.org/10.1002/app.42937

[64] B.-H. Luo, C.-E. Hsu, J.-H. Li, L.-F. Zhao, M.-X. Liu, X.-Y. Wang, and C.-R. Zhou, "Nano-composite of poly(l-lactide) and halloysite nanotubes surface-grafted with l-lactide oligomer under microwave irradiation," *Journal of Biomedical Nanotechnology*, vol. 9, no. 4, pp. 649–658, 2013. [Online]. Available: http://dx.doi.org/10.1166/jbn.2013.1570

[65] J. Arredondo, L. E. Elizalde, B. L. Droumaguet, and D. Grande, "A new route toward imidazoline-functionalized porous polymeric materials from corresponding polystyrene-polylactide diblock copolymers," *Reactive and Functional Polymers*, vol. 104, no. nil, pp. 62–70, 2016. [Online]. Available: http://dx.doi.org/10.1016/j.reactfunctpolym.2016.05.003

[66] M. Frediani, D. Sémeril, D. Matt, L. Rosi, P. Frediani, F. Rizzolo, and A. M. Papini, "Ring-Opening Polymerisation of *rac*-Lactide Using a Calix[4]arene-Based Titanium (IV) Complex," *International Journal of Polymer Science*, vol. 2010, no. nil, pp. 1–6, 2010. [Online]. Available: http://dx.doi.org/10.1155/2010/490724

[67] R. M. Lord, F. D. Janeway, L. Bird, and P. C. McGowan, "Bis(phenyl-β-diketonato)titanium(IV) ethoxide complexes: Ring-opening polymerization of L-lactide by solvent-free microwave irradiation," *Polyhedron*, vol. 211, no. nil, p. 115520, 2022. [Online]. Available: http://dx.doi.org/10.1016/j.poly.2021.115520

[68] H. Rodríguez-Tobías, G. Morales, F. J. Enríquez-Medrano, and D. Grande, "Performance of zinc oxide nanoparticles as polymerization initiating systems in the microwave-assisted synthesis of poly(D,L-lactide)/ZnO nanocomposites," *Macromolecular Symposia*, vol. 374, no. 1, p. nil, 2017. [Online]. Available: http://dx.doi.org/10.1002/masy.201600102

[69] A. H. Mijinyawa, G. Durga, and A. Mishra, "Isolation, characterization, and microwave assisted surface modification of colocasia esculenta (l.) schott mucilage by grafting polylactide," *International Journal of Biological Macromolecules*, vol. 119, no. nil, pp. 1090–1097, 2018. [Online]. Available: http://dx.doi.org/10.1016/j.ijbiomac.2018.08.045

[70] C. Thauvin, B. Schwarz, F. Delie, and E. Allémann, "Functionalized PLA polymers to control loading and/or release properties of drug-loaded nanoparticles," *International Journal of Pharmaceutics*, vol. 548, no. 2, pp. 771–777, 2018. [Online]. Available: http://dx.doi.org/10.1016/j.ijpharm.2017.11.001

[71] A. Bakibaev, A. Gazaliev, S. Kabieva, V. Fedorchenko, G. Guba, E. Smetanina, I. Dolgov, and R. Gulyaev, "Polymerization of lactic acid using microwave and conventional heating," *Procedia Chemistry*, vol. 15, no. nil, pp. 97–102, 2015. [Online]. Available: http://dx.doi.org/10.1016/j.proche.2015.10.015

[72] H. L. Cao, P. Wang, and W. B. Yuan, "Microwave-assisted synthesis of poly(L-lactic acid) via direct melt polycondensation using solid super-acids," *Macromolecular Chemistry and Physics*, vol. 210, no. 23, pp. 2058–2062, 2009. [Online]. Available: http://dx.doi.org/10.1002/macp.200900231

[73] B. T. Ergan and M. Bayramoğlu, "Poly (L-lactic acid) synthesis using continuous microwave irradiation-simultaneous cooling method," *Chemical Engineering Communications*, vol. 205, no. 12, pp. 1665–1677, 2018. [Online]. Available: http://dx.doi.org/10.1080/00986445.2018.1464446

[74] C. Nastruzzi, Capretto, Mazzitelli, Brognara, Lampronti, Carugo, Hill, Zhang, and Gambari, "Mithramycin encapsulated in polymeric micelles by microfluidic technology as novel therapeutic protocol for beta-thalassemia," *International*

Journal of Nanomedicine, vol. nil, no. nil, p. 307, 2012. [Online]. Available: http://dx.doi.org/10.2147/IJN.S25657

[75] H. Bhardwaj and R. K. Jangde, "Current updated review on preparation of polymeric nanoparticles for drug delivery and biomedical applications," *Next Nanotechnology*, vol. 2, no. nil, p. 100013, 2023. [Online]. Available: http://dx.doi.org/10.1016/j.nxnano.2023.100013

[76] A. Zielińska, F. Carreiró, A. M. Oliveira, A. Neves, B. Pires, D. N. Venkatesh, A. Durazzo, M. Lucarini, P. Eder, A. M. Silva, A. Santini, and E. B. Souto, "Polymeric nanoparticles: Production, characterization, toxicology and ecotoxicology," *Molecules*, vol. 25, no. 16, p. 3731, 2020. [Online]. Available: http://dx.doi.org/10.3390/molecules25163731

[77] S. Kumar, N. Dilbaghi, R. Saharan, and G. Bhanjana, "Nanotechnology as emerging tool for enhancing solubility of poorly water-soluble drugs," *BioNanoScience*, vol. 2, no. 4, pp. 227–250, 2012. [Online]. Available: http://dx.doi.org/10.1007/s12668-012-0060-7

[78] E. B. Souto, S. B. Souto, J. R. Campos, P. Severino, T. N. Pashirova, L. Y. Zakharova, A. M. Silva, A. Durazzo, M. Lucarini, A. A. Izzo, and A. Santini, "Nanoparticle delivery systems in the treatment of diabetes complications," *Molecules*, vol. 24, no. 23, p. 4209, 2019. [Online]. Available: http://dx.doi.org/10.3390/molecules24234209

[79] Y. He, Y. Huang, and Y. Cheng, "Structure evolution of curcumin nanoprecipitation from a micromixer," *Crystal Growth & Design*, vol. 10, no. 3, pp. 1021–1024, 2010. [Online]. Available: http://dx.doi.org/10.1021/cg9009916

[80] I. D. Marco, "Supercritical fluids and nanoparticles in cancer therapy," *Micromachines*, vol. 13, no. 9, p. 1449, 2022. [Online]. Available: http://dx.doi.org/10.3390/mi13091449

[81] M. Chidambaram and K. Krishnasamy, "Modifications to the conventional nanoprecipitation technique: an approach to fabricate narrow sized polymeric nanoparticles," *Advanced Pharmaceutical Bulletin; eISSN 2251-7308*, vol. nil, no. nil, p. nil, 2014. [Online]. Available: http://journals.tbzmed.ac.ir/APB/Manuscript/APB-4-205.pdf

[82] U. Bilati, E. Allémann, and E. Doelker, "Nanoprecipitation versus emulsion-based techniques for the encapsulation of proteins into biodegradable nanoparticles and

process-related stability issues," *AAPS PharmSciTech*, vol. 6, no. 4, pp. E594–E604, 2005. [Online]. Available: http://dx.doi.org/10.1208/pt060474

[83] J. Araújo, E. Vega, C. Lopes, M. Egea, M. Garcia, and E. Souto, "Effect of polymer viscosity on physicochemical properties and ocular tolerance of FB-loaded PLGA nanospheres," *Colloids and Surfaces B: Biointerfaces*, vol. 72, no. 1, pp. 48–56, 2009. [Online]. Available: http://dx.doi.org/10.1016/j.colsurfb.2009.03.028

[84] E. Sánchez-López, M. A. Egea, B. M. Davis, L. Guo, M. Espina, A. M. Silva, A. C. Calpena, E. M. B. Souto, N. Ravindran, M. Ettcheto, A. Camins, M. L. García, and M. F. Cordeiro, "Memantine-loaded pegylated biodegradable nanoparticles for the treatment of glaucoma," *Small*, vol. 14, no. 2, p. nil, 2017. [Online]. Available: http://dx.doi.org/10.1002/smll.201701808

[85] M. Jelvehgari, S. Salatin, J. Barar, M. Barzegar-Jalali, K. Adibkia, and F. Kiafar, "Development of a nanoprecipitation method for the entrapment of a very water soluble drug into Eudragit RL nanoparticles," *Research in Pharmaceutical Sciences*, vol. 12, no. 1, p. 1, 2017. [Online]. Available: http://dx.doi.org/10.4103/1735-5362.199041

[86] C. J. M. Rivas, M. Tarhini, W. Badri, K. Miladi, H. Greige-Gerges, Q. A. Nazari, S. A. G. Rodríguez, R. Á. Román, H. Fessi, and A. Elaissari, "Nanoprecipitation process: From encapsulation to drug delivery," *International Journal of Pharmaceutics*, vol. 532, no. 1, pp. 66–81, 2017. [Online]. Available: http://dx.doi.org/10.1016/j.ijpharm.2017.08.064

[87] L. Capretto, D. Carugo, S. Mazzitelli, C. Nastruzzi, and X. Zhang, "Microfluidic and lab-on-a-chip preparation routes for organic nanoparticles and vesicular systems for nanomedicine applications," *Advanced Drug Delivery Reviews*, vol. 65, no. 11-12, pp. 1496–1532, 2013. [Online]. Available: http://dx.doi.org/10.1016/j.addr.2013.08.002

[88] L. Capretto, D. Carugo, W. Cheng, M. Hill, and X. Zhang, "Continuous-flow production of polymeric micelles in microreactors: Experimental and computational analysis," *Journal of Colloid and Interface Science*, vol. 357, no. 1, pp. 243–251, 2011. [Online]. Available: http://dx.doi.org/10.1016/j.jcis.2011.01.085

[89] R. Othman, G. T. Vladisavljević, and Z. K. Nagy, "Preparation of biodegradable polymeric nanoparticles for pharmaceutical applications using glass capillary microfluidics," *Chemical Engineering Science*, vol. 137, no. nil, pp. 119–130, 2015. [Online]. Available: http://dx.doi.org/10.1016/j.ces.2015.06.025

[90] R. Karnik, F. Gu, P. Basto, C. Cannizzaro, L. Dean, W. Kyei-Manu, R. Langer, and O. C. Farokhzad, "Microfluidic platform for controlled synthesis of polymeric nanoparticles," *Nano Letters*, vol. 8, no. 9, pp. 2906–2912, 2008. [Online]. Available: http://dx.doi.org/10.1021/nl801736q

[91] M. C. Operti, A. Bernhardt, V. Sincari, E. Jager, S. Grimm, A. Engel, M. Hruby, C. G. Figdor, and O. Tagit, "Industrial Scale Manufacturing and Downstream Processing of PLGA-Based Nanomedicines Suitable for Fully Continuous Operation," *Pharmaceutics*, vol. 14, no. 2, p. 276, 2022. [Online]. Available: http://dx.doi.org/10.3390/pharmaceutics14020276

[92] M. C. Operti, A. Bernhardt, J. Pots, V. Sincari, E. Jager, S. Grimm, A. Engel, A. Benedikt, M. Hrubý, I. J. M. D. Vries, C. G. Figdor, and O. Tagit, "Translating the manufacture of immunotherapeutic PLGA nanoparticles from lab to industrial scale: Process transfer and in vitro testing," *Pharmaceutics*, vol. 14, no. 8, p. 1690, 2022. [Online]. Available: http://dx.doi.org/10.3390/pharmaceutics14081690

[93] A. Albisa, E. Piacentini, V. Sebastian, M. Arruebo, J. Santamaria, and L. Giorno, "Preparation of Drug-Loaded PLGA-PEG Nanoparticles by Membrane-Assisted Nanoprecipitation," *Pharmaceutical Research*, vol. 34, no. 6, pp. 1296–1308, 2017. [Online]. Available: http://dx.doi.org/10.1007/s11095-017-2146-y

[94] J. Cheng, N. Zhao, Y. Zhang, Y. Huang, Q. Huang, and C. Xiao, "Facile preparation of PMMA@PLA core-shell microspheres by ptfe membrane emulsification," *Journal of Membrane Science*, vol. 644, no. nil, p. 120178, 2022. [Online]. Available: http://dx.doi.org/10.1016/j.memsci.2021.120178

[95] C. N. Grama, V. P. Venkatpurwar, D. A. Lamprou, and M. N. V. R. Kumar, "Towards scale-up and regulatory shelf-stability testing of curcumin encapsulated polyester nanoparticles," *Drug Delivery and Translational Research*, vol. 3, no. 3, pp. 286–293, 2013. [Online]. Available: http://dx.doi.org/10.1007/s13346-013-0150-2

[96] Y. Dong and S.-S. Feng, "Poly(D,L-lactide-co-glycolide) (PLGA) nanoparticles prepared by high pressure homogenization for paclitaxel chemotherapy," *International Journal of Pharmaceutics*, vol. 342, no. 1-2, pp. 208–214, 2007. [Online]. Available: http://dx.doi.org/10.1016/j.ijpharm.2007.04.031

[97] N. H. Aghda, E. J. Lara, P. Patel, and T. Betancourt, "High throughput preparation of poly(lactic-co-glycolic acid) nanoparticles using fiber fluidic reactor," *Materials*, vol. 13, no. 14, p. 3075, 2020. [Online]. Available: http://dx.doi.org/10.3390/ma13143075

[98] E. Chiesa, M. Bellotti, A. Caimi, B. Conti, R. Dorati, M. Conti, I. Genta, and F. Auricchio, "Development and optimization of microfluidic assisted manufacturing process to produce PLGA nanoparticles," *International Journal of Pharmaceutics*, vol. 629, no. nil, p. 122368, 2022. [Online]. Available: http://dx.doi.org/10.1016/j.ijpharm.2022.122368

[99] K.-I. Min, D. J. Im, H.-J. Lee, and D.-P. Kim, "Three-dimensional flash flow microreactor for scale-up production of monodisperse PEG-PLGA nanoparticles," *Lab Chip*, vol. 14, no. 20, pp. 3987–3992, 2014. [Online]. Available: http://dx.doi.org/10.1039/c4lc00700j

[100] R. Zoqlam, C. J. Morris, M. Akbar, A. M. Alkilany, S. I. Hamdallah, P. Belton, and S. Qi, "Evaluation of the benefits of microfluidic-assisted preparation of polymeric nanoparticles for DNA delivery," *Materials Science and Engineering: C*, vol. 127, no. nil, p. 112243, 2021. [Online]. Available: http://dx.doi.org/10.1016/j.msec.2021.112243

[101] J. Xu, S. Zhang, A. Machado, S. Lecommandoux, O. Sandre, F. Gu, and A. Colin, "Controllable microfluidic production of drug-loaded PLGA nanoparticles using partially water-miscible mixed solvent microdroplets as a precursor," *Scientific Reports*, vol. 7, no. 1, p. 4794, 2017. [Online]. Available: http://dx.doi.org/10.1038/s41598-017-05184-5

[102] X. Kang, C. Luo, Q. Wei, C. Xiong, Q. Chen, Y. Chen, and Q. Ouyang, "Mass production of highly monodisperse polymeric nanoparticles by parallel flow focusing system," *Microfluidics and Nanofluidics*, vol. 15, no. 3, pp. 337–345, 2013. [Online]. Available: http://dx.doi.org/10.1007/s10404-013-1152-6

[103] M. S. Alkanawati, F. R. Wurm, H. Thérien-Aubin, and K. Landfester, "Large-scale preparation of polymer nanocarriers by high-pressure microfluidization," *Macromolecular Materials and Engineering*, vol. 303, no. 1, p. nil, 2017. [Online]. Available: http://dx.doi.org/10.1002/mame.201700505

[104] M. Arruebo, L. Uson, M. Miana, I. O. de Solorzano, V. Sebastian, and A. Larrea, "Continuous synthesis of drug-loaded nanoparticles using microchannel emulsification and numerical modeling: Effect of passive mixing," *International Journal of Nanomedicine*, vol. Volume 11, no. nil, pp. 3397–3416, 2016. [Online]. Available: http://dx.doi.org/10.2147/IJN.S108812

[105] N. Anton, F. Bally, C. A. Serra, A. Ali, Y. Arntz, Y. Mely, M. Zhao, E. Marchioni, A. Jakhmola, and T. F. Vandamme, "A new microfluidic setup

for precise control of the polymer nanoprecipitation process and lipophilic drug encapsulation," *Soft Matter*, vol. 8, no. 41, p. 10628, 2012. [Online]. Available: http://dx.doi.org/10.1039/c2sm25357g

[106] K. M. Pustulka, A. R. Wohl, H. S. Lee, A. R. Michel, J. Han, T. R. Hoye, A. V. McCormick, J. Panyam, and C. W. Macosko, "Flash nanoprecipitation: Particle structure and stability," *Molecular Pharmaceutics*, vol. 10, no. 11, pp. 4367–4377, 2013. [Online]. Available: http://dx.doi.org/10.1021/mp400337f

[107] X. Li and X. Jiang, "Microfluidics for producing poly(lactic-co-glycolic acid)-based pharmaceutical nanoparticles," *Advanced Drug Delivery Reviews*, vol. 128, no. nil, pp. 101–114, 2018. [Online]. Available: http://dx.doi.org/10.1016/j.addr.2017.12.015

[108] S. J. Shepherd, D. Issadore, and M. J. Mitchell, "Microfluidic formulation of nanoparticles for biomedical applications," *Biomaterials*, vol. 274, no. nil, p. 120826, 2021. [Online]. Available: http://dx.doi.org/10.1016/j.biomaterials.2021.120826

[109] J.-M. Lim, N. Bertrand, P. M. Valencia, M. Rhee, R. Langer, S. Jon, O. C. Farokhzad, and R. Karnik, "Parallel microfluidic synthesis of size-tunable polymeric nanoparticles using 3D flow focusing towards *in vivo* study," *Nanomedicine: Nanotechnology, Biology and Medicine*, vol. 10, no. 2, pp. 401–409, 2014. [Online]. Available: http://dx.doi.org/10.1016/j.nano.2013.08.003

[110] J. P. Martins, G. Torrieri, and H. A. Santos, "The importance of microfluidics for the preparation of nanoparticles as advanced drug delivery systems," *Expert Opinion on Drug Delivery*, vol. 15, no. 5, pp. 469–479, 2018. [Online]. Available: http://dx.doi.org/10.1080/17425247.2018.1446936

[111] M. Stoller and J. M. Ochando-Pulido, "ZnO nano-particles production intensification by means of a spinning disk reactor," *Nanomaterials*, vol. 10, no. 7, p. 1321, 2020. [Online]. Available: http://dx.doi.org/10.3390/nano10071321

[112] Y. Lu, X. Zhang, Y. Chu, H. Yu, M. Huo, J. Qu, J. C. Crittenden, H. Huo, and X. Yuan, "Cu_2O nanocrystals/TiO_2 microspheres film on a rotating disk containing long-afterglow phosphor for enhanced round-the-clock photocatalysis," *Applied Catalysis B: Environmental*, vol. 224, no. nil, pp. 239–248, 2018. [Online]. Available: http://dx.doi.org/10.1016/j.apcatb.2017.10.054

[113] X. Ren, J. Niu, Y. Li, L. Li, C. Zhang, Q. Guo, Q. Zhang, and W. Jiao, "Photocatalytic ozonation-based degradation of phenol by ZnO-TiO_2 nanocomposites

in spinning disk reactor," *Chinese Journal of Chemical Engineering*, vol. 72, no. nil, pp. 74–84, 2024. [Online]. Available: http://dx.doi.org/10.1016/j.cjche.2024.03.028

[114] C. Ahoba-Sam, K. Boodhoo, U. Olsbye, and K.-J. Jens, "Tailoring Cu nanoparticle catalyst for methanol synthesis using the spinning disk reactor," *Materials*, vol. 11, no. 1, p. 154, 2018. [Online]. Available: http://dx.doi.org/10.3390/ma11010154

[115] K. Adavi, D. Tahery, M. Khajouei, and M. Latifi, "High local supersaturation formation for precipitated calcium carbonate synthesis by applying a rotating disk reactor," *Brazilian Journal of Chemical Engineering*, vol. nil, no. nil, p. nil, 2023. [Online]. Available: http://dx.doi.org/10.1007/s43153-023-00423-x

[116] F. Haseidl, B. Müller, and O. Hinrichsen, "Continuous-flow synthesis and functionalization of magnetite: Intensified process for tailored nanoparticles," *Chemical Engineering & Technology*, vol. 39, no. 11, pp. 2051–2058, 2016. [Online]. Available: http://dx.doi.org/10.1002/ceat.201600163

[117] W. H. Khan and V. K. Rathod, "Process intensification approach for preparation of curcumin nanoparticles via solvent-nonsolvent nanoprecipitation using spinning disc reactor," *Chemical Engineering and Processing: Process Intensification*, vol. 80, no. nil, pp. 1–10, 2014. [Online]. Available: http://dx.doi.org/10.1016/j.cep.2014.03.011

[118] C. Y. Tai, Y.-H. Wang, and H.-S. Liu, "A green process for preparing silver nanoparticles using spinning disk reactor," *AIChE Journal*, vol. 54, no. 2, pp. 445–452, 2007. [Online]. Available: http://dx.doi.org/10.1002/aic.11396

[119] S. Sana, J. Manson, V. Zivkovic, and K. Boodhoo, "Solvent-antisolvent precipitation in a spinning disc reactor: Precipitation kinetics and mathematical modelling of starch nanoparticles," *Chemical Engineering and Processing - Process Intensification*, vol. 176, no. nil, p. 108962, 2022. [Online]. Available: http://dx.doi.org/10.1016/j.cep.2022.108962

[120] S. D. Pask, O. Nuyken, and Z. Cai, "The spinning disk reactor: an example of a process intensification technology for polymers and particles," *Polymer Chemistry*, vol. 3, no. 10, p. 2698, 2012. [Online]. Available: http://dx.doi.org/10.1039/c2py20237a

[121] K. Boodhoo and R. Jachuck, "Process intensification: Spinning disk reactor for styrene polymerisation," *Applied Thermal Engineering*, vol. 20, no. 12, pp. 1127–1146, 2000. [Online]. Available: http://dx.doi.org/10.1016/S1359-4311(99)00071-X

[122] S. Mohammadi, A. Harvey, and K. V. Boodhoo, "Synthesis of TiO_2 nanoparticles in a spinning disc reactor," *Chemical Engineering Journal*, vol. 258, no. nil, pp. 171–184, 2014. [Online]. Available: http://dx.doi.org/10.1016/j.cej.2014.07.042

[123] A. N. M. Martínez, M. Assirelli, and J. van der Schaaf, "Droplet size and liquid-liquid mass transfer with reaction in a rotor-stator spinning disk reactor," *Chemical Engineering Science*, vol. 242, no. nil, p. 116706, 2021. [Online]. Available: http://dx.doi.org/10.1016/j.ces.2021.116706

[124] M. Meeuwse, J. van der Schaaf, B. Kuster, and J. Schouten, "Gas-liquid mass transfer in a rotor-stator spinning disc reactor," *Chemical Engineering Science*, vol. 65, no. 1, pp. 466–471, 2010. [Online]. Available: http://dx.doi.org/10.1016/j.ces.2009.06.006

[125] F. Visscher, J. van der Schaaf, M. de Croon, and J. Schouten, "Liquid-liquid mass transfer in a rotor-stator spinning disc reactor," *Chemical Engineering Journal*, vol. 185-186, no. nil, pp. 267–273, 2012. [Online]. Available: http://dx.doi.org/10.1016/j.cej.2012.01.002

[126] M. de Beer, L. P. M. Loane, J. Keurentjes, J. Schouten, and J. van der Schaaf, "Single phase fluid-stator heat transfer in a rotor-stator spinning disc reactor," *Chemical Engineering Science*, vol. 119, no. nil, pp. 88–98, 2014. [Online]. Available: http://dx.doi.org/10.1016/j.ces.2014.08.008

[127] F. Visscher, J. de Hullu, M. H. J. M. de Croon, J. van der Schaaf, and J. C. Schouten, "Residence time distribution in a single-phase rotor-stator spinning disk reactor," *AIChE Journal*, vol. 59, no. 7, pp. 2686–2693, 2013. [Online]. Available: http://dx.doi.org/10.1002/aic.14036

[128] F. Haseidl, P. König, and O. Hinrichsen, "Single-phase flow residence-time distributions in a rotor-stator spinning disc reactor," *Chemical Engineering & Technology*, vol. 39, no. 12, pp. 2435–2443, 2016. [Online]. Available: http://dx.doi.org/10.1002/ceat.201600247

[129] A. N. M. Martínez, R. Jansen, K. Walker, M. Assirelli, and J. van der Schaaf, "Experimental and modeling study on meso- and micromixing in the rotor-stator spinning disk reactor," *Chemical Engineering Research and Design*, vol. 173, no. nil, pp. 279–288, 2021. [Online]. Available: http://dx.doi.org/10.1016/j.cherd.2021.07.012

[130] E. Arian and W. Pauer, "A comprehensive investigation of the incorporation model for micromixing time calculation," *Chemical Engineering Research and*

Design, vol. 175, no. nil, pp. 296–308, 2021. [Online]. Available: http://dx.doi.org/10.1016/j.cherd.2021.09.010

[131] J.-M. Commenge and L. Falk, "Villermaux-dushman protocol for experimental characterization of micromixers," *Chemical Engineering and Processing: Process Intensification*, vol. 50, no. 10, pp. 979–990, 2011. [Online]. Available: http://dx.doi.org/10.1016/j.cep.2011.06.006

[132] R. Gu, K. Cheng, and L. Wen, "Application of the engulfment model in assessing micromixing time of a micro-impinging stream reactor based on the determination of impinging zone with CFD," *Chemical Engineering Journal*, vol. 409, no. nil, p. 128248, 2021. [Online]. Available: http://dx.doi.org/10.1016/j.cej.2020.128248

[133] J. Bałdyga and R. Pohorecki, "Turbulent micromixing in chemical reactors - a review," *The Chemical Engineering Journal and the Biochemical Engineering Journal*, vol. 58, no. 2, pp. 183–195, 1995. [Online]. Available: http://dx.doi.org/10.1016/0923-0467(95)02982-6

[134] A. N. M. Martínez, K. M. van Eeten, J. C. Schouten, and J. van der Schaaf, "Micromixing in a rotor-stator spinning disc reactor," *Industrial & Engineering Chemistry Research*, vol. 56, no. 45, pp. 13 454–13 460, 2017. [Online]. Available: http://dx.doi.org/10.1021/acs.iecr.7b01324

[135] A. Chaudhuri, K. P. Kuijpers, R. B. Hendrix, P. Shivaprasad, J. A. Hacking, E. A. Emanuelsson, T. Noël, and J. van der Schaaf, "Process intensification of a photochemical oxidation reaction using a rotor-stator spinning disk reactor: a strategy for scale up," *Chemical Engineering Journal*, vol. 400, no. nil, p. 125875, 2020. [Online]. Available: http://dx.doi.org/10.1016/j.cej.2020.125875

[136] J. Kleiner and O. Hinrichsen, "Epoxidation of methyl oleate in a rotor-stator spinning disc reactor," *Chemical Engineering and Processing - Process Intensification*, vol. 136, no. nil, pp. 152–162, 2019. [Online]. Available: http://dx.doi.org/10.1016/j.cep.2019.01.004

[137] A. Chaudhuri, E. B. Temelli, C. J. W. Hop, V. P. Sureshkumar, and J. van der Schaaf, "Transesterification of triglycerides in a rotor-stator spinning disc reactor: Scale-up and solid handling," *Industrial & Engineering Chemistry Research*, vol. 61, no. 20, pp. 6831–6844, 2022. [Online]. Available: http://dx.doi.org/10.1021/acs.iecr.2c00690

[138] D. Zou, J. Li, J. Deng, Y. Jin, and M. Chen, "Continuous Preparation of Size-Controllable $BaTiO_3$ Nanoparticles in a Rotor-Stator Spinning Disk Reactor," *Industrial & Engineering Chemistry Research*, vol. 60, no. 40, pp. 14 511–14 518, 2021. [Online]. Available: http://dx.doi.org/10.1021/acs.iecr.1c02152

[139] G. Jacquet-Richardet, M. Torkhani, P. Cartraud, F. Thouverez, T. N. Baranger, M. Herran, C. Gibert, S. Baguet, P. Almeida, and L. Peletan, "Rotor to stator contacts in turbomachines. review and application," *Mechanical Systems and Signal Processing*, vol. 40, no. 2, pp. 401–420, 2013. [Online]. Available: http://dx.doi.org/10.1016/j.ymssp.2013.05.010

[140] T. Lin, Z. Zhu, X. Li, J. Li, and Y. Lin, "Theoretical, experimental, and numerical methods to predict the best efficiency point of centrifugal pump as turbine," *Renewable Energy*, vol. 168, no. nil, pp. 31–44, 2021. [Online]. Available: http://dx.doi.org/10.1016/j.renene.2020.12.040

[141] A. Håkansson, "Rotor-stator mixers: From batch to continuous mode of operation-a review," *Processes*, vol. 6, no. 4, p. 32, 2018. [Online]. Available: http://dx.doi.org/10.3390/pr6040032

[142] B. H. Samani, M. Behruzian, G. Najafi, E. Fayyazi, B. Ghobadian, A. Behruzian, M. Mofijur, M. Mazlan, and J. Yue, "The rotor-stator type hydrodynamic cavitation reactor approach for enhanced biodiesel fuel production," *Fuel*, vol. 283, no. nil, p. 118821, 2021. [Online]. Available: http://dx.doi.org/10.1016/j.fuel.2020.118821

[143] J. W. Daily and R. E. Nece, "Chamber dimension effects on induced flow and frictional resistance of enclosed rotating disks," *Journal of Basic Engineering*, vol. 82, no. 1, pp. 217–230, 1960. [Online]. Available: http://dx.doi.org/10.1115/1.3662532

[144] M. de Beer, J. Keurentjes, J. Schouten, and J. van der Schaaf, "Engineering model for single-phase flow in a multi-stage rotor-stator spinning disc reactor," *Chemical Engineering Journal*, vol. 242, no. nil, pp. 53–61, 2014. [Online]. Available: http://dx.doi.org/10.1016/j.cej.2013.12.052

[145] S. Haddadi and S. Poncet, "Turbulence modeling of torsional couette flows," *International Journal of Rotating Machinery*, vol. 2008, no. 1, p. nil, 2008. [Online]. Available: http://dx.doi.org/10.1155/2008/635138

[146] G. K. BATCHELOR, "NOTE ON A CLASS OF SOLUTIONS OF THE NAVIER-STOKES EQUATIONS REPRESENTING STEADY ROTATIONALLY-SYMMETRIC FLOW," *The Quarterly Journal of Mechanics and Applied Mathematics*,

vol. 4, no. 1, pp. 29–41, 1951. [Online]. Available: http://dx.doi.org/10.1093/qjmam/4.1.29

[147] M. Khirennas, H. Oualli, M. Mekadem, T. Azzam, A. Benaiche, and A. Bouabdallah, "Mechanism of vortices appearance in the taylor-couette flow system," *Journal of Applied Fluid Mechanics*, vol. 15, no. 1, pp. 129–137, 2022.

[148] M. G. Larson and F. Bengzon, *The Finite Element Method: Theory, Implementation, and Applications*, ser. Texts in Computational Science and Engineering. Springer Berlin Heidelberg, 2013. [Online]. Available: http://dx.doi.org/10.1007/978-3-642-33287-6

[149] B. Blais, L. Barbeau, V. Bibeau, S. Gauvin, T. E. Geitani, S. Golshan, R. Kamble, G. Mirakhori, and J. Chaouki, "Lethe: an open-source parallel high-order adaptative cfd solver for incompressible flows," *SoftwareX*, vol. 12, no. nil, p. 100579, 2020. [Online]. Available: http://dx.doi.org/10.1016/j.softx.2020.100579

[150] P. C. Africa, D. Arndt, W. Bangerth, B. Blais, M. Fehling, R. Gassmöller, T. Heister, L. Heltai, S. Kinnewig, M. Kronbichler, M. Maier, P. Munch, M. Schreter-Fleischhacker, J. P. Thiele, B. Turcksin, D. Wells, and V. Yushutin, "The deal.ii library, version 9.6," *Journal of Numerical Mathematics*, vol. 32, no. 4, pp. 369–380, 2024. [Online]. Available: http://dx.doi.org/10.1515/jnma-2024-0137

[151] L. P. Saavedra, P. Munch, and B. Blais, "A Matrix-Free Stabilized Solver for the Incompressible Navier-Stokes Equations," 2024. [Online]. Available: http://dx.doi.org/10.2139/ssrn.4981567

[152] M. Itoh, Y. Yamada, S. Imao, and M. Gonda, "Experiments on turbulent flow due to an enclosed rotating disk," *Experimental Thermal and Fluid Science*, vol. 5, no. 3, pp. 359–368, 1992. [Online]. Available: http://dx.doi.org/10.1016/0894-1777(92)90081-F

[153] L. SCHOUVEILER, P. L. GAL, and M. P. CHAUVE, "Instabilities of the flow between a rotating and a stationary disk," *Journal of Fluid Mechanics*, vol. 443, no. nil, pp. 329–350, 2001. [Online]. Available: http://dx.doi.org/10.1017/S0022112001005328

[154] S. Poncet, R. Schiestel, and M.-P. Chauve, "Centrifugal flow in a rotor-stator cavity," *Journal of Fluids Engineering*, vol. 127, no. 4, pp. 787–794, 2005. [Online]. Available: http://dx.doi.org/10.1115/1.1949645

[155] S. Poncet, M.-P. Chauve, and R. Schiestel, "Batchelor versus Stewartson flow structures in a rotor-stator cavity with throughflow," *Physics of Fluids*, vol. 17, no. 7, p. nil, 2005. [Online]. Available: http://dx.doi.org/10.1063/1.1964791

[156] C. J. W. Hop, R. Jansen, M. Besten, A. Chaudhuri, M. W. Baltussen, and J. van der Schaaf, "Hydrodynamics of a rotor-stator spinning disk reactor: Investigations by large-eddy simulation," *Physics of Fluids*, vol. 35, no. 3, p. nil, 2023. [Online]. Available: http://dx.doi.org/10.1063/5.0137405

[157] Z. Wen and J. Petera, "Numerical analysis of the effect of hydrodynamics and operating conditions on biodiesel synthesis in a rotor-stator spinning disk reactor," *Chemical and Process Engineering*, vol. 38, no. 2, pp. 265–281, 2017. [Online]. Available: http://dx.doi.org/10.1515/cpe-2017-0020

[158] Y. Wang, M. Chen, Y. Jin, Y. Ouguang, and J. Li, "CFD simulation of liquid flow characteristics in a rotor-stator spinning disc reactor," *Journal of the Taiwan Institute of Chemical Engineers*, vol. 115, no. nil, pp. 20–27, 2020. [Online]. Available: http://dx.doi.org/10.1016/j.jtice.2020.10.003

[159] É. Séverac, S. Poncet, É. Serre, and M.-P. Chauve, "Large eddy simulation and measurements of turbulent enclosed rotor-stator flows," *Physics of Fluids*, vol. 19, no. 8, p. nil, 2007. [Online]. Available: http://dx.doi.org/10.1063/1.2759530

[160] Z. Jiao and S. Fu, "Investigations of an enclosed annular rotor-stator system with LES method," *Science China Physics, Mechanics & Astronomy*, vol. 61, no. 11, p. 114711, 2018. [Online]. Available: http://dx.doi.org/10.1007/s11433-018-9228-x

[161] N. Y. Bailey, J. M. Owen, I. F. Mear, and H. Tang, "Prediction of flows in enclosed rotor-stator cavities," *Physics of Fluids*, vol. 34, no. 10, p. nil, 2022. [Online]. Available: http://dx.doi.org/10.1063/5.0107336

[162] K. M. P. van Eeten, J. van der Schaaf, J. C. Schouten, and G. J. F. van Heijst, "Boundary layer development in the flow field between a rotating and a stationary disk," *Physics of Fluids*, vol. 24, no. 3, p. nil, 2012. [Online]. Available: http://dx.doi.org/10.1063/1.3698406

[163] M. S. Lopes, A. Jardini, and R. M. Filho, "Poly (lactic acid) production for tissue engineering applications," *Procedia Engineering*, vol. 42, no. nil, pp. 1402–1413, 2012. [Online]. Available: http://dx.doi.org/10.1016/J.PROENG.2012.07.534

[164] B. Tyler, D. Gullotti, A. Mangraviti, T. Utsuki, and H. Brem, "Polylactic acid (PLA) controlled delivery carriers for biomedical applications," *Advanced Drug Delivery Reviews*, vol. 107, no. nil, pp. 163–175, 2016. [Online]. Available: http://dx.doi.org/10.1016/J.ADDR.2016.06.018

[165] T. L. de Albuquerque, J. E. M. Júnior, L. P. de Queiroz, A. D. S. Ricardo, and M. V. P. Rocha, "Polylactic acid production from biotechnological routes: a review," *International Journal of Biological Macromolecules*, vol. 186, no. nil, pp. 933–951, 2021. [Online]. Available: http://dx.doi.org/10.1016/j.ijbiomac.2021.07.074

[166] L. Nikolic, I. Ristic, B. Adnadjevic, V. Nikolic, J. Jovanovic, and M. Stankovic, "Novel Microwave-Assisted Synthesis of Poly(D,L-Lactide): The Influence of Monomer/Initiator Molar Ratio on the Product Properties," *Sensors*, vol. 10, no. 5, pp. 5063–5073, 2010. [Online]. Available: http://dx.doi.org/10.3390/s100505063

[167] P. R. Gruber, J. J. Kolstad, E. S. Hall, R. S. Eichen Conn, and C. M. Ryan, "5,338,822: Melt-stable lactide polymer compost on and process for manufacture thereof."

[168] Y. Yu, G. Storti, and M. Morbidelli, "Ring-Opening Polymerization of L,L-Lactide: Kinetic and Modeling Study," *Macromolecules*, vol. 42, no. 21, pp. 8187–8197, 2009. [Online]. Available: http://dx.doi.org/10.1021/ma901359x

[169] F. Wiesbrock, R. Hoogenboom, and U. S. Schubert, "Microwave-assisted polymer synthesis: State-of-the-art and future perspectives," *Macromolecular Rapid Communications*, vol. 25, no. 20, pp. 1739–1764, 2004. [Online]. Available: http://dx.doi.org/10.1002/MARC.200400313

[170] A. Aguilar-Reynosa, A. Romaní, R. M. Rodríguez-Jasso, C. N. Aguilar, G. Garrote, and H. A. Ruiz, "Microwave heating processing as alternative of pretreatment in second-generation biorefinery: an overview," *Energy Conversion and Management*, vol. 136, no. nil, pp. 50–65, 2017. [Online]. Available: http://dx.doi.org/10.1016/j.enconman.2017.01.004

[171] J. M. Hill and M. J. Jennings, "Formulation of model equations for heating by microwave radiation," *Applied Mathematical Modelling*, vol. 17, no. 7, pp. 369–379, 1993. [Online]. Available: http://dx.doi.org/10.1016/0307-904X(93)90061-K

[172] R. Hoogenboom and U. S. Schubert, "Microwave-assisted polymer synthesis: Recent developments in a rapidly expanding field of research," *Macromolecular*

Rapid Communications, vol. 28, no. 4, pp. 368–386, 2007. [Online]. Available: http://dx.doi.org/10.1002/MARC.200600749

[173] S. Jing, W. Peng, Z. Tong, and Z. Baoxiu, "Microwave-irradiated ring-opening polymerization of D,L-lactide under atmosphere," *Journal of Applied Polymer Science*, vol. 100, no. 3, pp. 2244–2247, 2006. [Online]. Available: http://dx.doi.org/10.1002/app.22527

[174] C. Leonelli and T. J. Mason, "Microwave and ultrasonic processing: Now a realistic option for industry," *Chemical Engineering and Processing: Process Intensification*, vol. 49, no. 9, pp. 885–900, 2010. [Online]. Available: http://dx.doi.org/10.1016/j.cep.2010.05.006

[175] W.-J. Zhi, L.-F. Wang, and X.-J. Hu, "Recent advances in the effects of microwave radiation on brains," *Military Medical Research*, vol. 4, no. 1, p. 29, 2017. [Online]. Available: http://dx.doi.org/10.1186/s40779-017-0139-0

[176] H. Rodríguez-Tobías, G. Morales, A. Olivas, and D. Grande, "One-pot formation of ZnO-graft-poly(D,L-lactide) hybrid systems via microwave-assisted polymerization of D,L-lactide in the presence of ZnO nanoparticles," *Macromolecular Chemistry and Physics*, vol. 216, no. 15, pp. 1629–1637, 2015. [Online]. Available: http://dx.doi.org/10.1002/macp.201500171

[177] H. L. Cao, P. Wang, and W. B. Yuan, "Microwave-assisted synthesis of poly(L-lactic acid) via direct melt polycondensation using solid super-acids," *Macromolecular Chemistry and Physics*, vol. 210, no. 23, pp. 2058–2062, 2009. [Online]. Available: http://dx.doi.org/10.1002/macp.200900231

[178] F. E. Kohn, J. W. A. V. D. Berg, G. V. D. Ridder, and J. Feijen, "The ring-opening polymerization of D,L-lactide in the melt initiated with tetraphenyltin," *Journal of Applied Polymer Science*, vol. 29, no. 12, pp. 4265–4277, 1984. [Online]. Available: http://dx.doi.org/10.1002/app.1984.070291255

[179] N. Najafi, M. Heuzey, P. Carreau, and P. M. Wood-Adams, "Control of thermal degradation of polylactide (PLA)-clay nanocomposites using chain extenders," *Polymer Degradation and Stability*, vol. 97, no. 4, pp. 554–565, 2012. [Online]. Available: http://dx.doi.org/10.1016/j.polymdegradstab.2012.01.016

[180] D. Cam and M. Marucci, "Influence of residual monomers and metals on poly (l-lactide) thermal stability," *Polymer*, vol. 38, no. 8, pp. 1879–1884, 1997. [Online]. Available: http://dx.doi.org/10.1016/S0032-3861(96)00711-2

[181] M.-B. Coltelli, A. Bertolini, L. Aliotta, V. Gigante, A. Vannozzi, and A. Lazzeri, "Chain extension of poly(lactic acid) (PLA)-based blends and composites containing bran with biobased compounds for controlling their processability and recyclability," *Polymers*, vol. 13, no. 18, p. 3050, 2021. [Online]. Available: http://dx.doi.org/10.3390/polym13183050

[182] J. Ramier, E. Renard, and D. Grande, "Microwave-assisted synthesis and characterization of biodegradable block copolyesters based on poly(3-hydroxyalkanoate)s and poly(D,L-lactide)," *Journal of Polymer Science Part A: Polymer Chemistry*, vol. 50, no. 7, pp. 1445–1455, 2012. [Online]. Available: http://dx.doi.org/10.1002/pola.25916

[183] X. Zhang, D. A. MacDonald, M. F. A. Goosen, and K. B. McAuley, "Mechanism of lactide polymerization in the presence of stannous octoate: the effect of hydroxy and carboxylic acid substances," *Journal of Polymer Science Part A: Polymer Chemistry*, vol. 32, no. 15, pp. 2965–2970, 1994. [Online]. Available: http://dx.doi.org/10.1002/pola.1994.080321519

[184] S. Rathi, E. Coughlin, S. Hsu, C. Golub, G. Ling, and M. Tzivanis, "Maintaining structural stability of poly(lactic acid): Effects of multifunctional epoxy based reactive oligomers," *Polymers*, vol. 6, no. 4, pp. 1232–1250, 2014. [Online]. Available: http://dx.doi.org/10.3390/polym6041232

[185] P. Dubois, C. Jacobs, R. Jerome, and P. Teyssie, "Macromolecular engineering of polylactones and polylactides. 4. Mechanism and kinetics of lactide homopolymerization by aluminum isopropoxide," *Macromolecules*, vol. 24, no. 9, pp. 2266–2270, 1991. [Online]. Available: http://dx.doi.org/10.1021/ma00009a022

[186] A. Kowalski, A. Duda, and S. Penczek, "Kinetics and mechanism of cyclic esters polymerization initiated with tin(II) octoate, 1. Polymerization of η-caprolactone," *Macromolecular Rapid Communications*, vol. 19, no. 11, pp. 567–572, 1998. [Online]. Available: http://dx.doi.org/10.1002/(SICI)1521-3927(19981101)19:11<567::AID-MARC567>3.0.CO;2-T

[187] O. Dechy-Cabaret, B. Martin-Vaca, and D. Bourissou, "Controlled ring-opening polymerization of lactide and glycolide," *Chemical Reviews*, vol. 104, no. 12, pp. 6147–6176, 2004. [Online]. Available: http://dx.doi.org/10.1021/cr040002s

[188] K. Masutani and Y. Kimura, *Chapter 1. PLA Synthesis. From the Monomer to the Polymer*, ser. Polymer Chemistry Series. Royal Society of Chemistry, 2014, pp. 1–36. [Online]. Available: http://dx.doi.org/10.1039/9781782624806-00001

[189] J. U. Izunobi and C. L. Higginbotham, "Polymer molecular weight analysis by ^{1}H NMR spectroscopy," *Journal of Chemical Education*, vol. 88, no. 8, pp. 1098–1104, 2011. [Online]. Available: http://dx.doi.org/10.1021/ed100461v

[190] R. Tomovska, A. Agirre, A. Veloso, and J. Leiza, *Characterization Techniques for Polymeric Materials*, ser. Reference Module in Chemistry, Molecular Sciences and Chemical Engineering. Elsevier, 2014, p. nil. [Online]. Available: http://dx.doi.org/10.1016/B978-0-12-409547-2.10910-2

[191] M. R. Kasaai, "Calculation of Mark-Houwink-Sakurada (MHS) equation viscometric constants for chitosan in any solvent-temperature system using experimental reported viscometric constants data," *Carbohydrate Polymers*, vol. 68, no. 3, pp. 477–488, 2007. [Online]. Available: http://dx.doi.org/10.1016/j.carbpol.2006.11.006

[192] P. T. Boeck, J. Tanaka, W. You, B. S. Sumerlin, and A. S. Veige, "Raft step-growth polymerization of bis-acrylamides and their facile degradation," *Polymer Chemistry*, vol. 14, no. 21, pp. 2592–2598, 2023. [Online]. Available: http://dx.doi.org/10.1039/D3PY00379E

[193] J. Oberlerchner, T. Rosenau, and A. Potthast, "Overview of methods for the direct molar mass determination of cellulose," *Molecules*, vol. 20, no. 6, pp. 10 313–10 341, 2015. [Online]. Available: http://dx.doi.org/10.3390/molecules200610313

[194] H. L. Wagner, "The Mark-Houwink-Sakurada Equation for the Viscosity of Atactic Polystyrene," *Journal of Physical and Chemical Reference Data*, vol. 14, no. 4, pp. 1101–1106, 1985. [Online]. Available: http://dx.doi.org/10.1063/1.555740

[195] N. Othman, A. Acosta-Ramírez, P. Mehrkhodavandi, J. R. Dorgan, and S. G. Hatzikiriakos, "Solution and melt viscoelastic properties of controlled microstructure poly(lactide)," *Journal of Rheology*, vol. 55, no. 5, pp. 987–1005, 2011. [Online]. Available: http://dx.doi.org/10.1122/1.3609853

[196] T. M. McGuire, A. Buchard, and C. Williams, "Chemical recycling of commercial poly(L-lactic acid) to L-lactide using a high-performance Sn(II)/alcohol catalyst system," *Journal of the American Chemical Society*, vol. 145, no. 36, pp. 19 840–19 848, 2023. [Online]. Available: http://dx.doi.org/10.1021/jacs.3c05863

[197] H. Tsuji, *Poly(lactic acid) - Hydrolytic Degradation*. New York City: Wiley, 2022.

[198] Z. He, L. Jiang, Y. Chuan, H. Li, and M. Yuan, "Ring-Opening Polymerization of l-Lactic Acid *O*-Carboxyanhydrides Initiated by Alkoxy Rare Earth Compounds,"

Molecules, vol. 18, no. 10, pp. 12 768–12 776, 2013. [Online]. Available: http://dx.doi.org/10.3390/molecules181012768

[199] P. Kenyon, M. Wörner, and S. Mecking, "Controlled polymerization in polar solvents to ultrahigh molecular weight polyethylene," *Journal of the American Chemical Society*, vol. 140, no. 21, pp. 6685–6689, 2018. [Online]. Available: http://dx.doi.org/10.1021/jacs.8b03223

[200] S. Farah, D. G. Anderson, and R. Langer, "Physical and mechanical properties of PLA, and their functions in widespread applications - A comprehensive review," *Advanced Drug Delivery Reviews*, vol. 107, no. nil, pp. 367–392, 2016. [Online]. Available: http://dx.doi.org/10.1016/J.ADDR.2016.06.012

[201] S. Metkar, V. Sathe, I. Rahman, B. Idage, and S. Idage, "Ring opening polymerization of lactide: Kinetics and modeling," *Chemical Engineering Communications*, vol. 206, no. 9, pp. 1159–1167, 2019. [Online]. Available: http://dx.doi.org/10.1080/00986445.2018.1550395

[202] R. Itzinger, C. Schwarzinger, and C. Paulik, "Investigation of the influence of impurities on the ring-opening polymerisation of L-Lactide from biogenous feedstock," *Journal of Polymer Research*, vol. 27, no. 12, p. 383, 2020. [Online]. Available: http://dx.doi.org/10.1007/s10965-020-02339-3

[203] N. J. Sherck, H. C. Kim, and Y.-Y. Won, "Elucidating a unified mechanistic scheme for the DBU-catalyzed ring-opening polymerization of lactide to poly(lactic acid)," *Macromolecules*, vol. 49, no. 13, pp. 4699–4713, 2016. [Online]. Available: http://dx.doi.org/10.1021/acs.macromol.6b00621

[204] L. Fang, R. Qi, L. Liu, G. Juan, and S. Huang, "Synthesis of poly(l-lactide) via solvothermal method," *International Journal of Polymer Science*, vol. 2009, no. nil, pp. 1–7, 2009. [Online]. Available: http://dx.doi.org/10.1155/2009/929732

[205] D. Obermayer, B. Gutmann, and C. O. Kappe, "Microwave chemistry in silicon carbide reaction vials: Separating thermal from nonthermal effects," *Angewandte Chemie International Edition*, vol. 48, no. 44, pp. 8321–8324, 2009. [Online]. Available: http://dx.doi.org/10.1002/anie.200904185

[206] A. Galia, O. Scialdone, T. Spanò, M. G. Valenti, B. Grignard, P. Lecomte, E. Monflier, S. Tilloy, and C. Rousseau, "Ring opening polymerization of e-caprolactone in the presence of wet β-cyclodextrin: Effect of the operative pressure and of water molecules

in the β-cyclodextrin cavity," *RSC Advances*, vol. 6, no. 93, pp. 90 290–90 299, 2016. [Online]. Available: http://dx.doi.org/10.1039/C6RA20211J

[207] J. K. Beasley, *Polymerization at High Pressure*, ser. Comprehensive Polymer Science and Supplements. Elsevier, 1989, pp. 273–282. [Online]. Available: http://dx.doi.org/10.1016/B978-0-08-096701-1.00083-5

[208] J. M. Pérez, C. Ruiz, and I. Fernández, "Synthesis of a biodegradable PLA: NMR signal deconvolution and end-group analysis," *Journal of Chemical Education*, vol. 99, no. 2, pp. 1000–1007, 2021. [Online]. Available: http://dx.doi.org/10.1021/acs.jchemed.1c00824

[209] R. Hador, M. Shuster, V. Venditto, and M. Kol, "Stereogradient Poly(Lactic Acid) from *meso*-Lactide/L-Lactide Mixtures," *Angewandte Chemie International Edition*, vol. 61, no. 40, p. nil, 2022. [Online]. Available: http://dx.doi.org/10.1002/anie.202207652

[210] M. A. Cuiffo, J. Snyder, A. M. Elliott, N. Romero, S. Kannan, and G. P. Halada, "Impact of the fused deposition (FDM) printing process on polylactic acid (PLA) chemistry and structure," *Applied Sciences*, vol. 7, no. 6, p. 579, 2017. [Online]. Available: http://dx.doi.org/10.3390/app7060579

[211] Y. Fan, H. Nishida, Y. Shirai, Y. Tokiwa, and T. Endo, "Thermal degradation behaviour of poly(lactic acid) stereocomplex," *Polymer Degradation and Stability*, vol. 86, no. 2, pp. 197–208, 2004. [Online]. Available: http://dx.doi.org/10.1016/j.polymdegradstab.2004.03.001

[212] F. Carrasco, O. S. Pérez, and M. Maspoch, "Kinetics of the thermal degradation of poly(lactic acid) and polyamide bioblends," *Polymers*, vol. 13, no. 22, p. 3996, 2021. [Online]. Available: http://dx.doi.org/10.3390/polym13223996

[213] C.-H. Chan, N. I. A. Manap, N. S. M. N. M. Din, A. S. A. Hazmi, K. W. Kow, and Y. K. Ho, "Strategy to scale up microwave synthesis with insight into the thermal and non-thermal effects from energy-based perspective," *Chemical Engineering and Processing - Process Intensification*, vol. 168, no. nil, p. 108594, 2021. [Online]. Available: http://dx.doi.org/10.1016/j.cep.2021.108594

[214] I. Polaert, M. Delmotte, N. Benamara, and L. Estel, "The effect of heat properties of metallic or dielectric containers on thermal yield and energy efficiency in microwave heating applications," *Chemical Engineering and Processing*

- *Process Intensification*, vol. 126, no. nil, pp. 1–7, 2018. [Online]. Available: http://dx.doi.org/10.1016/j.cep.2018.02.014

[215] M. Wehling, *Principles of Translational Science in Medicine*, ser. [From Bench to Bedside]. Elsevier, 2015. [Online]. Available: http://dx.doi.org/10.1016/C2013-0-15547-X

[216] N. Alasvand, A. M. Urbanska, M. Rahmati, M. Saeidifar, P. S. Gungor-Ozkerim, F. Sefat, J. Rajadas, and M. Mozafari, *Therapeutic Nanoparticles for Targeted Delivery of Anticancer Drugs*, ser. Multifunctional Systems for Combined Delivery, Biosensing and Diagnostics. Elsevier, 2017, pp. 245–259. [Online]. Available: http://dx.doi.org/10.1016/B978-0-323-52725-5.00013-7

[217] Y. K. Sung and S. W. Kim, "Recent advances in polymeric drug delivery systems," *Biomaterials Research*, vol. 24, no. 1, p. 12, 2020. [Online]. Available: http://dx.doi.org/10.1186/s40824-020-00190-7

[218] J.-M. Rabanel, J. Faivre, S. F. Tehrani, A. Lalloz, P. Hildgen, and X. Banquy, "Effect of the Polymer Architecture on the Structural and Biophysical Properties of PEG-PLA Nanoparticles," *ACS Applied Materials & Interfaces*, vol. 7, no. 19, pp. 10 374–10 385, 2015. [Online]. Available: http://dx.doi.org/10.1021/acsami.5b01423

[219] J. CHENG, B. TEPLY, I. SHERIFI, J. SUNG, G. LUTHER, F. GU, E. LEVYNIS-SENBAUM, A. RADOVICMORENO, R. LANGER, and O. FAROKHZAD, "Formulation of functionalized PLGA-PEG nanoparticles for in vivo targeted drug delivery," *Biomaterials*, vol. 28, no. 5, pp. 869–876, 2007. [Online]. Available: http://dx.doi.org/10.1016/j.biomaterials.2006.09.047

[220] S. Barua and S. Mitragotri, "Challenges associated with penetration of nanoparticles across cell and tissue barriers: a review of current status and future prospects," *Nano Today*, vol. 9, no. 2, pp. 223–243, 2014. [Online]. Available: http://dx.doi.org/10.1016/j.nantod.2014.04.008

[221] R. Singh and J. W. Lillard, "Nanoparticle-based targeted drug delivery," *Experimental and Molecular Pathology*, vol. 86, no. 3, pp. 215–223, 2009. [Online]. Available: http://dx.doi.org/10.1016/j.yexmp.2008.12.004

[222] X. Bai, Z. Smith, Y. Wang, S. Butterworth, and A. Tirella, "Sustained drug release from smart nanoparticles in cancer therapy: a comprehensive

review," *Micromachines*, vol. 13, no. 10, p. 1623, 2022. [Online]. Available: http://dx.doi.org/10.3390/mi13101623

[223] V. Weissig, T. Elbayoumi, B. Flühmann, and A. Barton, "The growing field of nanomedicine and its relevance to pharmacy curricula," *American Journal of Pharmaceutical Education*, vol. 85, no. 8, p. 8331, 2021. [Online]. Available: http://dx.doi.org/10.5688/ajpe8331

[224] I. J. Joye and D. J. McClements, "Production of nanoparticles by anti-solvent precipitation for use in food systems," *Trends in Food Science & Technology*, vol. 34, no. 2, pp. 109–123, 2013. [Online]. Available: http://dx.doi.org/10.1016/j.tifs.2013.10.002

[225] S. M. D'Addio and R. K. Prud'homme, "Controlling drug nanoparticle formation by rapid precipitation," *Advanced Drug Delivery Reviews*, vol. 63, no. 6, pp. 417–426, 2011. [Online]. Available: http://dx.doi.org/10.1016/j.addr.2011.04.005

[226] E. Lepeltier, C. Bourgaux, and P. Couvreur, "Nanoprecipitation and the "Ouzo effect": Application to drug delivery devices," *Advanced Drug Delivery Reviews*, vol. 71, no. nil, pp. 86–97, 2014. [Online]. Available: http://dx.doi.org/10.1016/j.addr.2013.12.009

[227] P. M. Valencia, O. C. Farokhzad, R. Karnik, and R. Langer, "Microfluidic technologies for accelerating the clinical translation of nanoparticles," *Nature Nanotechnology*, vol. 7, no. 10, pp. 623–629, 2012. [Online]. Available: http://dx.doi.org/10.1038/NNANO.2012.168

[228] M. Meeuwse, J. van der Schaaf, and J. C. Schouten, "Mass transfer in a rotor-stator spinning disk reactor with cofeeding of gas and liquid," *Industrial & Engineering Chemistry Research*, vol. 49, no. 4, pp. 1605–1610, 2009. [Online]. Available: http://dx.doi.org/10.1021/ie901301m

[229] M. Meeuwse, S. Lempers, J. van der Schaaf, and J. C. Schouten, "Liquid-solid mass transfer and reaction in a rotor-stator spinning disc reactor," *Industrial & Engineering Chemistry Research*, vol. 49, no. 21, pp. 10 751–10 757, 2010. [Online]. Available: http://dx.doi.org/10.1021/ie1003366

[230] M. M. de Beer, J. T. Keurentjes, J. C. Schouten, and J. van der Schaaf, "Intensification of convective heat transfer in a stator-rotor-stator spinning disc reactor," *AIChE Journal*, vol. 61, no. 7, pp. 2307–2318, 2015. [Online]. Available: http://dx.doi.org/10.1002/aic.14788

[231] M. M. de Beer, J. T. F. Keurentjes, J. C. Schouten, and J. van der Schaaf, "Forced convection boiling in a stator-rotor-stator spinning disc reactor," *AIChE Journal*, vol. 62, no. 10, pp. 3763–3773, 2016. [Online]. Available: http://dx.doi.org/10.1002/aic.15274

[232] A. N. M. Martínez, A. Chaudhuri, M. Besten, M. Assirelli, and J. van der Schaaf, "Micromixing efficiency in the presence of an inert gas in a rotor-stator spinning disk reactor," *Industrial & Engineering Chemistry Research*, vol. 60, no. 24, pp. 8677–8686, 2021. [Online]. Available: http://dx.doi.org/10.1021/acs.iecr.1c01238

[233] H. Toma and K. Nishino, "Convective mixing of miscible liquids in a rotor-stator spinning disk reactor," *Chemical Engineering Journal*, vol. 346, no. nil, pp. 329–339, 2018. [Online]. Available: http://dx.doi.org/10.1016/j.cej.2018.04.002

[234] M. Meeuwse, J. van der Schaaf, and J. C. Schouten, "Multistage rotor-stator spinning disc reactor," *AIChE Journal*, vol. 58, no. 1, pp. 247–255, 2011. [Online]. Available: http://dx.doi.org/10.1002/aic.12586

[235] A. Chaudhuri, S. D. A. Zondag, J. H. A. Schuurmans, J. van der Schaaf, and T. Noël, "Scale-up of a heterogeneous photocatalytic degradation using a photochemical rotor-stator spinning disk reactor," *Organic Process Research & Development*, vol. 26, no. 4, pp. 1279–1288, 2022. [Online]. Available: http://dx.doi.org/10.1021/acs.oprd.2c00012

[236] Y. Wang, J. Li, Y. Jin, M. Chen, and R. Ma, "Extraction of chromium (III) from aqueous waste solution in a novel rotor-stator spinning disc reactor," *Chemical Engineering and Processing - Process Intensification*, vol. 149, no. nil, p. 107834, 2020. [Online]. Available: http://dx.doi.org/10.1016/j.cep.2020.107834

[237] A. Chaudhuri, W. G. Backx, L. L. Moonen, C. W. Molenaar, W. Winkenweder, T. Ljungdahl, and J. van der Schaaf, "Kinetics and intensification of tertiary amine N-oxidation: Towards a solventless, continuous and sustainable process," *Chemical Engineering Journal*, vol. 416, no. nil, p. 128962, 2021. [Online]. Available: http://dx.doi.org/10.1016/j.cej.2021.128962

[238] P. Zhu, Y. Wang, J. Li, and Y. Jin, "Continuous production of high-capacity iron-based prussian blue sodium-ion cathode materials using a rotor-stator spinning disk reactor," *ACS Applied Energy Materials*, vol. 6, no. 11, pp. 6141–6150, 2023. [Online]. Available: http://dx.doi.org/10.1021/acsaem.3c00679

[239] M. Magosso, L. J. Hazen, M. van den Berg, and J. van der Schaaf, "Intensified sulfite reduction of alkyl hydroperoxides in a rotor-stator spinning-disc reactor," *Industrial & Engineering Chemistry Research*, vol. 60, no. 43, pp. 15 540–15 548, 2021. [Online]. Available: http://dx.doi.org/10.1021/acs.iecr.1c02626

[240] Y. Wang, X. Tao, J. Li, S. Zhang, Y. Jin, and M. Chen, "Esterification of free fatty acids in a rotor-stator spinning disc reactor," *Korean Journal of Chemical Engineering*, vol. 38, no. 8, pp. 1727–1732, 2021. [Online]. Available: http://dx.doi.org/10.1007/s11814-021-0815-3

[241] D. Liu, S. Cito, Y. Zhang, C. Wang, T. M. Sikanen, and H. A. Santos, "A versatile and robust microfluidic platform toward high throughput synthesis of homogeneous nanoparticles with tunable properties," *Advanced Materials*, vol. 27, no. 14, pp. 2298–2304, 2015. [Online]. Available: http://dx.doi.org/10.1002/adma.201405408

[242] P. M. Valencia, P. A. Basto, L. Zhang, M. Rhee, R. Langer, O. C. Farokhzad, and R. Karnik, "Single-step assembly of homogenous lipid-polymeric and lipid-quantum dot nanoparticles enabled by microfluidic rapid mixing," *ACS Nano*, vol. 4, no. 3, pp. 1671–1679, 2010. [Online]. Available: http://dx.doi.org/10.1021/nn901433u

[243] C. S. Funari, R. L. Carneiro, M. M. Khandagale, A. J. Cavalheiro, and E. F. Hilder, "Acetone as a greener alternative to acetonitrile in liquid chromatographic fingerprinting," *Journal of Separation Science*, vol. 38, no. 9, pp. 1458–1465, 2015. [Online]. Available: http://dx.doi.org/10.1002/jssc.201401324

[244] T. R. García, A. G. Ac, A. Lalloz, F.-X. Lacasse, P. Hildgen, J.-M. Rabanel, and X. Banquy, "Unified scaling of the structure and loading of nanoparticles formed by diffusion-limited coalescence," *Langmuir*, vol. 34, no. 20, pp. 5772–5780, 2018. [Online]. Available: http://dx.doi.org/10.1021/acs.langmuir.8b00652

[245] J. Baldyga and J. Bourne, "Simplification of micromixing calculations. I. Derivation and application of new model," *The Chemical Engineering Journal*, vol. 42, no. 2, pp. 83–92, 1989. [Online]. Available: http://dx.doi.org/10.1016/0300-9467(89)85002-6

[246] A. Kolmogorov, "The local structure of turbulence in incompressible viscous fluid for very large reynolds numbers," *Dokl. Akad. Nauk SSSR*, pp. 301–305, 1941.

[247] J. Baldyga and J. Bourne, *Turbulent Mixing and Chemical Reactions.* Wiley, 1999.

[248] M. de Beer, J. Keurentjes, J. Schouten, and J. van der Schaaf, "Bubble formation in co-fed gas-liquid flows in a rotor-stator spinning disc reactor," *International*

Journal of Multiphase Flow, vol. 83, no. nil, pp. 142–152, 2016. [Online]. Available: http://dx.doi.org/10.1016/j.ijmultiphaseflow.2016.03.013

[249] I. L. Blouza, C. Charcosset, S. Sfar, and H. Fessi, "Preparation and characterization of spironolactone-loaded nanocapsules for paediatric use," *International Journal of Pharmaceutics*, vol. 325, no. 1-2, pp. 124–131, 2006. [Online]. Available: http://dx.doi.org/10.1016/j.ijpharm.2006.06.022

[250] H.-C. Yang and M.-H. Hon, "The effect of the molecular weight of chitosan nanoparticles and its application on drug delivery," *Microchemical Journal*, vol. 92, no. 1, pp. 87–91, 2009. [Online]. Available: http://dx.doi.org/10.1016/j.microc.2009.02.001

[251] P. Legrand, S. Lesieur, A. Bochot, R. Gref, W. Raatjes, G. Barratt, and C. Vauthier, "Influence of polymer behaviour in organic solution on the production of polylactide nanoparticles by nanoprecipitation," *International Journal of Pharmaceutics*, vol. 344, no. 1-2, pp. 33–43, 2007. [Online]. Available: http://dx.doi.org/10.1016/j.ijpharm.2007.05.054

[252] M. Beck-Broichsitter, E. Rytting, T. Lebhardt, X. Wang, and T. Kissel, "Preparation of nanoparticles by solvent displacement for drug delivery: A shift in the "ouzo region" upon drug loading," *European Journal of Pharmaceutical Sciences*, vol. 41, no. 2, pp. 244–253, 2010. [Online]. Available: http://dx.doi.org/10.1016/j.ejps.2010.06.007

[253] R. Stepanyan, J. G. J. L. Lebouille, J. J. M. Slot, R. Tuinier, and M. A. C. Stuart, "Controlled nanoparticle formation by diffusion limited coalescence," *Physical Review Letters*, vol. 109, no. 13, p. 138301, 2012. [Online]. Available: http://dx.doi.org/10.1103/PhysRevLett.109.138301

[254] H. Lannibois, A. Hasmy, R. Botet, O. A. Chariol, and B. Cabane, "Surfactant limited aggregation of hydrophobic molecules in water," *Journal de Physique II*, vol. 7, no. 2, pp. 319–342, 1997. [Online]. Available: http://dx.doi.org/10.1051/jp2:1997128

[255] J. Lebouille, R. Stepanyan, J. Slot, M. C. Stuart, and R. Tuinier, "Nanoprecipitation of polymers in a bad solvent," *Colloids and Surfaces A: Physicochemical and Engineering Aspects*, vol. 460, no. nil, pp. 225–235, 2014. [Online]. Available: http://dx.doi.org/10.1016/j.colsurfa.2013.11.045

[256] S. Gimondi, H. Ferreira, R. L. Reis, and N. M. Neves, "Microfluidic devices: a tool for nanoparticle synthesis and performance evaluation," *ACS Nano*, vol. 17, no. 15, pp. 14 205–14 228, 2023. [Online]. Available: http://dx.doi.org/10.1021/acsnano.3c01117

[257] C. C. Bannan, G. Calabró, D. Y. Kyu, and D. L. Mobley, "Calculating partition coefficients of small molecules in octanol/water and cyclohexane/water," *Journal of Chemical Theory and Computation*, vol. 12, no. 8, pp. 4015–4024, 2016. [Online]. Available: http://dx.doi.org/10.1021/acs.jctc.6b00449

[258] T. Scheytt, P. Mersmann, R. Lindstädt, and T. Heberer, "1-octanol/water partition coefficients of 5 pharmaceuticals from human medical care: Carbamazepine, clofibric acid, diclofenac, ibuprofen, and propyphenazone," *Water, Air, and Soil Pollution*, vol. 165, no. 1-4, pp. 3–11, 2005. [Online]. Available: http://dx.doi.org/10.1007/s11270-005-3539-9

[259] T. Yano, A. Nakagawa, M. Tsuji, and K. Noda, "Skin permeability of various non-steroidal anti-inflammatory drugs in man," *Life Sciences*, vol. 39, no. 12, pp. 1043–1050, 1986. [Online]. Available: http://dx.doi.org/10.1016/0024-3205(86)90195-5

[260] H.-Y. Wang, C. Li, N. Wang, K. Li, X.-W. Feng, T. He, and X.-Q. Yu, "Two-step enzymatic selective synthesis of water-soluble ketoprofen-saccharide conjugates in organic media," *Bioorganic & Medicinal Chemistry*, vol. 17, no. 5, pp. 1905–1910, 2009. [Online]. Available: http://dx.doi.org/10.1016/j.bmc.2009.01.040

[261] S. Essa, J. M. Rabanel, and P. Hildgen, "Effect of polyethylene glycol (PEG) chain organization on the physicochemical properties of poly(D,L-Lactide) (PLA) based nanoparticles," *European Journal of Pharmaceutics and Biopharmaceutics*, vol. 75, no. 2, pp. 96–106, 2010. [Online]. Available: http://dx.doi.org/10.1016/j.ejpb.2010.03.002

[262] J. Xing, D. Zhang, and T. Tan, "Studies on the oridonin-loaded poly(D,L-lactic acid) nanoparticles *in vitro* and *in vivo*," *International Journal of Biological Macromolecules*, vol. 40, no. 2, pp. 153–158, 2007. [Online]. Available: http://dx.doi.org/10.1016/j.ijbiomac.2006.07.001

[263] Z. Song, R. Feng, M. Sun, C. Guo, Y. Gao, L. Li, and G. Zhai, "Curcumin-loaded PLGA-PEG-PLGA triblock copolymeric micelles: Preparation, pharmacokinetics and distribution in vivo," *Journal of Colloid and Interface Science*, vol. 354, no. 1, pp. 116–123, 2011. [Online]. Available: http://dx.doi.org/10.1016/j.jcis.2010.10.024

[264] L. Milane, Z. Duan, and M. Amiji, "Development of EGFR-Targeted Polymer Blend Nanocarriers for Combination Paclitaxel/Lonidamine Delivery To Treat Multi-Drug Resistance in Human Breast and Ovarian Tumor Cells," *Molecular*

Pharmaceutics, vol. 8, no. 1, pp. 185–203, 2010. [Online]. Available: http://dx.doi.org/10.1021/mp1002653

[265] L. Lai and H. Guo, "Preparation of new 5-fluorouracil-loaded zein nanoparticles for liver targeting," *International Journal of Pharmaceutics*, vol. 404, no. 1-2, pp. 317–323, 2011. [Online]. Available: http://dx.doi.org/10.1016/j.ijpharm.2010.11.025

[266] A. K. Jain, N. K. Swarnakar, C. Godugu, R. P. Singh, and S. Jain, "The effect of the oral administration of polymeric nanoparticles on the efficacy and toxicity of tamoxifen," *Biomaterials*, vol. 32, no. 2, pp. 503–515, 2011. [Online]. Available: http://dx.doi.org/10.1016/j.biomaterials.2010.09.037

[267] M. Holgado, J. Arias, M. Cózar, J. Alvarez-Fuentes, A. Gañán-Calvo, and M. Fernández-Arévalo, "Synthesis of lidocaine-loaded PLGA microparticles by flow focusing," *International Journal of Pharmaceutics*, vol. 358, no. 1-2, pp. 27–35, 2008. [Online]. Available: http://dx.doi.org/10.1016/j.ijpharm.2008.02.012

[268] S. Mitic and S. de Vries, *1.22 Rapid Mixing Techniques for the Study of Enzyme Catalysis*, ser. Comprehensive Biophysics. Elsevier, 2012, pp. 514–532. [Online]. Available: http://dx.doi.org/10.1016/B978-0-12-374920-8.00127-2

[269] J. Brody, P. Yager, R. Goldstein, and R. Austin, "Biotechnology at low reynolds numbers," *Biophysical Journal*, vol. 71, no. 6, pp. 3430–3441, 1996. [Online]. Available: http://dx.doi.org/10.1016/S0006-3495(96)79538-3

[270] D. Sobek, "Microfabricated fused silica flow chambers for flow cytometry," 1997, available at http://dspace.mit.edu/handle/1721.1/10262.

[271] X. Yuan, A. Glidle, H. Furusho, and H. Yin, "A 3D hydrodynamic flow-focusing device for cell sorting," *Microfluidics and Nanofluidics*, vol. 25, no. 3, p. 23, 2021. [Online]. Available: http://dx.doi.org/10.1007/s10404-021-02425-y

[272] W. Wu, P. Rezai, H. Hsu, and P. Selvaganapathy, *Materials and methods for the microfabrication of microfluidic biomedical devices*, ser. Microfluidic Devices for Biomedical Applications. Elsevier, 2013, pp. 3–62. [Online]. Available: http://dx.doi.org/10.1533/9780857097040.1.3

[273] B. K. Johnson and R. K. Prud'homme, "Chemical processing and micromixing in confined impinging jets," *AIChE Journal*, vol. 49, no. 9, pp. 2264–2282, 2003. [Online]. Available: http://dx.doi.org/10.1002/aic.690490905

[274] W. S. Saad and R. K. Prud'homme, "Principles of nanoparticle formation by flash nanoprecipitation," *Nano Today*, vol. 11, no. 2, pp. 212–227, 2016. [Online]. Available: http://dx.doi.org/10.1016/j.nantod.2016.04.006

[275] L.-H. Hung, S.-Y. Teh, J. Jester, and A. P. Lee, "PLGA micro/nanosphere synthesis by droplet microfluidic solvent evaporation and extraction approaches," *Lab on a Chip*, vol. 10, no. 14, p. 1820, 2010. [Online]. Available: http://dx.doi.org/10.1039/C002866E

[276] T. V. Kármán, "Über laminare und turbulente reibung," *ZAMM - Journal of Applied Mathematics and Mechanics / Zeitschrift für Angewandte Mathematik und Mechanik*, vol. 1, no. 4, pp. 233–252, 1921. [Online]. Available: http://dx.doi.org/10.1002/zamm.19210010401

[277] U. T. Bödewadt, "Die drehströmung über festem grunde," *ZAMM - Journal of Applied Mathematics and Mechanics / Zeitschrift für Angewandte Mathematik und Mechanik*, vol. 20, no. 5, pp. 241–253, 1940. [Online]. Available: http://dx.doi.org/10.1002/zamm.19400200502

[278] S. PONCET, M. P. CHAUVE, and P. L. GAL, "Turbulent rotating disk flow with inward throughflow," *Journal of Fluid Mechanics*, vol. 522, no. nil, pp. 253–262, 2005. [Online]. Available: http://dx.doi.org/10.1017/S0022112004002046

[279] D. Cun, C. Foged, M. Yang, S. Frøkjær, and H. M. Nielsen, "Preparation and characterization of poly(DL-Lactide-Co-Glycolide) nanoparticles for siRNA delivery," *International Journal of Pharmaceutics*, vol. 390, no. 1, pp. 70–75, 2010. [Online]. Available: http://dx.doi.org/10.1016/j.ijpharm.2009.10.023

[280] L. M. Cafiero, G. Baffi, A. Chianese, and R. J. J. Jachuck, "Process intensification: Precipitation of barium sulfate using a spinning disk reactor," *Industrial & Engineering Chemistry Research*, vol. 41, no. 21, pp. 5240–5246, 2002. [Online]. Available: http://dx.doi.org/10.1021/ie010654w

[281] R. Donno, A. Gennari, E. Lallana, J. M. R. D. L. Rosa, R. d'Arcy, K. Treacher, K. Hill, M. Ashford, and N. Tirelli, "Nanomanufacturing through microfluidic-assisted nanoprecipitation: Advanced analytics and structure-activity relationships," *International Journal of Pharmaceutics*, vol. 534, no. 1-2, pp. 97–107, 2017. [Online]. Available: http://dx.doi.org/10.1016/j.ijpharm.2017.10.006

[282] U. Phadke and J. Owen, "Aerodynamic aspects of the sealing of gas-turbine rotor-stator systems," *International Journal of Heat and Fluid Flow*, vol. 9, no. 2, pp. 98–105, 1988. [Online]. Available: http://dx.doi.org/10.1016/0142-727X(88)90060-4

[283] M. Schrimpf, J. Esteban, H. Warmeling, T. Färber, A. Behr, and A. J. Vorholt, "Taylor-couette reactor: Principles, design, and applications," *AIChE Journal*, vol. 67, no. 5, p. nil, 2021. [Online]. Available: http://dx.doi.org/10.1002/aic.17228

[284] T. Tezduyar, *Stabilized Finite Element Formulations for Incompressible Flow Computations*, ser. Advances in Applied Mechanics. Elsevier, 1991, pp. 1–44. [Online]. Available: http://dx.doi.org/10.1016/S0065-2156(08)70153-4

[285] T. Tezduyar and S. Sathe, "Stabilization parameters in SUPG and PSPG formulations," *Journal of Computational and Applied Mechanics*, vol. 4, no. 1, pp. 71–88, 2003. [Online]. Available: https://www.researchgate.net/publication/265330934_Stabilization_parameters_in_SUPG_and_PSPG_formulations

[286] L. P. Saavedra, C. E. N. Radburn, A. Collard-Daigneault, and B. Blais, "An implicit large-eddy simulation perspective on the flow over periodic hills," *Computers &; Fluids*, vol. 283, no. nil, p. 106390, 2024. [Online]. Available: http://dx.doi.org/10.1016/j.compfluid.2024.106390

[287] M. Grigoriev, T. Carrigan, D. Garlisch, and J. Hitt, "Higher order finite element meshes for centrifugal impeller blade analyses using pointwise," in *Volume 7A: Structures and Dynamics*, 2014, p. nil. [Online]. Available: http://dx.doi.org/10.1115/GT2014-25734

[288] B. Launder, S. Poncet, and E. Serre, "Laminar, transitional, and turbulent flows in rotor-stator cavities," *Annual Review of Fluid Mechanics*, vol. 42, no. 1, pp. 229–248, 2010. [Online]. Available: http://dx.doi.org/10.1146/annurev-fluid-121108-145514

[289] S. L. Soo, "Laminar flow over an enclosed rotating disk," *Journal of Fluids Engineering*, vol. 80, no. 2, pp. 287–294, 1958. [Online]. Available: http://dx.doi.org/10.1115/1.4012346

[290] F. Cabaret, S. Bonnot, L. Fradette, and P. A. Tanguy, "Mixing time analysis using colorimetric methods and image processing," *Industrial & Engineering Chemistry Research*, vol. 46, no. 14, pp. 5032–5042, 2007. [Online]. Available: http://dx.doi.org/10.1021/ie0613265